REPORT DOCUMENTATION PAGE

AFRL-SR-AR-TR-04-

0168

Public reporting burden for this collection of information is estimated to average 1 hour per response, including the time for reviewing ins data needed, and completing and reviewing this collection of information. Send comments regarding this burden estimate or any other a this burden to Department of Defense, Washington Headquarters Services, Directorate for Information Operations and Reports 0704-0 4302. Respondents should be aware that notwithstanding any other provision of law, no person shall be subject to any penalty for failing valid OMB control number. **PLEASE DO NOT RETURN YOUR FORM TO THE ABOVE ADDRESS.**

1. REPORT DATE (DD-MM-YYYY) 01/03/04	2. REPORT TYPE Final Technical Report	3. DATES COVERED (From - To) November 1999-November 2001

4. TITLE AND SUBTITLE	
Pulsed-Sound Measurements of the Influence of High-Amplitude Noise on Boundary-Layer Transition to Turbulence	5a. CONTRACT NUMBER
	5b. GRANT NUMBER F49620-00-1-0075
	5c. PROGRAM ELEMENT NUMBER

6. AUTHOR(S)	
William S. Saric	5d. PROJECT NUMBER
	5e. TASK NUMBER
	5f. WORK UNIT NUMBER

7. PERFORMING ORGANIZATION NAME(S) AND ADDRESS(ES)	8. PERFORMING ORGANIZATION REPORT NUMBER
Mechanical and Aerospace Engineering Department, Arizona State University, Tempe, AZ 85287-6106	XAA 0089/TE

9. SPONSORING / MONITORING AGENCY NAME(S) AND ADDRESS(ES)	10. SPONSOR/MONITOR'S ACRONYM(S)
Air Force Office of Scientific Research / NA ATTN: Dr. Thomas J. Beutner Program Officer / NA 4015 Wilson Blvd, Room 713 Arlington VA 22203-1954	AFOSR
	11. SPONSOR/MONITOR'S REPORT NUMBER(S)

12. DISTRIBUTION / AVAILABILITY STATEMENT

APPROVED FOR PUBLIC RELEASE.

20040319 113

13. SUPPLEMENTARY NOTES

14. ABSTRACT
An experimental study of leading-edge receptivity to high-amplitude acoustic forcing was conducted in the low-turbulence Arizona State University Unsteady Wind Tunnel. The experiment examined unstable wave evolution in a Blasius boundary layer produced on a flat plate. A pulsed-sound technique was employed to generate measurements of receptivity coefficients for a 20:1 modified-super-ellipse leading edge. The leading-edge profile ensures that there is no curvature discontinuity at the flat-plate juncture, therefore limiting the receptivity sources. The goal of the pulsed-sound method was to prevent the superposition of the Stokes and Tollmien-Schlichting (T-S) waves that were prevalent in previous experiments. Separation was achieved via a short acoustic pulse, followed by the conditional sampling of the boundary layer. The resulting signal yielded a pure T-S wave. The signals were examined in the frequency domain, where the magnitudes of the ensemble-averaged Fourier coefficients were used to calculate the receptivity coefficients. These experiments resolved the erroneous narrow pass-band response of all other experiments, extended the measurement range of previous experiments, and provided very good validation of analytical and numerical models. Results revealed good agreement with linear stability theory. Receptivity coefficients are presented and the first step to a transition prediction scheme has been completed.

15. SUBJECT TERMS
Receptivity, sound interaction, initial conditions

16. SECURITY CLASSIFICATION OF:			17. LIMITATION OF ABSTRACT	18. NUMBER OF PAGES	19a. NAME OF RESPONSIBLE PERSON William S. Saric
Report Unclassified	b. ABSTRACT Unclassified	c. THIS PAGE Unclassified	100-200 words	including this page 118	19b. TELEPHONE NUMBER (include area code) (480) 965-2822

Standard Form 298 (Rev. 8-98)
Prescribed by ANSI Std. Z39.18

PULSED-SOUND MEASUREMENTS OF INFLUENCE OF HIGH-AMPLITUDE

NOISE ON BOUNDARY-LAYER TRANSITION TO TURBULENCE

AFOSR GRANT F49620-00-0075

EXECUTIVE SUMMARY

and

FINAL TECHNICAL REPORT

William S. Saric
Mechanical and Aerospace Engineering
Arizona State University, Tempe, AZ 85287-6106
saric@asu.edu
http://frc.asu.edu

Executive Summary

Summary

Although there has been significant experimental progress in understanding the transition process, researchers are still unable to predict transition. Arguably the most important yet least understood phase of transition is the process by which freestream disturbances are introduced into the boundary layer (i.e. receptivity). Understanding of receptivity provides the essential initial amplitudes and other characteristics of the resulting instabilities, which can be used to validate both theoretical and numerical models.

The annual review paper by Saric et al (2002) is a thorough summary of the experimental and computational accomplishments of this and other programs. It represents the culmination of the present work done under AFOSR sponsorship. The remainder of the executive summary gives an example of a successful comparison between computations and experiment as well as the principal conclusions. The following final report gives many of the experimental details and figures.

Project Goals

Determine leading-edge receptivity coefficients using pulsed acoustic forcing. Use these results to resolve the present conflict that exists between numerical models and experimental results obtained using constant acoustic forcing. Provide a data base of receptivity coefficients for freestream sound.

Approach

A pulsed-sound technique was employed to generate measurements of receptivity coefficients for a 20:1 modified-super-ellipse leading edge. The leading-edge profile ensures that there is no curvature discontinuity at the flat-plate juncture, therefore limiting the receptivity sources. The goal of the pulsed-sound method was to prevent the superposition of the Stokes and Tollmien-Schlichting (T-S) waves that were prevalent in previous experiments. Separation was achieved via a short acoustic pulse, followed by the conditional sampling of the boundary layer. The resulting signal yielded a pure T-S wave. The signals were examined in the frequency domain, where the magnitudes of the ensemble-averaged Fourier coefficients were used to calculate the receptivity coefficients.

Leading-Edge Receptivity to Freestream Sound

We conducted a series of leading-edge receptivity experiments on a 20:1 modified super ellipse given in Saric et al (1999). The leading edge is machined directly on a 4000 mm (chord) x 1370 mm (span) x 9.53 mm (thickness) flat-plate. This design moves the pressure minimum toward the leading edge, eliminates the curvature discontinuity at the juncture, and eliminates any discontinuities associated with the ellipse/flat-plate juncture which could serve as a receptivity mechanism. Simultaneous static pressure

measurements on each side of the leading edge are used to adjust the flap for symmetric flow. For the experiments, the sound pressure level in the test section is varied from 90 dB to 125 dB ($p' = \rho c_a u'_{rms}$; 20-μPa reference). This gives a $|u'_{ac}|_{fs} = O(10^{-4} - 10^{-2} U_\infty)$.

The pulsed-sound technique has been used to measure T-S mode shapes. The observed mode shapes match linear theory predictions and demonstrate convincingly that the pulsed-sound/Fourier technique of White et al (2000) is a valid means of measuring relative disturbance amplitude. The results are compared with DNS in Table 1.

TABLE 1: Branch I receptivity coefficients for multiple frequencies as predicted by DNS and compared with the experiments.

Case	Wanderley & Corke (2001) DNS	Fuciarelli et al (2000) DNS	Saric et al (1999) Experiment
F	90	82—86	88—92
K_s	0.046	0.048	0.045 ± 0.005

Here we use

$$F = 2\pi f \nu / U_\infty^2 \times 10^6 \quad \text{and} \qquad K_s = |u'_{TS}|_I / |u'_{ac}|_{LE}$$

The agreement between DNS and experiment is rather remarkable. In this case the nominal freestream speed was 8 m/s which was the upper limit on Reynolds number for the DNS and the lower limit of the experiments.

Figure 1 shows that the receptivity process is linear over several orders of magnitude of forcing amplitude. This is true of all of the other cases conducted.
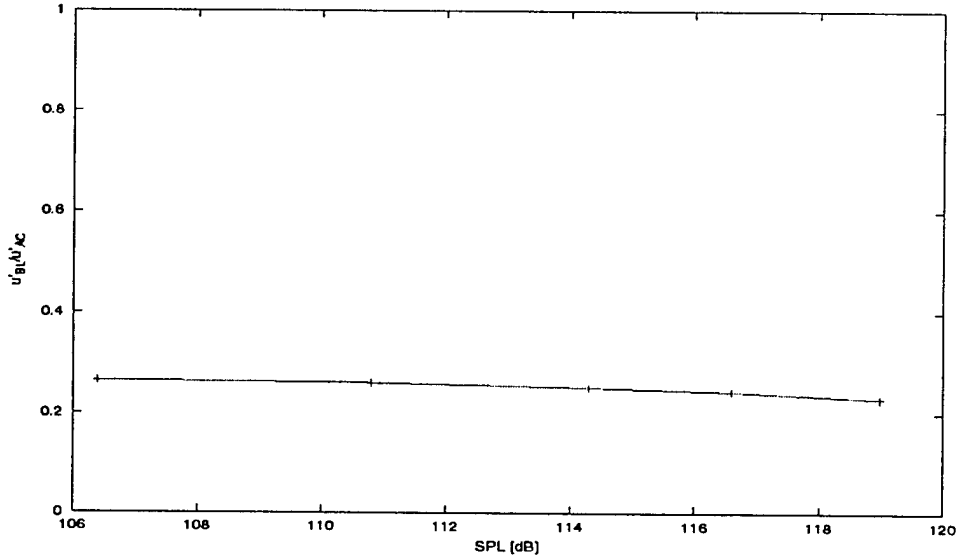

Figure 1. Disturbance amplitude versus freestream sound pressure level for 8m/s.

Principal Results

The remarkable agreement between computations and experiments validates the codes at low Reynolds numbers.

A higher Reynolds number data base for computations is provided from the experiments.

The role of random (broad band) noise is minimized since transition to turbulence is still triggered by the frequency of the most unstable mode – even in the range of 120-130 dB where nonlinear interactions are thought to be important.

Three-dimensional disturbances are still needed to trigger transition. Thus some combination of sound and turbulence are the real causes of transition.

The most effective study to determine the initial conditions for transition will be a combination of freestream turbulence and sound. That is to say, some combination of the turbulence work done at JPL and the acoustic work done at ASU.

Personnel Supported

William Saric	Professor, Arizona State University (ASU)
Pierre Gabet	Graduate Student, ASU
Robert Gladden	Graduate Student, ASU
Danny C. Clevenger	Wind Tunnel Technician, ASU

M.S. Students Graduated

P. Gabet, 2001. "Pulsed sound techniques for leading edge receptivity." Dec 2001.

R. Gladden, 2001. "Role of random distributed roughness on boundary layer transition." Dec 2001

References

Fuciarelli DA, Reed HL, Lyttle I. 2000. Direct numerical simulation of leading-edge receptivity to sound. *AIAA J.* 38(7):1159-65

Wanderly JBV, Corke TC. 2001 Boundary layer receptivity to free-steam sound on elliptic leading edges of flat plates. *J. Fluid Mech.* 429:1-29

Publications

Fasel HF, Saric WS. eds. 2000. *Laminar-Turbulent Transition V.* Springer. 686 pp.

Saric WS, White EB. 1998. Influence of high-amplitude noise on boundary-layer transition to turbulence. *AIAA Pap. No. 98-2645*

Saric WS, Reed HL, White EB. 1999. Boundary-layer receptivity to freestream disturbances and its role in transition. *AIAA Pap. No. 99-3788*

Saric WS, Reed HL, Kerschen EJ. 2002. Boundary-layer receptivity to freestream disturbances. *Ann. Rev. Fluid Mech. Vol. 34*, to appear.

White, E.B., Saric, W.S., Radeztsky, R.H. Jr. 2000 Leading-Edge Acoustic Receptivity Measurements Using a Pulsed-Sound Technique. *Laminar-Turbulent Transition, Vol. V.* Eds. W. Saric, H. Fasel, Springer-Verlag. . pp. 103-08. ISBN 3-540-679472.2

Reed, H., Saric, W.S. 2002 CFD Validation Issues for Stability and Transition. (*invited*) *ASME FED-SM2002-31366*.

Saric, W.S., Reed, H.L., Kerschen, E.J. 2002 Boundary-Layer Receptivity to Freestream Disturbances. *Ann. Rev. Fluid Mech. Vol. 34*, pp. 291-319.

Talks and Lectures

"Boundary Layer Receptivity to Freestream Disturbances and its role in Transition" (invited) E.B. White, 30th AIAA Fluid Dynamics Conference, Norfolk, VA. *AIAA Paper No. 99-3788,* June 28 – July 1, 1999.

"Validation of an Acoustic-Receptivity Experiment Using a PSV" E. White. Vibra*Scan* Annual Scanning Laser Vibrometer Users Meeting, San Jose, CA. June 8, 1999.

"Leading-Edge Acoustic Receptivity Measurements Using a Pulsed-Sound Technique" E.B. White, IUTAM Symposium on Laminar-Turbulent Transition, Sedona, AZ. September 13-17, 1999.

"Measurement of Laminar-Turbulent Transition Behavior" W.S. Saric, Workshop on Prediction of Laminar-turbulent Transition in Boundary Layers, Tokyo, Japan, September 27-29, 2000.

"Receptivity Effects in Transition Control" W.S. Saric, APS/DFD 53 Ann. Mtg. 19-21 Nov. 2000, *Bull. Am. Phys. Soc. Vol. 45, No. 11*.

"Boundary-Layer Receptivity to Freestream Sound" W.S. Saric, EuroMech Colloquim 423, 2-4 April 2001, Stuttgart, Germany.

TABLE OF CONTENTS

CHAPTER 1

INTRODUCTION

1.1. Background and motivation

Although there has been significant experimental progress in understanding the transition process from laminar to turbulent flow, researchers are still unable to predict the transition Reynolds number on a flat plate (Saric 1994). Transition plays an important role since it ultimately affects essential quantities such as skin friction and heat transfer. Laminar flow is generally a desired flow condition since a laminar boundary layer causes less drag than a turbulent boundary layer. For example, it has been assessed that if laminar flow could be maintained over the wings of a modern jetliner, an estimated 25% reduction in fuel consumption would be attained (Pfenninger 1977, Thomas 1985, Saric 1994). Understanding and predicting transition from laminar flow to turbulent flow can lead to many other practical applications. For instance, a reliable transition model is essential to the prediction of heat transfer in high-speed aircrafts and reentry vehicles. Other considerable efforts are directed towards technologies like Laminar Flow Control (LFC) or Natural Laminar Flow (NLF) in an attempt to delay or prevent transition.

However, to successfully develop and apply these technologies, the intricacies of the transition process must be understood. In particular, research must determine how factors such as freestream turbulence or acoustic disturbances provide the initial conditions for the growing instabilities.

With the development of low turbulence wind tunnels, the existence of viscous instability waves within a laminar boundary layer was experimentally validated by Schubauer and Skramstad in 1943. Since then, a multitude of experimental research has been conducted to examine boundary-layer transition. This experiment will examine receptivity to acoustic forcing using a new frequency-domain pulsed-sound technique that prevents the detrimental effects from reflected waves that were pervasive in earlier experiments

1.2. Boundary-layer transition

In general the transition process involves three distinct stages: receptivity, or the entrainment of freestream disturbances into the boundary layer, linear growth of the disturbances and non-linear interactions and breakdown to turbulence (Saric 1994).

Receptivity, a concept first introduced by Morkovin (1969), describes how freestream disturbances such as sound or vorticity interact with leading-edge curvature, or roughness, and enter the boundary layer as small fluctuations of the basic state. Arguably, receptivity is the most important phase of transition because it creates the initial amplitude of the instability mode, yet it remains the least understood.

The second stage is well described by linear stability theory. The unsteady, linearized Navier-Stokes equations can be solved to model the growth of the entrained disturbances. Linear stability theory has been developing since the 1920s when Prandtl first developed the fundamental ideas of a viscous instability mechanism and Tollmien and Schlichting examined the solutions to the Orr-Sommerfeld equation for incompressible, two-dimensional flows with zero pressure gradient (Blasius flow). For a Blasius boundary layer, the instability wave is of the Tollmien-Schlichting (T-S) type (Mack 1984).

The last stage of boundary layer transition occurs as the amplitude of the instability waves grows, causing nonlinear and three-dimensional interactions and allowing the growth of secondary instabilities leading to the rapid breakdown into turbulence. The three-dimensional modes for T-S waves are characterized by peak-valley splitting into K-type (Klebanoff et al. 1962), C-type (Craik 1971), and H-type breakdown (Herbert 1983).

The three stages described above are not the only path to turbulence. If the initial disturbances are large enough the linear growth stage can be bypassed and the flow becomes turbulent immediately (Morkovin 1969). This occurs when the flow is "tripped" by the introduction of large roughness elements, or high amplitude freestream turbulence or sound. A review of the bypass mechanism for high freestream turbulence is given by Reshotko (1994).

1.3. Transition prediction

Although the transition process is not well understood, transition-prediction models are commonly used in industry. The conventional transition prediction tool is the e^N method of Smith & Gamberoni (1956) and van Ingen (1956). This model only accounts for the linear amplification phase of the transition process and does not include any receptivity effects. The e^N method postulates that there is a critical N-factor, defined in equation (1.1) where transition will occur.

$$N = \ln(A/A_0) = \int_{x_0}^{x} -\alpha_i dx \qquad (1.1)$$

Here A_o is the amplitude of the disturbance at Branch I of the neutral stability curve, A is the amplitude at some location downstream of the first neutral-stability point, and $-\alpha_i$ is the spatial growth rate.

The e^N method is widely used and is applied at all speeds (Bushnell et al., 1989), and for systems with similar geometries and disturbance environments it predicts transition with significant success for streamwise disturbances. However, this technique relies on empirical observations and cannot be used successfully to correlate data for cases where experimental data is not available, since the method ignores the different initial conditions for the boundary-layer instability development. Given that the receptivity stage is not accounted for, the method is susceptible to large error and should be used with caution.

1.4. Theory

1.4.1. *The basic state*

The simplest boundary layer forms on a flat plate under a zero pressure gradient. Such a flow is called Blasius flow and is used as the basic state for this experiment, mostly for simplicity as well as for the vast amount of stability information available. In addition, using this basic state allows for comparison to theoretical models.

The governing equation for a 2-D boundary layer is given by the Falkner-Skan equation for similar flows, shown in equation (1.2)

$$f''' + \frac{1}{2} ff'' + \frac{1}{2} \beta(1 - f'^2) = 0 \qquad (1.2)$$

with boundary conditions:

$$f(0) = f'(0) = 0, f'(\infty) = 1 \qquad (1.3)$$

where $f=f(\eta)$, $f'(\eta)=U(y)/u$ and $\eta=y/(vx/u)^{1/2}$. The parameter β is a measure of the pressure gradient, and it is equal to zero for a Blasius flow.

For a one-dimensional boundary layer the basic state is described by equations (1.4)-(1.6)

$$U = U(y) \quad ; \quad V = 0 \quad ; \quad W = W(y) \qquad (1.4)$$

$$\frac{1}{R} \frac{d^2 U}{dy^2} = \frac{dP}{dx} \qquad (1.5)$$

$$\frac{1}{R}\frac{d^2W}{dy^2} = \frac{dP}{dz} \tag{1.6}$$

where (U,V,W) are the chordwise, normal and spanwise velocity components. The flow is assumed incompressible and parallel.

1.4.2. *Linear stability analysis*

Turbulence occurs as a result of large-amplitude velocity fluctuations in the boundary layer. These fluctuations of particular frequencies grow exponentially from very small amplitudes to trigger the transition process. The initial growth of disturbances in a Blasius flow can be correctly described by linear stability theory. The basic idea of linear theory is to superpose small disturbances onto the basic state and determine whether these disturbances grow or decay. The following discussion provides an overview of linear stability theory applied to a Blasius boundary layer. For a comprehensive discussion of linear stability theory the reader is referred to Saric et al. (1996).

The stability equations are obtained by superposition of small disturbances given in equations (1.7)-(1.10)

$$\frac{\hat{u}}{U_\infty} = U(y) + u'(x, y, z, t) \tag{1.7}$$

$$\frac{\hat{v}}{U_\infty} = v'(x, y, z, t) \tag{1.8}$$

$$\frac{\hat{w}}{U_\infty} = W(y) + w'(x, y, z, t) \tag{1.9}$$

$$\frac{\hat{p}}{\rho U_\infty^2} = P(x, z) + p'(x, y, z, t) \tag{1.10}$$

where the prime quantities, representing the perturbations, must be functions of *x, y, z,* and *t*. The resulting system, equations (1.11) through (1.14), is obtained by substitution and linearization (i.e., neglecting products of disturbance quantities) of equations (1.7)-(1.10) into the unsteady Navier-Stokes equations.

$$\frac{\partial u'}{\partial x} + \frac{\partial v'}{\partial y} + \frac{\partial w'}{\partial z} = 0 \tag{1.11}$$

$$\frac{\partial u'}{\partial t} + U\frac{\partial u'}{\partial x} + W\frac{\partial u'}{\partial z} + \frac{\partial U}{\partial y}v' + \frac{\partial p'}{\partial x} - \frac{1}{R}\nabla^2 u' = 0 \tag{1.12}$$

$$\frac{\partial v'}{\partial t} + U\frac{\partial v'}{\partial x} + W\frac{\partial v'}{\partial z} + \frac{\partial p'}{\partial y} - \frac{1}{R}\nabla^2 v' = 0 \tag{1.13}$$

$$\frac{\partial w'}{\partial t} + U\frac{\partial w'}{\partial x} + W\frac{\partial w'}{\partial z} + \frac{\partial W}{\partial y}v' + \frac{\partial p'}{\partial z} - \frac{1}{R}\nabla^2 w' = 0 \tag{1.14}$$

These disturbance equations are linear, and the coefficients are in terms of y only. Therefore we can expect a solution by means of separation of variables using normal modes. One accepted normal mode for bounded shear flows is shown in equation (1.15)

$$q'(x, y, z, t) = q(y)\exp[i(\alpha x + \beta z - \omega t)] + C.C. \qquad (1.15)$$

where the chordwise and spanwise wavenumbers, α and β respectively, are complex quantities and the frequency ω is real. This spatial normal mode is only valid for parallel flow. For this reason, in a real boundary layer flow, where the parallel assumption holds only for small chordwise displacements, the stability characteristics must be re-evaluated at each chord location. In view of this, the normal mode is generalized with the introduction of the phase function Θ as shown in equations (1.16)-(1.19)

$$q'(x, y, z, t) = q(y)\exp(i\Theta) + C.C. \qquad (1.16)$$

where $\Theta = \Theta(x, z, t)$ and

$$\frac{\partial \Theta}{\partial x} = \alpha \qquad (1.17)$$

$$\frac{\partial \Theta}{\partial z} = \beta \qquad (1.18)$$

$$\frac{\partial \Theta}{\partial t} = -\omega \qquad (1.19)$$

This approach produces a zero-order (quasi-parallel) approximation that can be rigorously justified using a non-parallel analysis (Gaster 1974, Saric & Nayfeh 1977).

Substitution of equation (1.16) into equations (1.11)-(1.14) gives

$$i\alpha u + i\beta w + Dv = 0 \tag{1.20}$$

$$i(\alpha U + \beta W - \omega)u + vDU + i\alpha p - (D^2 - k^2)\frac{u}{R} = 0 \tag{1.21}$$

$$i(\alpha U + \beta W - \omega)v + Dp - (D^2 - k^2)\frac{v}{R} = 0 \tag{1.22}$$

$$i(\alpha U + \beta W - \omega)w + vDW + i\beta p - (D^2 - k^2)\frac{w}{R} = 0 \tag{1.23}$$

where $D = \dfrac{d}{dy}$; $k^2 = \alpha^2 + \beta^2$

This linear system of ordinary differential equations can be combined to obtain the famous Orr-Sommerfeld equation:

$$D^4\phi - 2k^2D^2\phi + k^4\phi - iR[(\alpha U + \beta W - \omega)(D^2\phi - k^2\phi) - (\alpha D^2U + \beta D^2W)\phi] = 0 \tag{1.24}$$

with boundary conditions

$$\phi(0) = D\phi(0) = 0 \ ; \ \phi(y \to \infty) \to 0$$

For a Blasius boundary layer, equation (1.24) reduces to:

$$\left\{(D^2 - \alpha^2)^2 - iR\left[(\alpha U - \omega)(D^2 - \alpha^2) - \alpha(D^2U)\right]\right\}\phi = 0 \tag{1.25}$$

where the first mode eigenfunction is the Tollmien-Schlichting (T-S) wave. The higher modes are usually disregarded since they are greatly damped. The local normal mode for a Blasius flow is given in equation (1.26).

$$q'(x, y, t) = q(y)\exp(-\alpha_i x)\exp[i(\alpha_r x - \omega t)] + C.C. \qquad (1.26)$$

The spatial growth rate is given by $-\alpha_i$ and is a function of R and the reduced frequency $F = \omega/R = 2\pi f \nu / U_\infty^2$. The phase speed is represented by $c = \omega/\alpha_r$. The stability of the disturbances can be grouped into three classes depending on the sign of α_i. That is, if $\alpha_i < 0$ the disturbances are amplified and the flow is unstable. If $\alpha_i = 0$ there is no change and the flow is neutrally stable. Finally, if $\alpha_i > 0$ the disturbances are damped and the flow is stable.

The stability characteristics of such a system are represented by the neutral stability curve shown in Figure 1. At constant frequencies the amplitudes of the disturbances initially decay until further downstream the first unstable points are reached. This collection of points form what is called Branch I (left side) of the neutral stability curve. The amplitude then grows exponentially downstream of Branch I until Branch II (right side) is reached.

The amplitude ratio of the disturbance at two locations can be found using equation (1.27)

$$\frac{A}{A_0} = e^N \tag{1.27}$$

where A_0 is the amplitude of the disturbance at Branch I. The N-factor is given by equation (1.1) with x_0 corresponding to Branch I of the neutral stability curve.

Linear stability theory is in very good agreement with experimental results and demonstrates that the two-dimensional instability growth is well understood up until the onset of nonlinear and three-dimensional effects that will eventually breakdown the flow into turbulence. Further details in all aspects of linear stability theory are given by Mack (1984).

1.4.3. Receptivity

What is needed today for reliable transition prediction is the mechanism by which freestream disturbances create the initial instability waves inside the boundary layer. The role of receptivity is to determine how these external disturbances provide the initial amplitude, frequency and phase to the instability waves. Receptivity sources include surface roughness, surface geometry, freestream sound and freestream vorticity. A schematic of the receptivity problem for this experiment is shown in Figure 2.

The receptivity problem can be divided into two distinct classes: forced receptivity and natural receptivity. In forced receptivity the disturbances are introduced into the boundary layer with a wavelength similar to that of the instability. This forcing allows the direct excitation of the instability wave and provides a complete transfer of

energy. In contrast, natural receptivity occurs only after a wavelength-conversion process. For example, acoustic disturbances and freestream turbulence have wavelengths that differ to a large extent from those of the instabilities. Therefore, the energy from the freestream disturbances is not available to directly excite the instability waves.

Early attempts to solve the receptivity problem made use of the parallel assumption of the O-S equation and involved inhomogeneous boundary conditions at the wall (Gaster 1965, Mack 1975). This method was successful for the forced receptivity problem, but failed for natural receptivity. Saric et al. (1994) shows that the breakdown of the O-S equation lies in its parallel-assumption, which excludes the wavelength-conversion process.

Natural receptivity occurs essentially in two regions. Hence, it can be separated into two classes. The first is the body leading-edge region, where the mean flow changes rapidly in the streamwise direction and the non-parallel mean flow effects cannot be neglected, thus invalidating the parallel flow assumption of the O-S equation. Goldstein (1983) was the first to develop the correct asymptotic approximation to the Navier-Stokes equation: the linearized, unsteady, boundary-layer equation (LUBLE). Goldstein showed that close to the leading edge the LUBLE accurately describes the flow. Further downstream, the flow can be approximated by the classical large-Reynolds-number, small-wavenumber approximation of the O-S equation. Goldstein asymptotically matched these two regions and showed that the first Lam-Rott asymptotic eigensolution of the LUBLE, with coefficient C_1, matches the T-S wave that becomes unstable further

downstream in the O-S equation region. Consequently, the amplitude of the T-S wave is linearly proportional to C_1, which is called the *complex leading-edge coefficient*.

The second class of natural receptivity happens downstream of the leading edge, where local changes in surface geometry cause the mean flow to make quick adjustments. For this second mechanism, the correct asymptotic approximation is the triple-deck structure. The viscous flow in the lower deck satisfies the LUBLE, illustrating once more that the mean-flow non-parallel effects are required for the wavelength-conversion mechanism. A detailed discussion is given in Goldstein (1985).

1.5. Experimental and theoretical overview

A number of experimental and computational approaches to boundary layer receptivity to freestream sound have been developed over the years, and some of the more recent experiments have been conducted at Arizona State University, Unsteady Wind Tunnel.

Saric et al. (1995) examines the effect of acoustic forcing on a flat plate for two different leading edges. These leading edges consist of modified super ellipses (MSE) with aspect ratios of 20:1 and 40:1. In this experiment, continuous acoustic forcing is used to excite the T-S instability and determine the receptivity coefficient at Branch I at various frequencies. As a result of the continuous nature of the acoustic forcing, the acquired signal is composed of both the T-S and the Stokes waves. Thus, the waves have

to be separated using a complex-polar plot technique. In this manner, the amplitude and phase of the signal are plotted in the complex plane and the noise introduced by the Stokes wave as well as the sting vibration is subtracted, leaving only the T-S amplitude. Further details are given in Wlezien (1994) and Saric (1994, 1995).

The results of this experiment showed a narrow-frequency-band response that could not be reconciled with the theoretical (Kerschen et al. 1990) or computational (Fuciarelli & Reed 1994) results.

The inconclusive nature of these results provided the motivation for the development of a different technique using modulated acoustic bursts. Further experiments were conducted by Saric & White (1998) using bursts of sound at specific frequencies. Here the signal can be conditionally sampled by taking advantage of the disparity in the propagation speeds between the T-S wave and the freestream acoustic disturbance and its associated Stokes wave. In this manner, the slower T-S wave can be isolated from the Stokes wave and the T-S amplitude can be found directly. This is a much simpler method than other techniques previously used and offers the experimentalist a better understanding of the T-S response.

The results of this work revealed a more broadband distribution of the receptivity coefficients. However, these results still showed some focusing, although they were more consistent with theory and DNS.

Other approaches to the receptivity problem investigate the receptivity to freestream vorticity and take a step towards determining the receptivity to freestream turbulence with its broadband spectrum. Dietz (1999) performed experiments where the

wake from a vibrating ribbon, located upstream of a flat plate, is used to generate the freestream disturbance. He examined the effects of two dimensional roughness elements and their interaction with various single frequency and broadband forcing signals. The results demonstrated that receptivity to convected disturbances is the dominant mechanism responsible for the generation of T-S waves.

Initial receptivity models were developed for semi-infinite, zero-thickness flat plates (Goldstein 1983). However, historically, experiments have been performed on flat plates with parabolic or elliptic leading edges and finite thickness. Consequently, the majority of current analytical and computational efforts have adopted these more realistic geometries.

The theoretical work by Hammerton & Kerschen (1996) considered the effect of the nose radius of a parabolic leading edge. The radius of curvature r_n of the leading edge enters the equation as a Strouhal number $S=\omega\, r_n/U$ where ω is the frequency of the freestream disturbance. In addition, Hammerton & Kerschen (1997) studied the small-Strouhal number limit. Their results showed that for acoustic waves propagating parallel to the symmetric mean flow, the receptivity varies linearly with the Strouhal number.

An alternative model is the recent DNS of receptivity to acoustic disturbances on an elliptic leading edge undertaken by Wanderley & Corke (2001). These computations follow the spatial approach of Haddad & Corke (1998) previously used for parabolic bodies. The emphasis of this work is to simulate the experimental conditions of Saric et al. (1995) and Saric & White (1998). In addition, the results can be directly compared with the DNS of Fuciarelli et al. (2000). Branch I receptivity results revealed good

agreement with experiment over a small frequency band. Notwithstanding, the experiments show some frequency focusing that cannot be explained by the numerical simulation. For a comprehensive review of receptivity research the reader is referred to Saric et al. (2002).

1.6. Objectives

Receptivity experiments are highly sensitive and often produce inconclusive and ambiguous results (Wlezien 1994). Thus, they must be very well controlled. The objectives of the current research are as follows. The first is to properly characterize the experimental initial conditions, first by documenting the freestream turbulence at the ASU-Unsteady Wind Tunnel, and secondly, by establishing a reference Blasius flow on the flat plate. Previously, acoustic receptivity experiments have shown narrow-frequency focusing of receptivity coefficients while DNS and analytical models have predicted a more broadband behavior. For this reason, the second and primary goal of the current work is to produce leading-edge receptivity coefficients, via a frequency-domain pulsed-sound technique, that can be used to reconcile these contradictions between experiments and theoretical models.

1.7. Outline

Now that the literature has been reviewed and the experimental objectives have been defined, the details of the experimental set-up, model specifications, and facilities

are described in Chapter 2. Chapter 3 presents the experimental techniques and data acquisition methods. The results are presented and discussed in Chapter 4, including basic state, freestream-turbulence data and receptivity-coefficient measurements. Here, the results are also compared with linear stability theory. Finally, Chapter 5 provides concluding remarks.

CHAPTER 2

EXPERIMENTAL FACILITY

2.1. Unsteady Wind Tunnel

The experiments are performed in the Arizona State University Unsteady Wind Tunnel. The Unsteady Wind Tunnel is a low-speed, closed-return and low-turbulence facility originally designed and built by Dr.Philip Klebanoff at the National Bureau of Standards in Gaithersburg, Maryland. The tunnel was moved to Arizona State University in 1984 where, under the supervision of Dr. William Saric, it underwent extensive modifications to improve flow quality. The renovated facility became operational in 1987 and the turbulence levels were reduced to 0.02 % for a freestream speed of $U_\infty = 20$ m/s.

A 150 hp variable-speed, computer-controlled motor powers the wind tunnel with a 1.8 m diameter fan consisting of 9 blades and 11 stators. The facility can operate at speeds between 1 and 35 m/s and features a 1.4 m $\times$ 1.4 m $\times$ 5 m test section, and a contraction cone constructed from reinforced steel with a 5.3:1 contraction ratio. A schematic of the facility is shown in Figure 3.

As the name suggests, the tunnel can also operate in unsteady mode. Unsteady flow is achieved by diverting air from the main duct to a secondary duct equipped with oscillating shutters as shown in Figure 4. For this experiment, the wind tunnel is exclusively operated in steady mode. Further details of the facility are given by Saric (1992).

The tunnel's low-turbulence environment is ideal to conduct stability and receptivity experiments. Many factors contribute to lower the turbulence levels. A carefully designed contraction cone contoured by a fifth-degree polynomial eliminates curvature discontinuities at the ends. An aluminum honeycomb section is used to reduce large-scale disturbances and seven stainless steel screens, placed upstream of the contraction cone, are used to lower turbulence caused by smaller disturbances. In addition, both the test section and the motor housing are mounted on concrete foundations isolated from the rest of the facility and are connected to the rest of the tunnel by flexible couplings. This prevents motor and environmental vibrations from being transmitted to the test section. All these factors contribute to the overall quality of the facility for conducting receptivity experiments.

2.2. Traverse system

A three-dimensional, automated, and high-resolution traverse system is used in this experiment to precisely position a hotwire in the boundary layer. The traverse is step-motor driven, with the motors directly attached to high-precision leadscrews. A Compumotor CM4000 four-axis motion controller with four micro-stepping units is

linked to the computer system via General Purpose Interface Bus (GPIB) and controls the movements of the traverse. Safe and accurate positioning of the instrumentation is achieved through digital positioning feedback provided on all axes by optical encoders. The traverse specifications are given in Table 1.

Direction	X, axial	Y, wall normal	Z, vertical
Travel	1250 mm	100 mm	175 mm
Step Size	12 μm	0.7 μm	1.3 μm

Table 1. Traverse Capabilities.

The traverse mechanism is located outside the test section and supports an aluminum sting that holds a boundary-layer hotwire. The sting passes through a slotted Plexiglas window and the slot is sealed with a zipper. The X-traverse moves the entire traverse system in the axial direction along two stainless-steel rails using self-aligning ball bushings. Movements in the Z-direction are matched by two additional microstepping motors that provide synchronized movement of the window. Two views of the traverse system are depicted in Figures 5 and 6. Additionally, the traverse mechanism is enclosed in a pressure box so that there is no mass transfer through the sting access.

2.3. Computer system

Automation of the experiments is customary at the Unsteady Wind Tunnel. The need to combine many concurrent operations added to the vast amount of collected data requires the full automation of the process. The computer system at the Unsteady Wind Tunnel operates on two Pentium II personal computers. A Gateway E 5250 computer running the Red Hat 6.1 version of the Linux operating system primarily controls the experiments. Linux was chosen for its flexibility and robustness. Specifically, Linux is a multi-tasking, multi-user environment well known for its stability and therefore was deemed ideal for the complex real-time data acquisition, equipment control and data processing required.

Data communication with the external instruments, including the motor, is accomplished using a National Instruments GPIB card. The choice of GPIB provides high-speed communications and allows each instrument to be configured individually or be combined to form a complete acquisition and control system.

The integrity of the data is assured by a Redundant Array of Independent Disks (RAID) system. A second Pentium II IBM computer mirrors the capabilities of the main system and serves as a post-processing unit and backup system. Data acquisition and tunnel control software are written in-house using the C/C++ programming language. Details of the available C libraries can be found in Reibert (1996).

2.4. Instrumentation

A pitot-static tube, positioned at the ceiling, near the test section entrance, measures the tunnel's freestream velocity. The dynamic pressure is measured by a MKS 398HD 10-torr differential pressure transducer and the static pressure is measured with an MKS 390HA 1000-torr absolute pressure transducer. Both pressure transducers are outfitted with internal heaters, thus making them impervious to external temperature changes. Temperature is measured with a resistance temperature detector or RTD (Omega model DP116). All measurements are sent real-time to the computer system via GPIB.

Two hotwire probes provide velocity measurements for the freestream and the boundary layer. The probes used are Dantec 55P15 miniature boundary-layer sensors. These probes are specifically designed to allow easy access to the boundary layer and have a 1.25 mm long, 5 μm diameter platinum-plated tungsten wire. Each hotwire is connected to a Dantec 55M10 CTA, low-noise bridge.

Fluctuating velocity measurements are separated using a benchtop Kemo VBF-44 filter. The filter contains four 6th-order filters that can be used independently to create a 4 channel filter-amplifier, or in pairs to create 2 channels of bandpass, bandstop or other combinations. Each filter can be adjusted over a frequency range of 1 Hz to 255 kHz. The inputs have a gain of −10 to 40 dB and the outputs provide an additional −10 to 30 dB. The filter can be operated in stereo mode; in this mode the instrument creates two identical composite channels. This is useful for insuring that adjustments of the reference

channel bandpass will cause the other channel to retune automatically to preserve the selected response shape. The filter can be adjusted manually or through the built in GPIB interface.

Signals are acquired through two Iotech AD488/8SA analog-to-digital converters. Each A/D converter offers 8 differential input channels with 16-bit resolution. The input ranges are user-programmable for optimal resolution and range from $\pm$ 1 V to $\pm$ 10 V. Sampling rates range from 0.2 Hz to a maximum of 100 kHz and are also user-selectable.

2.5. Sound equipment

The pulsed-sound experiment involves generating very short acoustic input signals. A Hewlett-Packard function generator (model HP 33120A) is used to create three- to five-cycle sine waves at specific frequencies and amplitudes. The HP 33120A is a high-performance 15 MHz synthesized function generator with built-in arbitrary waveform capability and GPIB interface. The instrument can be configured to output a burst waveform with a specified frequency, amplitude and number of cycles. Standard waveforms include square, triangle, ramp, noise (Gaussian) and sine, among others. The frequency range for sine waveforms encompasses the 100 mHz to 15 MHz range. The sinewave spectral wave purity, into 50 Ohms, offers a total harmonic distortion of less than 0.04% for frequencies up to 20 kHz.

The signal is directly sent to five ADCOM GFA-555 high-current power amplifiers. The amplifiers are continually cooled with several fans to avoid a decrease in

performance as well as thermal overload. Under these conditions the amplifiers are power rated at 325 Watts continuous average power into 4 Ohms at any frequency between 20 Hz and 20 kHz with both channels driven at less than 0.04% total harmonic distortion. The signal to noise ratio is rated at −110 dB for operation at 200 Watts into 8 Ohms. The maximum input to the amplifiers should not exceed 5 Volts peak-to-peak.

The acoustic signal is broadcasted into the tunnel by an array of nine Mc-Cauley Sound speakers (model 6222). These high performance woofers are designed to reproduce low frequency signals and are 250 mm in diameter with a maximum power rating of 300 Watts. Figure 7 shows the response of the speakers as sound pressure level (SPL) versus frequency, for different amplitude signals.

The speakers are encased in individual boxes and mounted flush with the inside wall of the plenum to minimize disturbances to the flow. A schematic of the layout is shown in Figure 8.

In addition to hotwires, high sensitivity microphones can be used to measure SPL levels. The piezoelectric microphones, PCB 103A102, are acceleration compensated, with a 2 psi dynamic range, a 1500 mV/psi sensitivity and a rise time of less than one hundred microseconds. A unity-gain, battery-powered signal conditioner (model 480C02) provides 27 VDC, 2 mA constant-current power to the sensors enabling fast and highly sensitive measurements. For the present experiment he microphones were used as a means of comparison with the hotwire data.

2.6. Model configuration

2.6.1. *Flat plate*

The ASU-UWT flat plate has been previously utilized by several researchers, including Saric et al. (1995), Krutckoff (1996) and White et al. (2000), to perform leading-edge receptivity experiments to sound.

The flat plate is made of an Aluminum-Nickel alloy, and it is ground flat so that variations in thickness are minimized. Models made of rolled Aluminum should be avoided since they typically present periodic pressure disturbances. The model is 9.53 mm thick, 4000 mm long, and 1370 mm wide. The surface is hand-polished to 0.2 μm RMS to remove surface roughness as a potential receptivity source.

The flat plate is mounted vertically in the test section, approximately 780 mm from the end of the contraction cone. It is held in place by ten movable brackets and it is mounted off-center (54:46) in the test section. Mounting the plate off center from the line of symmetry permits the reduction of the effects of streamwise circulation cells that often occur inside the test section. The plate is outfitted with two rows of 25 static pressure ports regularly spaced on either side of the centerline. As a result, the pressure distribution along the plate can be measured and used as a preliminary method to align the plate for Blasius flow. A 500 mm flap with a sharp trailing edge is hinged to the end of the plate, and can be adjusted to control the location of the stagnation line.

2.6.2. *Leading edge*

Each end of the plate is machined with a distinct leading edge. The test leading edge is a 20:1 aspect ratio, modified super ellipse (MSE) and the other is a 40:1 MSE. These geometries were originally used by Lin et al. (1992) and Fuciarelli & Reed (1994) in a Direct Numerical Simulation (DNS) of the receptivity mechanism. The modified super ellipse is described by equation (2.1)

$$\left(\frac{y}{b}\right)^2 + \left(\frac{a-x}{a}\right)^{2+\left(\frac{x}{a}\right)^2} = 1 \tag{2.1}$$

where a is the major axis and b is the minor axis. For the experimental configuration 20:1 MSE, a is 95.3 mm and b is 4.76 mm.

The MSE profile is chosen to ensure that there is no curvature discontinuity at the interface between leading edge and flat plate, and to move the minimum pressure region towards the leading edge.

CHAPTER 3

EXPERIMENTAL TECHNIQUES

3.1. Hotwire compensation and calibration

The hotwire anemometer has been successfully used for many years to measure small fluctuating velocity components. This feature is of special interest because of the extreme sensitivity of this experiment. For optimal response, the hotwires are calibrated daily in the same reference position in order to avoid calibration drift.

A careful description and discussion of the calibration technique is given by White (2000). The reader is referred to this source and its references for an in-depth analysis. Instead, a brief account of the procedure is given below.

The calibration procedure includes not only velocity but also accounts for temperature effects, since the Unsteady Wind Tunnel lacks a cooling system. Effectively the temperature rise during lengthy or high Reynolds number experiments can be greater than 20°C and as a result cannot be neglected.

The velocity calibration is performed by sampling the voltages from the constant temperature anemometer and calibrating them versus both the velocity measured by a

pitot-static tube and the temperature recorded by an RTD thermometer. The procedure is fully automated and consists of three main steps. First, the tunnel is run through a range of speeds, in general between 2 and 27 m/s in intervals of 2 to 3 m/s. Second, the tunnel is operated at high speed in order to raise the temperature by a specified amount, typically 5°C. This allows for the frictional heating of the closed loop tunnel to be accounted for in the calibration procedure. Finally, once the target temperature is reached, the velocity is decreased and the temperature and voltages are recorded once more against the pitot-tube velocity.

Using the voltages obtained for a given velocity at low and high temperatures, a temperature compensation coefficient is obtained. These compensation coefficients allow ,in turn, the voltage data to be corrected for any temperature effect. As a result, the velocity is calibrated as a function of temperature compensated voltage. The resulting calibration curves are fitted using a Levenberg-Marquardt least-squares nonlinear fit. A typical calibration curve is shown in Figure 9. It should be noted that the more traditional polynomial fit is omitted in favor of the nonlinear fit since this last method provides a more accurate model. For this reason, a small temperature rise can be used and yields good results.

3.2. Boundary layer profiles

Boundary-layer mean velocity profiles are acquired using the hotwire probe. These profiles serve two main purposes. First, they permit locating the surface of the

plate in order to zero the coordinates of the traverse mechanism. Second, they yield the shape factor $H = \delta^*/\theta$, which is an accurate means for establishing Blasius flow.

Using the boundary-layer profiles to locate the wall involves an automated process controlled by a stepping algorithm. The algorithm divides the boundary layer scans into several regions, as the hotwire is moved in the wall-normal (Y) direction, from a point outside of the boundary layer to a point within 100-150 µm of the surface of the plate. These different regions are necessary to guarantee an adequate resolution, as well as to minimize the risk of breaking the hotwire against the surface of the plate.

The measurement is started outside of the boundary layer, where the hotwire is adjusted manually to within 5 or 6 mm of the model. In this region the traverse moves in the Y direction using relatively large steps. When the probe enters the boundary layer, the step size is gradually scaled with u/Ue. In addition, when $u/Ue < 0.5$, an estimate of the hotwire distance from the plate is extrapolated for each of the data points, through a linear least squares fit. The distance to the wall is calculated by subtracting the extrapolated wall position from the traverse location that can be controlled precisely but is not referenced to the plate. The scan is ended when the distance reaches a nominal value, typically 125 µm. In addition, a bailout value of 15% of u/Ue is used as a supplementary precaution.

The boundary layer velocity scans are also used to compute the displacement thickness and the momentum thickness shown in equations 3.1 and 3.2.

$$\delta^* = \int_0^\infty \left(1 - \frac{u}{U_e}\right) dy \qquad (3.1)$$

$$\theta = \int_0^\infty \frac{u}{U_e}\left(1 - \frac{u}{U_e}\right) dy \qquad (3.2)$$

Their ratio, called the shape factor, is then used to establish the Blasius character of the boundary layer. This procedure is implemented through a Simpson's rule numerical integration. Multiple streamwise locations are inspected and the plate is fine-tuned until   the shape factor approaches the Blasius value of $H = 2.59$ for all boundary-layer velocity scans.

3.3. Virtual leading edge

There is a small region in the neighborhood of the leading edge where there exists a pressure gradient followed by a pressure recovery zone. The streamwise pressure gradient arises from the geometry of the flat plate (i.e., finite thickness and elliptical leading edge). Fortunately this pressure gradient disappears over a small region, and downstream of the recovery zone a Blasius flow develops. However, one consequence of this phenomenon is an apparent shift in the origin of the boundary layer. The difference between the geometric origin of the plate and the apparent origin of the boundary layer is denoted as the *virtual leading edge.*

The location of the virtual leading edge can be calculated from the mean velocity profiles as:

$$x_v = x - \frac{\theta^2 U_\infty \times 10^6}{0.441\nu}$$

(3.3)

where x is the streamwise location of the boundary layer scan, ν is the kinematic viscosity and θ is the momentum thickness for Blasius flow as shown previously in equation (3.2). All measurements and calculations in this experiment are referenced to the virtual leading edge.

3.4. The pulsed-sound technique

The pulsed-sound technique was developed to prevent the superposition of the Stokes and the T-S waves that was inherent in previous experiments using continuous acoustic forcing. This new technique was first proposed by Saric (1995) and has been recently used in a study of receptivity to large amplitude-sound (Saric & White 1998). The technique has also been employed to examine the effects of acoustic disturbances on transition for an unswept two-dimensional wing (Kanner & Schetz 1999).

The pulsed-sound experiment consists of introducing short acoustic bursts, broadcasted via an array of nine speakers, into the test section. The acoustic wave is measured in the freestream by one hotwire while, within the boundary layer, a second

hotwire samples first the corresponding Stokes wave, followed a fraction of a second later by a T-S wave. A typical time trace is shown in Figure 10. The Stokes wave is observed first since it travels at sonic speed whereas the observed T-S wave, according to linear theory, travels at a fraction of the freestream velocity. This delay permits the direct measurement of the T-S amplitude. However, it is necessary to take into account reflections of the original acoustic pulse.

Reflections originate from the diffuser, just aft of the test section, as well as from the turning vanes and the end-wall downstream of the test section. This reverberation is observed as extra cycles in the freestream wire, which are mirrored within the boundary layer by extra cycles in the Stokes wave. Separation of these reflected waves is essential since it is believed that receptivity is greater for upstream-traveling waves than for the original downstream-traveling waves (Kerschen 1990).

To limit the detrimental effects of the reflections, a data-acquisition window is established. The detection of the input acoustic wave triggers the windowing function and, in this manner, the T-S and acoustic signals are automatically extracted from the time traces. The acquisition window is first adjusted by manually locating the end of the waveforms and is closely monitored thereafter. A comparison between the velocity measurements and the windowed data is shown in Figure 11. The extra cycles are excluded by limiting the length of the signal and, consequently, the sampling time. If necessary, the extracted signals are padded with zeros to maintain the time scale.

One of the shortcomings associated with the pulsed-sound technique is its intrinsic limited frequency resolution due to its brief time history. In the spectral domain,

the frequency resolution is the inverse of the sample length. Thus, a wave packet will, because of its short duration, typically a few hundred milliseconds, have its energy spread out over a wide frequency range. Furthermore, the energy at any one particular frequency will be low. Consequently, a large number of ensemble averages are necessary to achieve the best possible results.

3.5. Branch I receptivity coefficients

To obtain the strongest possible disturbance amplitude, the linear growth of the T-S instability between Branch I and Branch II is used to strengthen the boundary-layer signal. T-S waves are measured near Branch II and linear stability theory is used to scale the disturbance amplitude back to Branch I. The T-S amplitude at Branch I is normalized with the acoustic amplitude measured in the leading-edge plane. This ratio defines the receptivity coefficient as shown in equation (3.4).

$$K_S = \frac{\left| u'_{TS} \right|_I}{\left| u'_{ac} \right|_{LE}} \tag{3.4}$$

The amplitudes are found from the conditionally sampled sound pulses, using the magnitude of the complex Fourier coefficient for each frequency present in the wave packet.

CHAPTER 4

RESULTS

4.1. Base flow

4.1.1. Symmetric flow

As a first step towards the establishment of a Blasius flow the trailing-edge flap is used to control the stagnation point and guarantee an unseparated leading edge. The symmetric streamline is accomplished by adjusting the flap to an angle that generates a zero differential pressure between the two sides of the plate. The differential pressure is measured using two pairs of static pressure ports placed near the leading edge. Initially, the static ports on the top of the plate are used. The flap setting is varied and the differential pressure is recorded for a variety of freestream velocities as shown in Figure 12. Next, the bottom static ports are used and the process is repeated. Figure 13 illustrates the differential pressure versus flap angle for the bottom static ports. For symmetric flow the flap angle is set to 1 degree. It should be noted that the boundary layer on the backside of the plate was tripped using Velcro strips in order to fix the transition location.

Note also, that the flap setting is insensitive to Reynolds number. Consequently, the 1-degree setting is used independent of freestream speed.

4.1.2. *Shape factors*

As described in section 3.2. a more rigorous characterization of the Blasius character of the flow is to compute the shape factor at multiple streamwise locations, and adjust the plate until the shape factor is in accord with the theoretical Blasius value of H = 2.59.

This was accomplished by performing multiple boundary-layer scans, calculating the shape factor for each profile, and adjusting the plate using the movable brackets. The process was iterated until the value of the experimental shape factors were $H = 2.59 \pm 1\%$ as shown in Table 2.

Speed [m/s]	x_v [m]	Shape Factor
8	0.10	2.57
12	0.08	2.59
15	0.09	2.59
18	0.06	2.58
21	0.04	2.57

Table 2. Experimental shape factor and virtual leading edge for different speeds and streamwise locations.

Note that the corresponding virtual leading edge is calculated as described earlier in equation (3.3).

The excellent agreement with theory is manifested in Figure 14, where the theoretical Blasius profile is compared with the experimental data at selected streamwise locations, and at different freestream velocities. Note that the wall-normal coordinate is the appropriate dimensionless similarity variable η.

4.1.3. *Freestream disturbances*

Receptivity experiments are very sensitive and initial high levels of freestream turbulence can accelerate the transition process as well as conceal the T-S waves. Therefore, it is paramount to carefully document the tunnel's background fluctuations. In addition, this turbulence information is needed to accurately compare data from different wind tunnels.

The freestream turbulence is recorded for three different bandpass ranges in order to encompass in detail the regions of amplified T-S waves. These fluctuation levels are measured for a series of speeds (8-21 m/s) since the amplitudes increase with tunnel velocity. Figures 15-19 show the power spectral density of the u' fluctuation obtained for 8 m/s with a 1-450 Hz bandpass. The data is acquired with a single hotwire sampling for 30 seconds at 1 kHz. These spectra show a majority of the energy in the lower frequencies below the T-S band. Figures 20-24 show the power spectral density for the same speeds but with a 4-1000 Hz bandpass. Here, the data was acquired for 30 seconds at 5 kHz. Again, we see a low amount of energy present in the 50-150 Hz range of amplified T-S waves. Finally, Figures 25-29 shows the power spectral density for the

same speeds but with a 10-1000 Hz bandpass. The sampling parameters are the same as

for the previous case. The disturbance amplitudes for these three cases are summarized in

Table 3.

Speed [m/s]	u'/U_0 [%]	Bandwidth
8	0.039	
12	0.038	
15	0.046	1 Hz – 450 Hz
18	0.052	
21	0.064	
8	0.032	
12	0.029	
15	0.030	4 Hz – 1000 Hz
18	0.031	
21	0.036	
8	0.032	
12	0.028	
15	0.029	10 Hz – 1000 Hz
18	0.030	
21	0.033	

Table 3. Freestream disturbance measurements.

It is apparent from these results that the u' fluctuations are significantly higher for

the 1-450 Hz bandwidth. This shows not only that most of the energy resides in the low

frequency, less than 4 Hz, but it also emphasizes the importance of specifying the

frequency bandwidth when quoting freestream turbulence levels.

It should be noted that the u' fluctuations are quantitatively similar to those given

by Krutckoff (1996). However, the fluctuations are higher than those reported by

Mousseux (1988). At this time, it is assumed that changing the fan blade angles could improve the overall freestream disturbance levels.

To further understand the background freestream turbulence, the blade and stator blade passing frequencies are recorded for all speeds considered in this experiment as shown in Table 4.

Speed [m/s]	Blade frequency [Hz]	Stator frequency [Hz]
8	63	78
12	91	114
15	116	145
18	137	172
21	161	198

Table 4. Blade and stator passing frequencies.

The disturbances generated by the fan at the frequencies shown in the previous table appear as small peaks in the freestream turbulence spectrums. These peaks can be seen for the different speeds on the 4-1000 Hz bandpass spectra. It should be noted that the disturbance levels generated from this sources are of the same order of the noise; therefore they should not play a major role in the experiment.

During the course of the receptivity experiments, diverse attempts were made to cancel or limit the reflections of acoustic waves. To this avail, the tunnel's downstream wall was covered with acoustic absorbing foam. After installation, the freestream turbulence measurements were repeated to quantify the effect of the new configuration. Figures 30-44 duplicate the preceding freestream turbulence measurements. These spectra are presented mainly for completeness. However some interesting changes are apparent between the two configurations as shown in Table 5.

Speed [m/s]	u'/U_0 [%]	Bandwidth
8	0.040	
12	0.038	
15	0.047	1 Hz – 450 Hz
18	0.048	
21	0.064	
8	0.035	
12	0.031	
15	0.032	4 Hz – 1000 Hz
18	0.037	
21	0.040	
8	0.033	
12	0.030	
15	0.030	10 Hz – 1000 Hz
18	0.035	
21	0.039	

Table 5. Freestream disturbance measurements with acoustic foam.

The u' fluctuation amplitudes have moderately increased. However, upon close inspection of the frequency content, some peaks in the 100 Hz range have been attenuated. This can be clearly seen while comparing the 80-100 Hz ($57< F <72$) range between Figures 16 and 31. As before, a very small amount of energy is present in the range of amplified T-S waves and it is believed that the use of acoustic absorbing foam together with the fine-tuning of the blade angles would result in even lower freestream turbulence levels at this facility.

4.1.4. *Transition Reynolds number*

As an ultimate test of the flow quality, the transition Reynolds number was determined on the flat plate. This was done by ramping the tunnel's speed while leaving a hotwire at a fixed height inside the boundary layer. The velocity ratio u/U_∞ is plotted versus Re_x until a large rise in velocity is seen, indicating the onset of transition (Figure 45). Since transition occurs over a finite length, the exact transition location cannot be determined. Therefore, the transition Reynolds number is estimated as the Re_{tr} corresponding to the intersection of the lines given by the slopes of the initial increase in velocity and the transition area. An average value of $Re_{tr} = 2.5 \times 10^6$ was measured, indicative of low freestream turbulence. However, this value is considerably different than $Re_{tr} = 3.5 \times 10^6$ measured by Mousseux (1988). This discrepancy can be partly attributed to higher freestream turbulence levels currently present at this facility. However, as discussed in the section 4.1.3. changes in the fan blade pitch angles combined with the used of acoustic absorbing foam may alleviate this problem.

4.1.5. *Acoustic field*

Sound pressure levels inside the test section are measured with a hotwire placed in the freestream. The measured velocity fluctuations are converted to a pressure perturbation as shown in equation (4.1)

$$p' = u'_{rms}\, \rho c \qquad (4.1)$$

where ρ is the density and c is the local speed of sound. The SPL level is defined generally by

$$SPL = 10\ \log\left(\frac{p'}{p_{ref}}\right)^2 \qquad (4.2)$$

where p_{ref} is a reference pressure taken as 20×10^{-6} Pa.

The uniformity of the acoustic field has been verified in the past for this same experimental setup (Saric et al. 1995). In addition, special precautions have been taken to prevent vibrations of the leading edge, and a laser vibrometer has been used to guarantee that the vibrations are of no consequence (White et al. 2000).

4.2. Disturbance State

For this experiment, the freestream hotwire is situated even with the leading edge, behind the plate, and the boundary layer hotwire is positioned on the sting near Branch II for the central input frequency. The input wave packet consists of a 5-cycle sine wave. Also, the pulsed-sound technique described in section 3.4. was used to obtain the T-S wave amplitudes.

4.2.1. *Tollmien-Schlichting modeshapes*

Comparisons of the experimental and theoretical modeshapes are shown in Figures 46 and 47. Results are presented for two different freestream speeds (12 m/s and 15 m/s). The collapse of the measured data with the theoretical data indicates good agreement between experimental results and linear stability theory. Accord between theory and experiment is essential, because LST is used when determining receptivity coefficients to scale the measured signal to Branch I.

The linear behavior is also evident from Figures 48 – 50. Here, the disturbance amplitude is shown for varying freestream pressure levels. The boundary-layer response was found to be linear for all acoustic forcing levels considered.

4.2.2. *Receptivity measurements*

Receptivity coefficients for $U_\infty = 8$ m/s and 15 m/s are shown in Figures 51 and 52. These figures include a quantitative comparison between the present results, and the experiments of Saric et al. (1995). In addition, the receptivity results shown for 8 m/s are compared to the numerical results of Fuciarelli et al. (2000). Figures 53 and 54 show the magnitude-averaged power spectral density for the freestream and boundary layer signals. Both results show receptivity over a wide frequency range. Consequently, they do not exhibit the focusing behavior present in previous experiments as can be clearly

seen in the comparison. Furthermore, the DNS of Fuciarelli et al. (2000) shows $(K_s)_1 =$ 0.048 at 8 m/s, which is in good agreement with the experiment. However, an amplification of the receptivity coefficients can be seen for changes in reduced frequency over the measured frequency band. For the 8 m/s case, the receptivity coefficients grow for increasing reduced frequency. This trend follows the computational results of Wanderley & Corke (2001) for a 20:1 MSE leading edge. These numerical results show a local maximum at approximately $F = 95$ and $(K_s)_1 = 0.047$. Note that this value agrees with the experimental result as depicted in the receptivity curve. Moreover, the receptivity curve also qualitatively captures the drop off observed in the DNS. Moving to the 15 m/s case, an upward shift of the receptivity coefficients for decreasing reduced frequency is also evident in the receptivity curve. This feature may be partly explained by the variation of the instability response with changes in reduced frequency. However, there is another factor that must be taken into account. As a consequence of the pulsed-sound technique, the measured signal becomes difficult to characterize from the background noise level as the receptivity coefficients move away from the center frequency. One aspect of this behavior is an upward drift of the measured $(K_s)_1$ values close to the ends of the receptivity curves. This behavior is also apparent in Figure 55 which depicts the receptivity coefficients for $U_\infty = 12$ m/s. For this case two input frequencies were used to span a wider receptivity zone. The corresponding PSDs are shown in Figures 56 and 57. Once more, the receptivity coefficient variation with frequency is much broader than the previous results of Saric et al. (1995) and Saric & White (1998). Furthermore, there is not any apparent frequency focusing. Receptivity

results by White et al. (2000) showed a similar broadband behavior, however they were significantly lower. It is conjectured that this may be the result of phase inconsistencies in the boundary layer signal over the large number of complex ensemble-averages. As a result, the magnitude of the receptivity coefficients would be lower. Another feature shown in Figure 55 is the difficulty in attaining a continuous receptivity curve when using multiple input frequencies. The disparity in slopes can be traced in part to the extreme sensitivity to environmental conditions such as temperature, viscosity, and reflected waves. This disparity shows that despite the great care taken during each experiment it is difficult to reproduce results since the T-S amplitudes are very small and are highly influenced by diverse environmental effects.

A summary list of receptivity coefficients for 8 m/s, 12 m/s and 15 m/s is shown in Table 6. It should be noted that the receptivity coefficients for a given freestream speed are functions of the reduced frequency, F, defined in section 1.4.2.

The leading edge receptivity dependence on frequency was sought at higher freestream speeds and different reduced frequencies. However, this was not possible due to some unavoidable circumstances, primarily due to reflections of the input acoustic signal. These echoes, mainly generated at the downstream corner of the tunnel, altered the T-S signal. The contaminated signal was prevalent for higher speeds and covered the entire receptivity zone.

A passive wave cancellation scheme was attempted using acoustic absorbing foam. However, the results were meager, because of the inherent complexity in dampening low frequencies.

U_∞ [m/s]	F	R_I	N	$(K_\mathrm{s})_\mathrm{I}$	$\sigma_{K\mathrm{s}}$
	83.8	464	1.88	0.039	0.003
	87.8	453	1.90	0.037	0.003
8.0	91.8	442	1.87	0.039	0.004
	95.8	433	1.78	0.043	0.005
	99.8	424	1.65	0.052	0.009
	45.7	645	3.94	0.050	0.012
	47.6	630	4.08	0.045	0.009
	49.4	617	4.16	0.042	0.008
	51.2	605	4.20	0.041	0.007
	53.1	593	4.19	0.043	0.007
	54.8	583	2.82	0.047	0.006
12.0	54.9	582	4.13	0.048	0.008
	56.6	572	2.93	0.044	0.005
	58.4	563	3.01	0.041	0.005
	60.3	553	3.08	0.039	0.005
	62.1	544	3.13	0.040	0.005
	63.9	536	3.14	0.039	0.006
	65.8	527	3.13	0.041	0.005
	42.8	669	3.80	0.066	0.007
	44.0	659	3.90	0.062	0.006
	45.2	648	4.02	0.056	0.006
	46.3	640	4.10	0.052	0.005
15.0	47.5	631	4.18	0.048	0.005
	48.7	622	4.23	0.046	0.005
	49.9	614	4.26	0.045	0.005
	51.1	606	4.28	0.044	0.005

Table 6. Receptivity coefficient dependence on frequency.

CHAPTER 5

CONCLUSIONS

In this experiment, receptivity to high amplitude sound was studied on a Blasius

boundary layer. A flat plate with exceptional surface finish was used in conjunction with

a 20:1 MSE leading edge. The MSE ensures that there was no curvature discontinuity at

the interface between leading edge and flat plate, therefore limiting the receptivity

sources.

A rigorous methodology was followed to guarantee the establishment of a Blasius

flow. First, a symmetric flow was achieved by adjusting a trailing edge flap to a one-

degree angle. Then, multiple boundary-layer scans and plate adjustments were used to

attain an experimental shape factor of $H = 2.59 \pm 1\%$. The mean flow results were

consistent throughout the tests and fully agreed with theory. In addition to achieving a

Blasius mean flow, particular care was taken to document the freestream disturbance

levels for various experimental conditions. Low turbulence levels were observed across

the experimental velocity range. The measurements showed $u'/U_o = 0.038$ % at 12 m/s

for a 1-450 Hz bandwidth. Furthermore, most of the energy was contained below

4 Hz, which is away from the frequency range of interest. Finally, the transition Reynolds number was determined on the flat plate. An average value of $Re_{tr} = 2.5 \times 10^6$ was measured, suggesting low levels of freestream turbulence.

A pulsed-sound technique was successfully employed to extract uncontaminated Tollmien-Schlichting waves and generate measurements of receptivity coefficients. The signals were converted to the frequency domain, by a fast Fourier transform, where the magnitude of the ensemble-averaged Fourier coefficients was used to calculate the receptivity coefficients. This method proved to be more reliable than the complex averaging approach that is prone to errors due to phase inconsistencies in the boundary layer signal

Previous experiments had suggested that the receptivity coefficients exhibited a frequency-focusing effect. The results presented here show that receptivity is broadband. This broadband behavior is consistent with DNS and analytical models. In particular, the receptivity coefficients exhibit good agreement with the numerical results of Fuciarelli et al. (2000), and also reflect qualitatively the behavior shown in the DNS by Wanderley & Corke (2001), as can be seen in Table 7.

DNS 20:1 MSE Fuciarelli, Reed & Lyttle (2000)	DNS 20:1 MSE Wanderley & Corke (2001)	Experiment 20:1 MSE Saric & White (1998)	Present Experiment 20:1 MSE
$(K_s)_1 = 0.048$ over $F = 82 - 86$	$(K_s)_1 = 0.03 - 0.047$ over $F = 73 - 103$	$(K_s)_1 = 0.05$ over $F = 82 - 86$	$(K_s)_1 = 0.037 - 0.043$ over $F = 83.8 - 99.8$

Table 7. Comparison of Branch I receptivity coefficients with DNS and experiments of Saric & White (1998).

While the results from this experiment showed that progress has been made using the pulsed-sound technique, there are still several limitations. These limitations include high sensitivity to environmental factors such as tunnel heating and the prevalence of reflected waves. Several attempts were made to mitigate the effects of the reflections, including passive means of wave cancellation using acoustic absorbing foam. Regrettably, no measurable improvement was observed. However, the agreement between theory and experiment is reasonable considering the limitations encountered and the extreme sensitivity of the instability.

REFERENCES

BUSHNELL, D. M., MALIK, M. R. & HARVEY, W. D. 1989 Transition prediction in external flows via linear stability theory. In *IUTAM Symp. Transsonicum III* (ed. J. Zierep, H. Oertel), pp. 225-242.

CRAIK, A. 1971 Nonlinear resonant instability in boundary layers. *J. Fluid Mech.* **50**, 393-413.

DIETZ, A. J. 1999 Local boundary-layer receptivity to a convected free-stream disturbance. *J. Fluid Mech.* **378**, 291-317.

FUCIARELLI, D. A., REED, H. L. & LYTTLE, I. 2000 Direct numerical simulation of leading-edge receptivity to sound. *AIAA J.* **38** (7), 1159-1165.

FUCIARELLI, D. A. & REED, H. L. 1994 Direct numerical simulations of leading-edge receptivity to freestream sound. *Application of Direct and Large Eddy Simulation to Transition and Turbulence, AGARD CP* 551.

GASTER, M. 1974 On the effects of boundary-layer growth on flow stability. *J. Fluid Mech.* **66**, 465-480.

GASTER, M. 1965 On the generation of spatially growing waves in a boundary layer. *J. Fluid Mech.* **22**, 433-441.

GOLDSTEIN, M. E. 1983 The evolution of Tollmien-Schlichting waves near a leading edge. *J. Fluid Mech.* **127**, 59-81.

GOLDSTEIN, M. E. 1985 Scattering of acoustic waves into Tollmien-Schlichting waves by small streamwise variations in surface geometry. *J. Fluid Mech.* **154**, 509-529.

HADDAD, O. & CORKE, T. C. 1998 Boundary layer receptivity to freestream sound on parabolic bodies. *J. Fluid Mech.* **368**, 1-26.

HAMMERTON, P. W. & KERSCHEN, E. J. 1996 Boundary-layer receptivity for a parabolic leading edge. *J. Fluid Mech.* **310**, 243-267.

HAMMERTON, P. W. & KERSCHEN, E. J. 1997 Boundary-layer receptivity for a parabolic leading edge. Part 2. The small Strouhal number limit. *J. Fluid Mech.* **353**, 205-220.

HERBERT, T. 1983 Subharmonic three-dimensional disturbances in unstable plane shear flows. *AIAA Paper* 83-1759.

KANNER, H. S. & SCHETZ, J. A. 1999 The evolution of an acoustic disturbance up to transition in the boundary layer on an airfoil. *AIAA Paper* 99-3791.

KERSCHEN, E. J., CHOUDHARI, M. & HEINRICH, R. A. 1990 Generation of boundary instability waves by acoustic and vortical freestream disturbances. *Laminar-turbulent Transition*, vol. 3 (Eds. Arnal, R. Michel), pp. 477-88.

KERSCHEN, E. J. 1990 Boundary-layer receptivity theory. *Appl. Mech. Rev.* **43**, S152-S157.

KLEBANOFF, P., TIDSTROM, K. & SARGENT, L. 1962 The three-dimensional nature of boundary-layer instability. *J. Fluid Mech.* **12**.

KRUTCKOFF, T. K. 1996 Experiments on boundary-layer receptivity to sound. M.S. thesis, Arizona State University.

LIN, N., REED, H. L. & SARIC, W. S. 1992 Effect of leading edge geometry on boundary-layer receptivity to freestream sound. In *Stability, Transition and Turbulence* (ed. M.Y. Hussaini, A. Kumar & C. L. Streett), pp. 421-440.

MACK, L. M. 1984 Boundary-layer linear stability theory. *Special Course on Stability and Transition of Laminar Flows, AGARD R-709.*

MACK, L. M. 1975. Linear stability theory and the problem of supersonic boundary-layer transition. *AIAA J.* **13**, 278.

MORKOVIN, M. V. 1969 On the many faces of transition. In *Viscous Drag Reduction* (ed. CS Wells), pp. 1-31. New York: Plenum.

MORKOVIN, M. V. 1993 Bypass-transition research: Issues and philosophy. *Instabilities and Turbulence in Engineering Flows* (ed. D. E. Ashpis, T. B. Gatski & R. Hirsh), pp. 3-30.

MOUSSEUX, M. 1988 Flow-quality improvements in the Arizona State University Unsteady Wind Tunnel. M.S. thesis, Arizona State University.

PFENNINGER, W. 1977 Laminar flow control-laminarization. In *Special Course on Concepts for Drag Reduction, AGARD R-654.*

REIBERT, M. S. 1996 Standard C libraries and codes: A guide to programming at the ASU Unsteady Wind Tunnel. Arizona State University. Unsteady Wind Tunnel Internal Documentation.

RESHOTKO, E. 1994 Boundary layer instability, transition, and control. *AIAA Paper* 94-0001.

SARIC, W.S. 1994 Low-speed boundary-layer transition experiments. In *Aspects of Transition to Turbulence: Experiments, Theory & Computations.*

SARIC. W. S. & NAYFEH, A. H. 1977. Nonparallel stability of boundary layers with pressure gradients and suction. *AGARD CP* 224.

SARIC, W. S., REED, H. L. & ARNAL, D. 1996 Linear stability theory applied to boundary layers. *Ann. Rev. Fluid Mech.* **28** 389-428.

SARIC, W. S., REED, H. L. & KERSCHEN, E. J. 1994 Leading edge receptivity to sound: experiments, DNS, and theory. *AIAA Paper* 94-2222.

SARIC, W. S., WEI, W., RASMUSSEN, B. K.& Krutckoff, T. K. 1995 Experiments on leading-edge receptivity to sound. *AIAA Paper* 95-2253.

SARIC, W. S. & WHITE E. B. 1998 Influence of high-amplitude noise on boundary-layer transition to turbulence. *AIAA Paper* 98-2645.

SARIC, W. S. 1992 The ASU transition research facility. *AIAA Paper* 92-3910.

SARIC, W. S., HOOS, J. A. & RADEZTSKY, R. H. 1992 Boundary-layer receptivity of sound with roughness. In *Boundary Layer Stability and Transition to Turbulence.* ASME FED, vol.114, pp. 17-22.

SARIC, W. S., REED, H. L. & KERSCHEN, E. J. 2002 Boundary-layer receptivity to freestream disturbances. *Ann. Rev. Fluid Mech.*

SMITH, A. M. O. & GAMBERONI, N. 1956 Transition, pressure gradient and stability theory. *Tech. Rep..* Douglas Aircraft Company.

THOMAS, A. S. W. 1985 Aircraft drag reduction technology-a summary. In *Special Course on Aircraft Drag Prediction and Reduction, AGARD R-723.*

VAN IGEN, J. L. 1956 A suggested semi-empirical method for the calculation of the boundary-layer transition region. *Tech. Rep.* UTH1-74, Univ. of Tech., Delft, Netherlands.

WANDERLEY, J. B. V. & CORKE, T. C. 2001 Boundary layer receptivity to free-steam sound on elliptic leading edges of flat plates. *J. Fluid Mech.* **429**, 1-29.

WHITE, E. B., SARIC, W. S. & RADEZTSKY R. H. 2000 Leading-edge acoustic receptivity measurements using a pulsed-sound technique. Laminar-Turbulent Transition vol. 5 (ed. H. F. Fasel & W. S. Saric), pp.103-110.

WHITE, E. B. 2000 Breakdown of crossflow vortices. PhD thesis, Arizona State University.

WLEZIEN, R. W. 1994 Measurement of acoustic receptivity. *AIAA Paper* 94-2221.

APPENDIX A

FIGURES
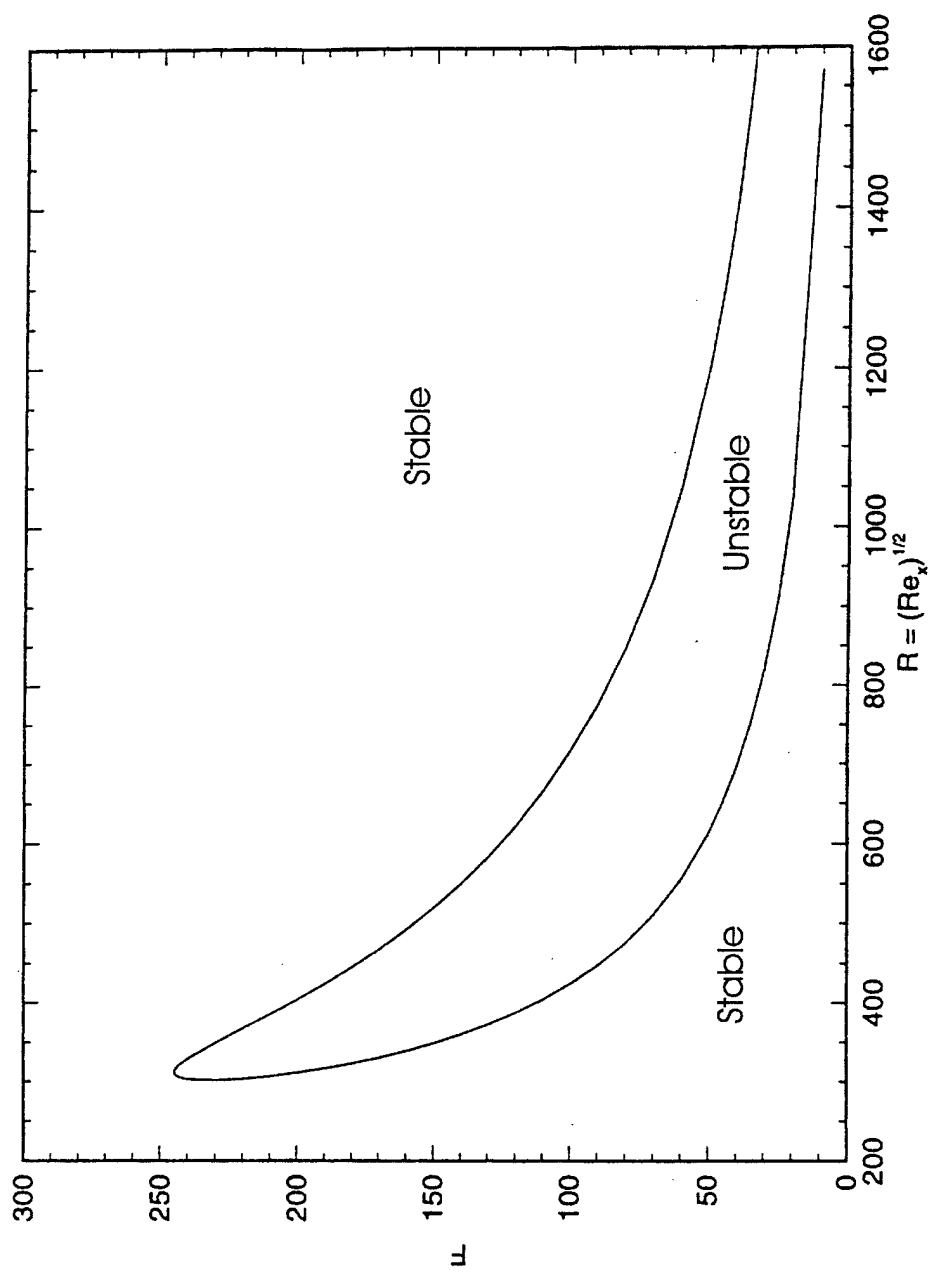
Figure 1. Neutral stability curve for a Blasius boundary layer.
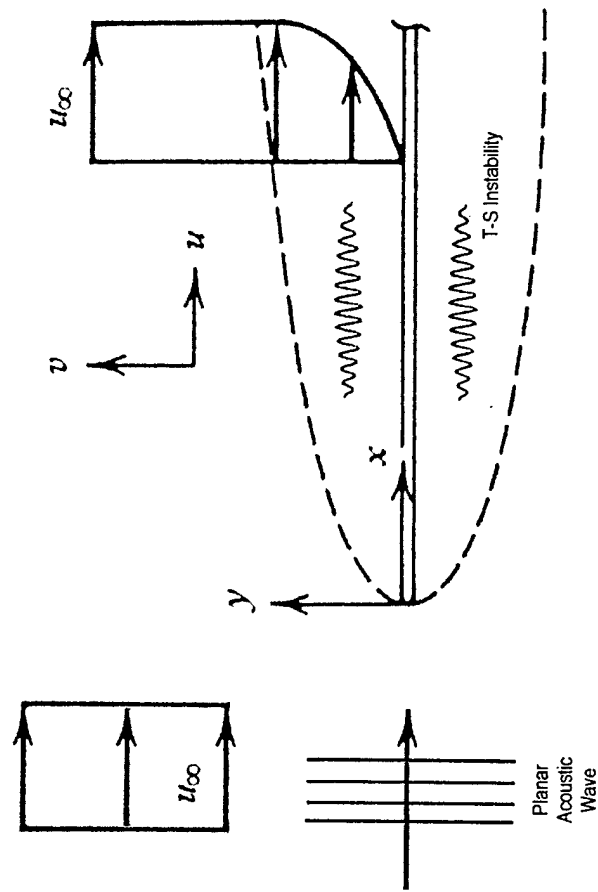
Figure 2. Diagram of receptivity.

a   turning vanes
b   honeycomb
c   screens
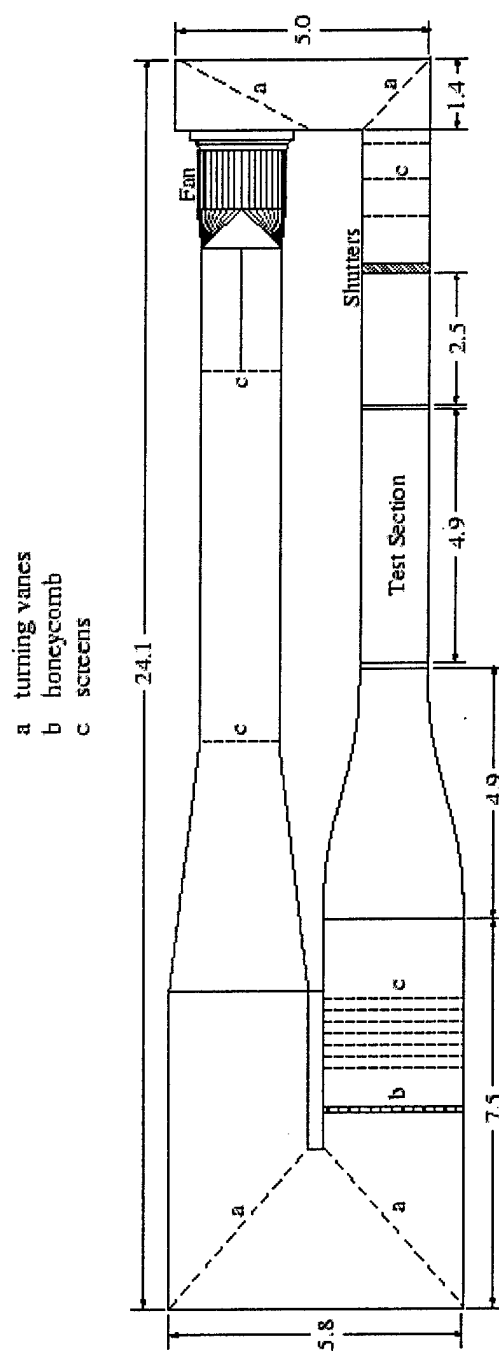
Figure 3. Overhead sketch of the Unsteady Wind Tunnel. All dimensions in meters.
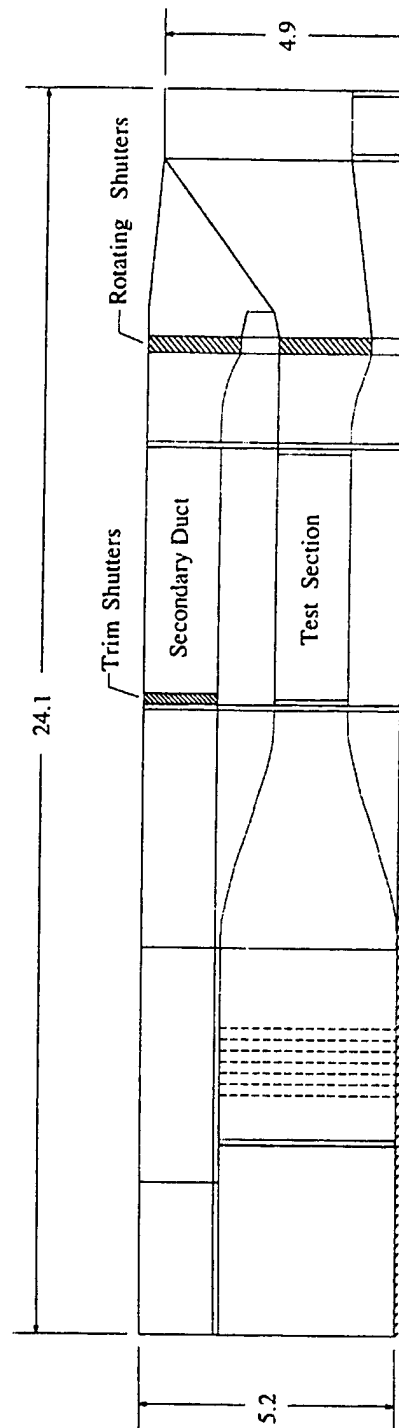
Figure 4. Front view of the Unsteady Wind Tunnel. All dimensions in meters.

58
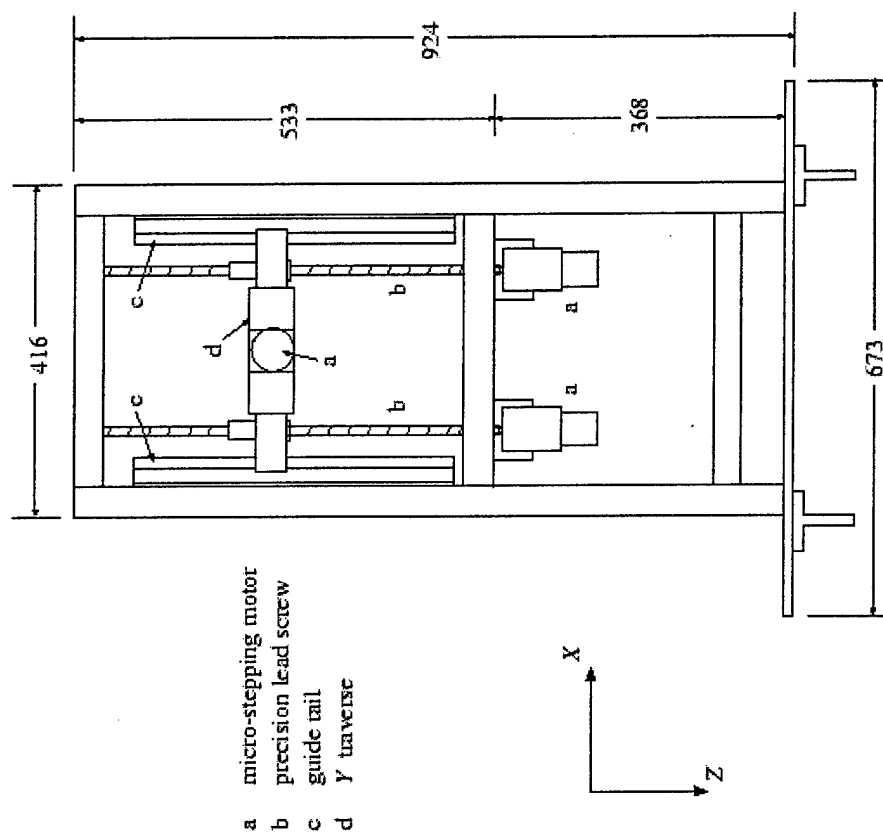
Figure 5. Front view of the traverse structure. All dimensions in millimeters.

a   micro-stepping motor
b   precision lead screw
c   guide rail
d   Y traverse

a micro-stepping motor
b lead screw
c guide rail
d Y traverse
e interior wall
f outer pressure wall
g 1/4" plexiglass
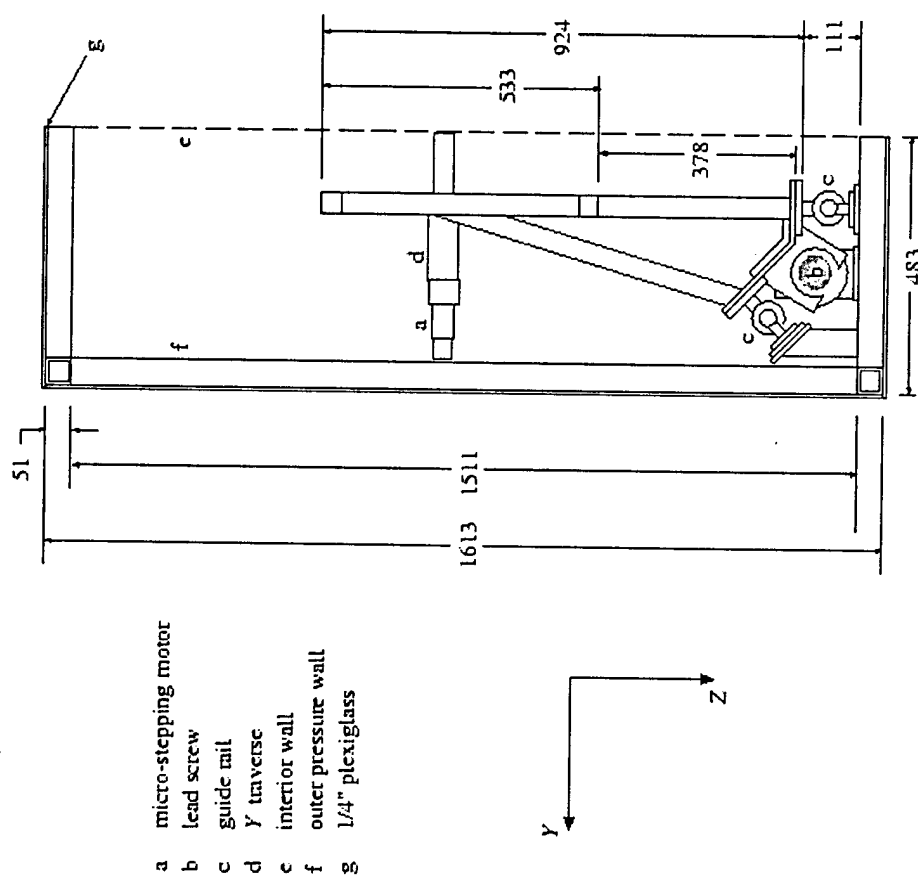
Figure 6. Side view of the traverse structure. All dimensions in millimeters.
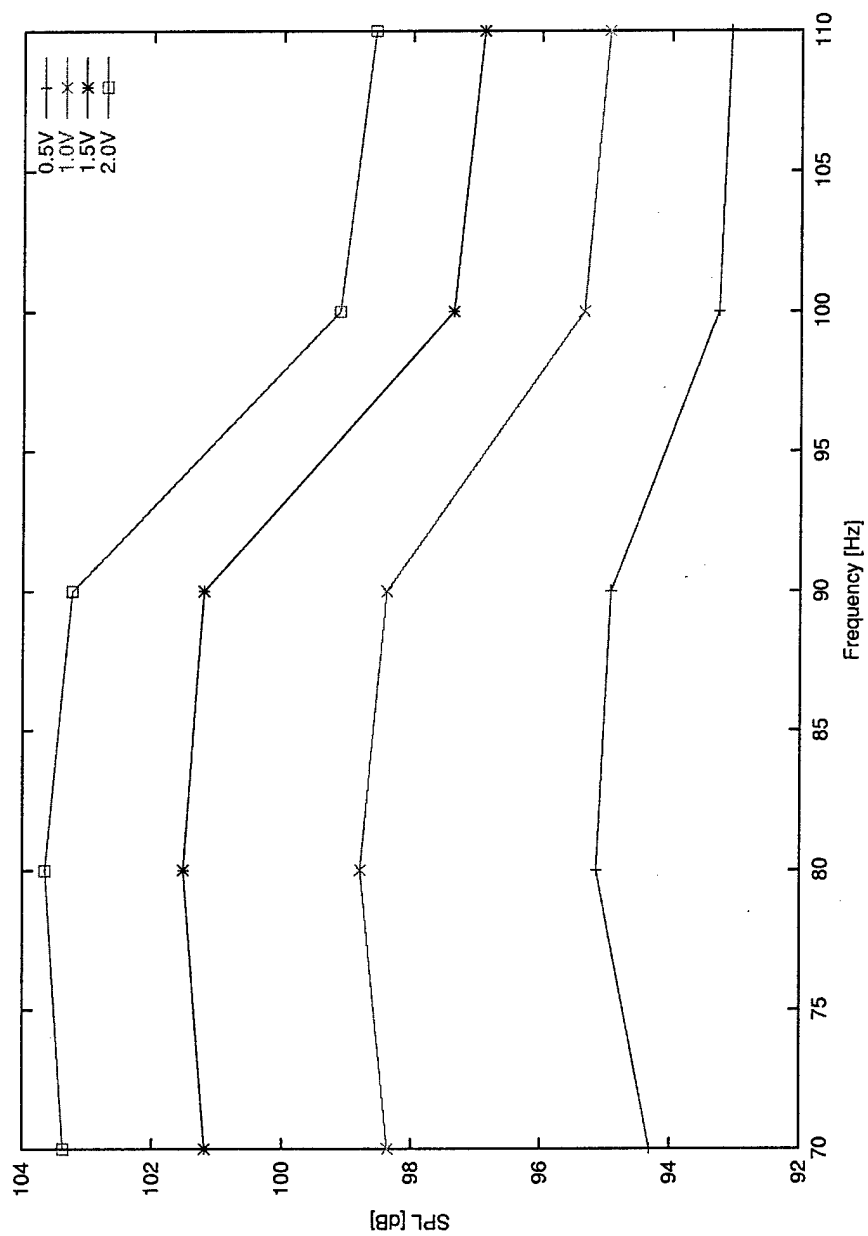
Figure 7. Speaker response. Sound pressure level versus frequency for $U = 12$ m/s
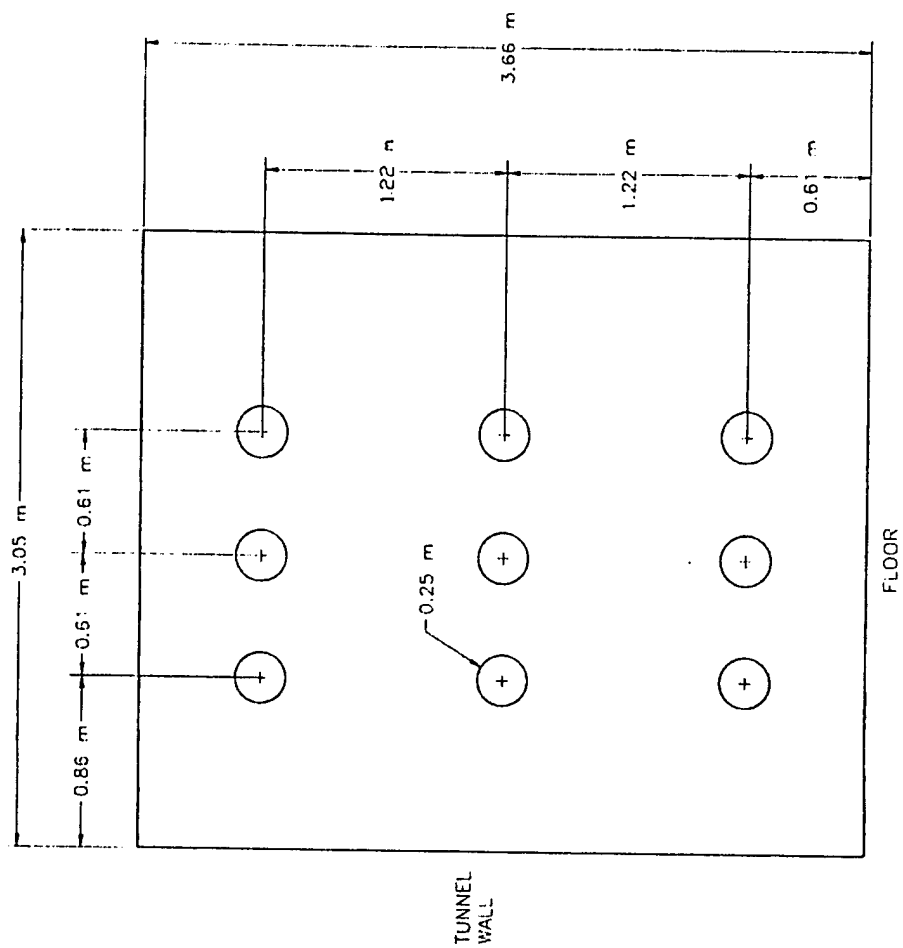
Figure 8. Speaker layout at the plenum wall.
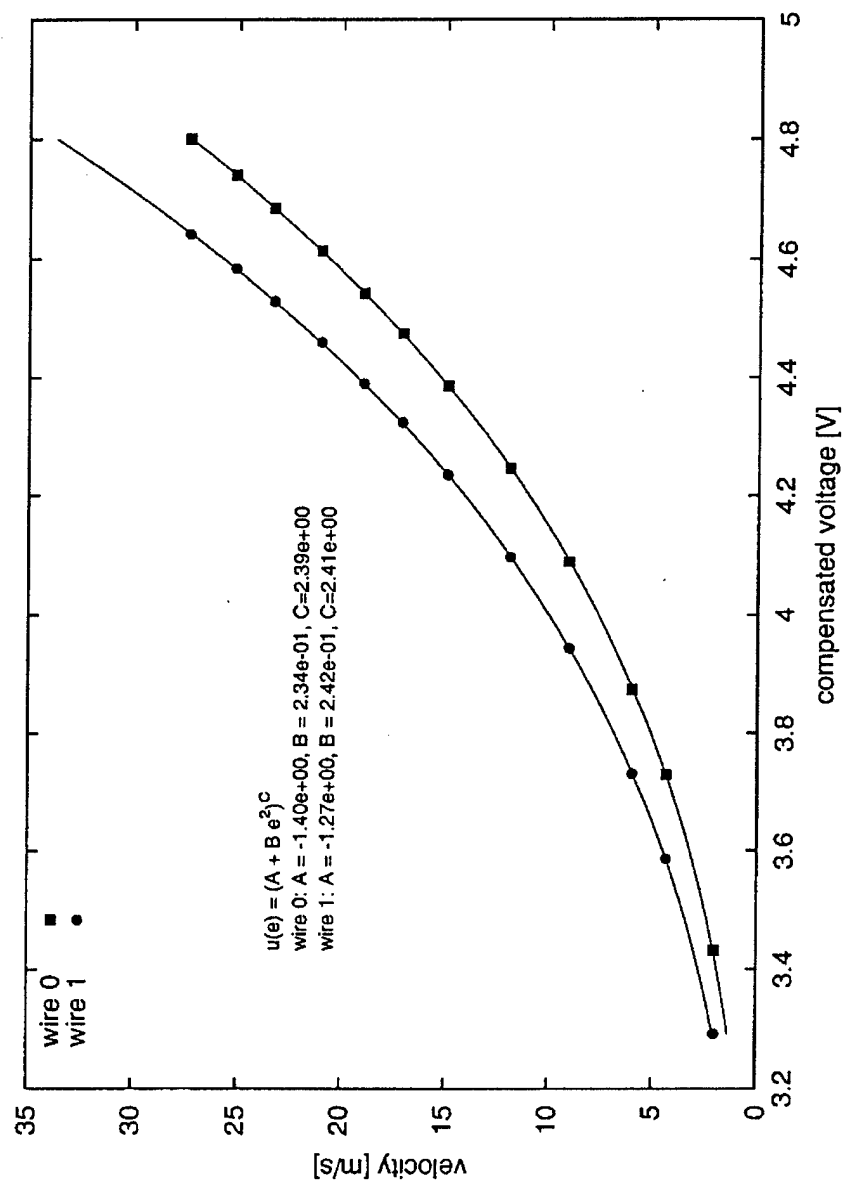
Figure 9. Typical hotwire calibration curve.
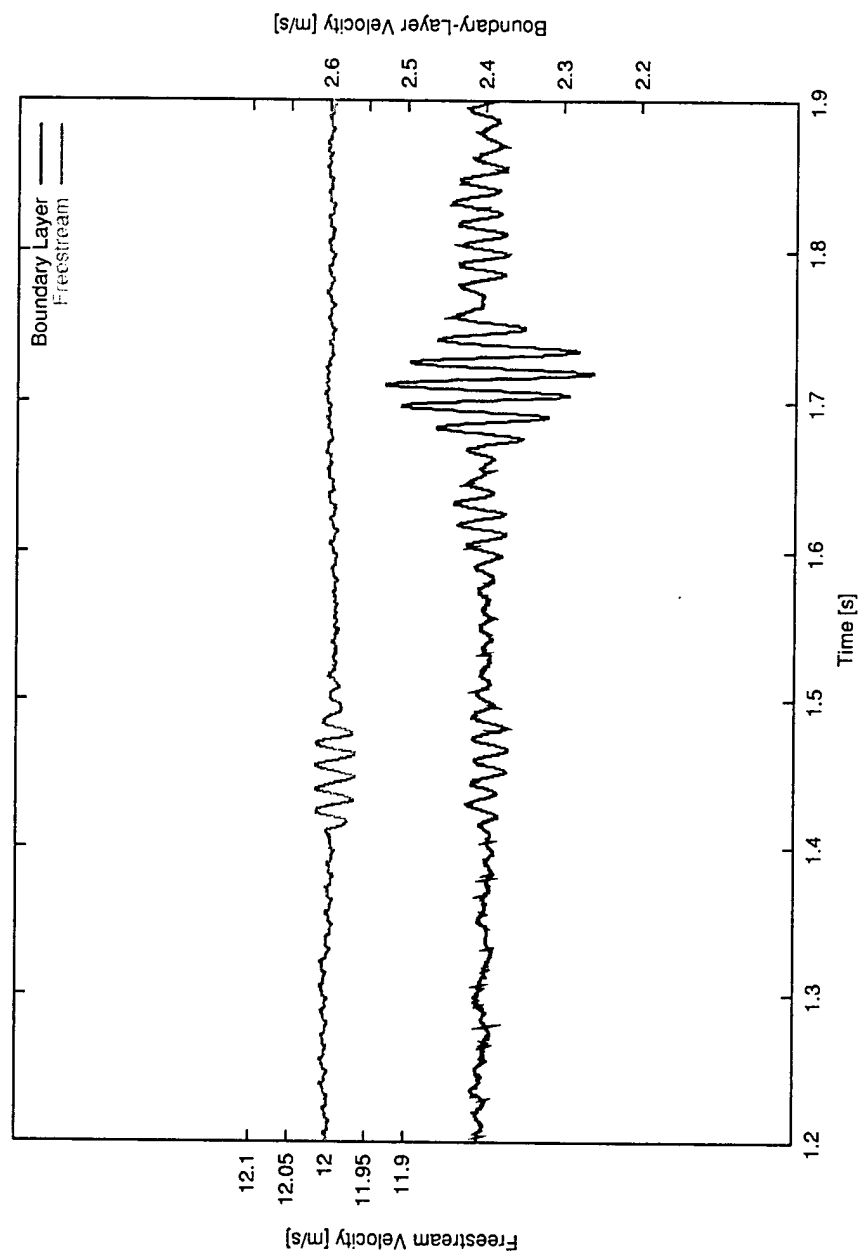
Figure 10. Hotwire velocity measurements, $U_\infty = 12$ m/s, 5-cycle, 67.4 Hz pulse, SPL = 107dB.
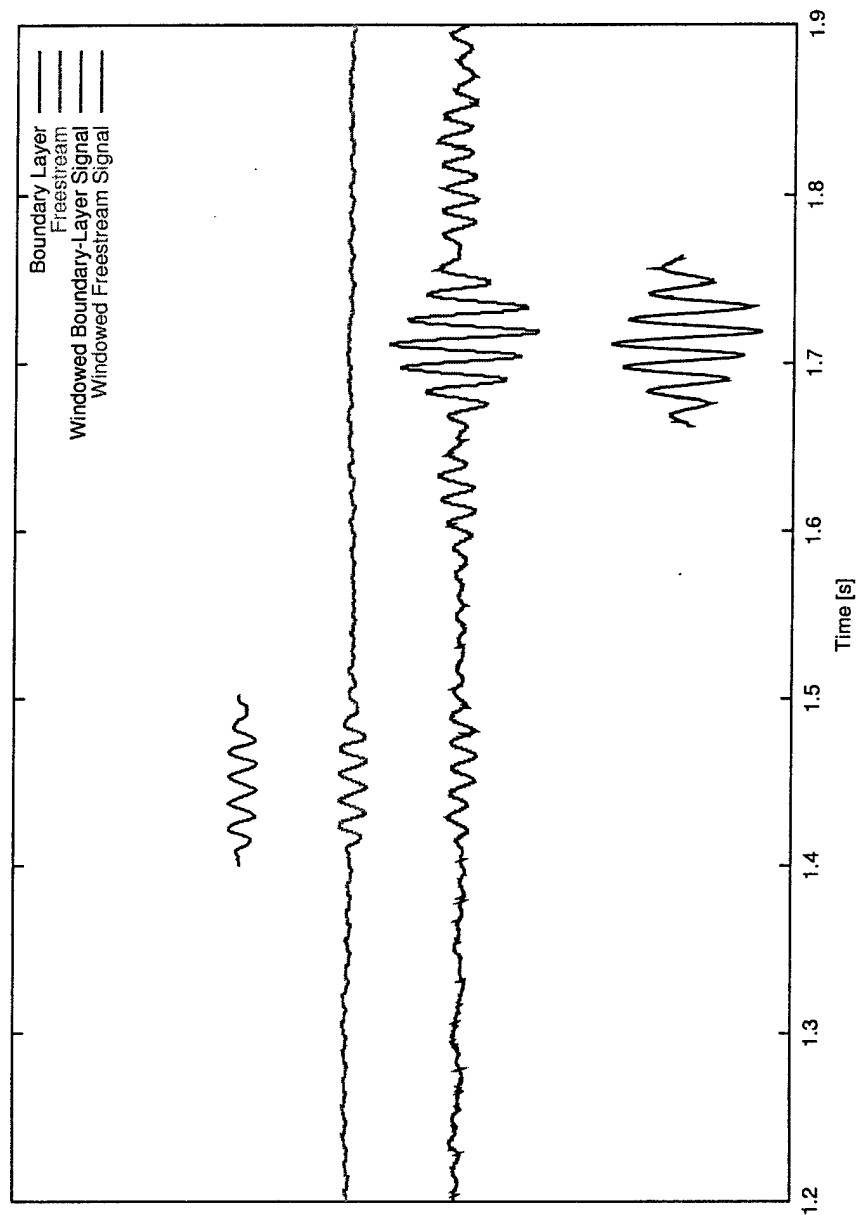
Figure 11. Hotwire velocity measurements. Comparison with windowed data.
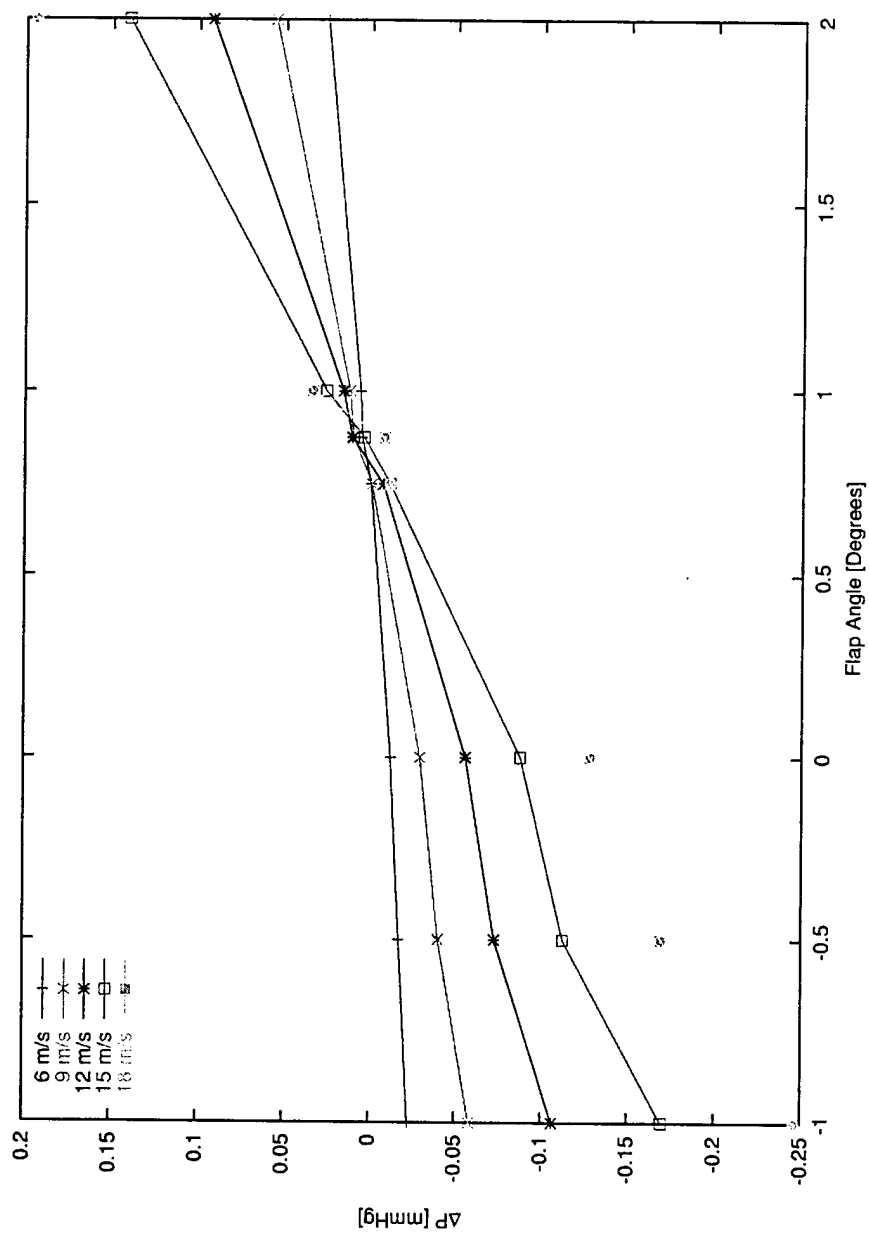
Figure 12. Symmetric-flow measurements using the top leading-edge static pressure ports
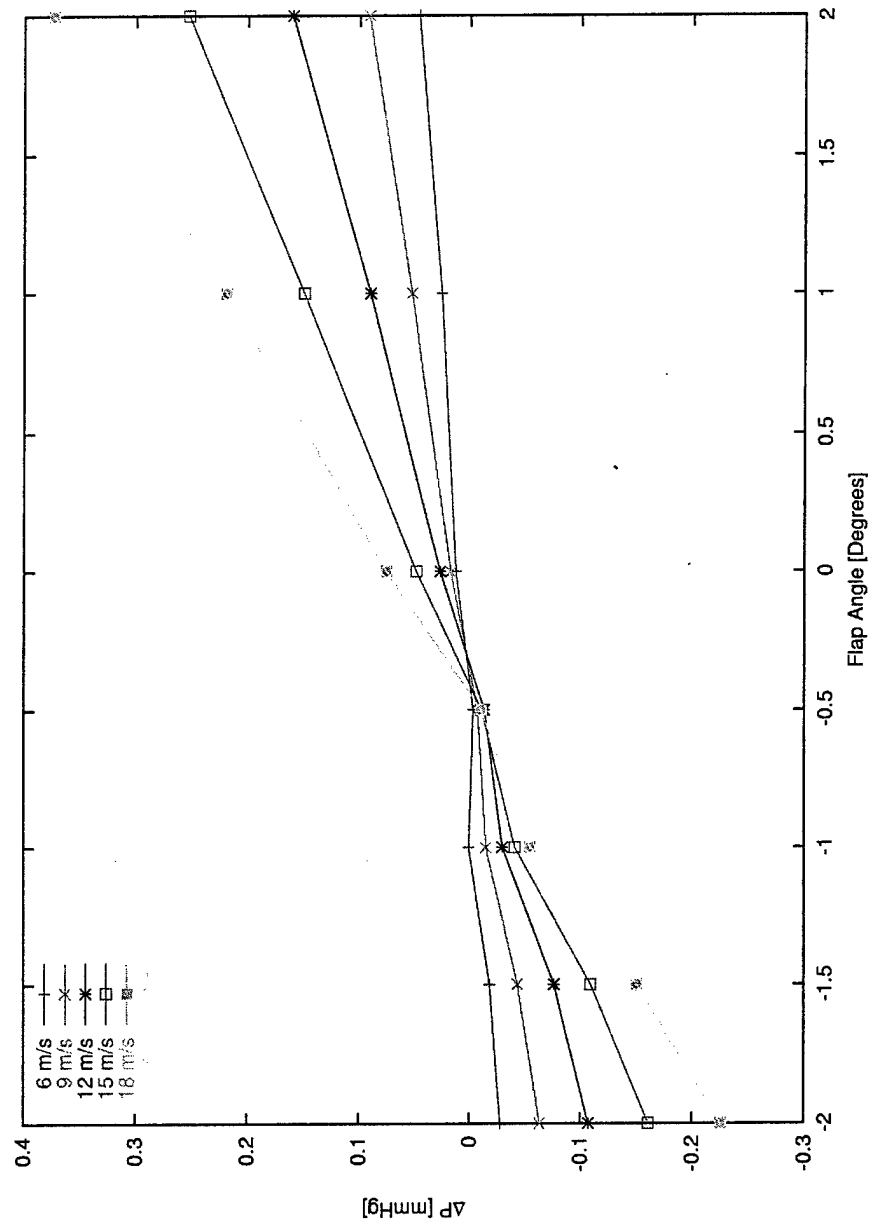
Figure 13. Symmetric-flow measurements using the bottom
leading-edge static pressure ports
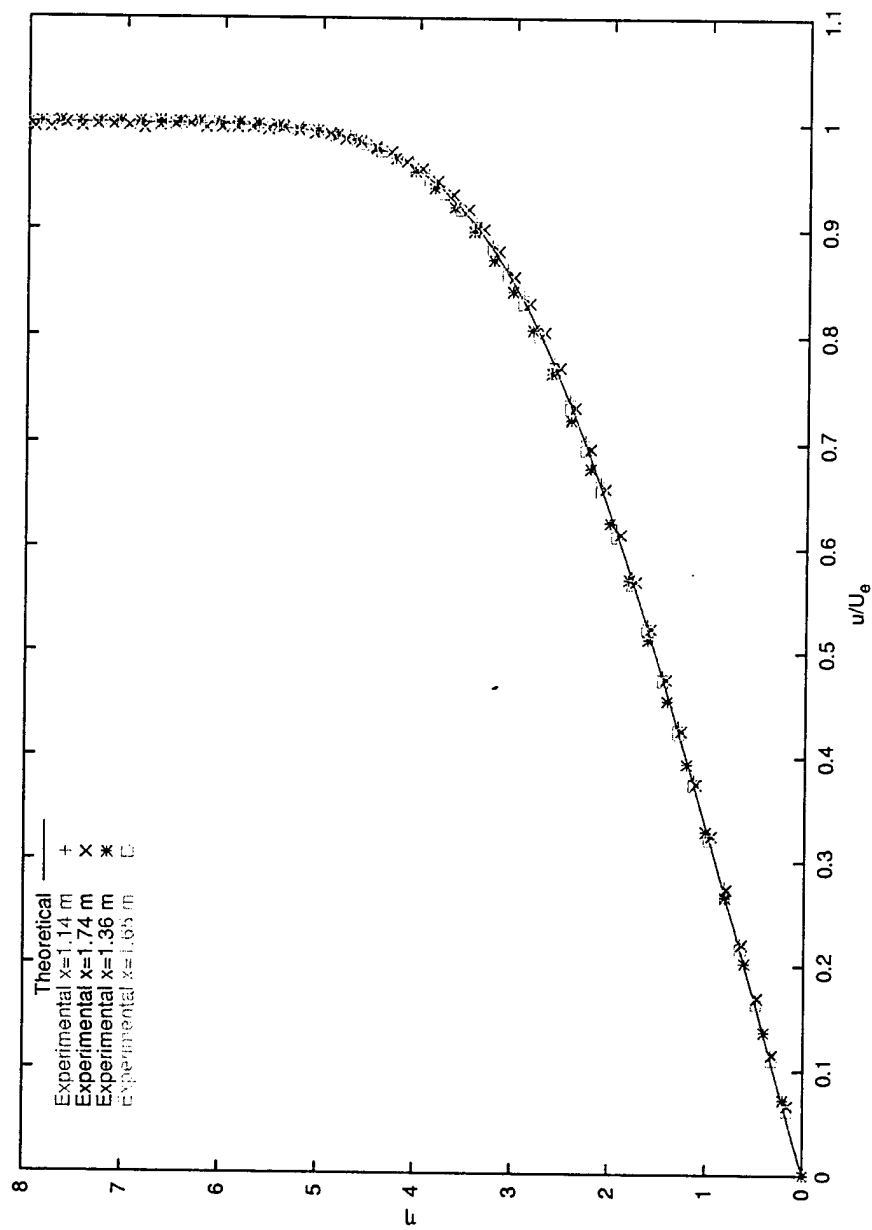
Figure 14. Mean velocity profile comparison.
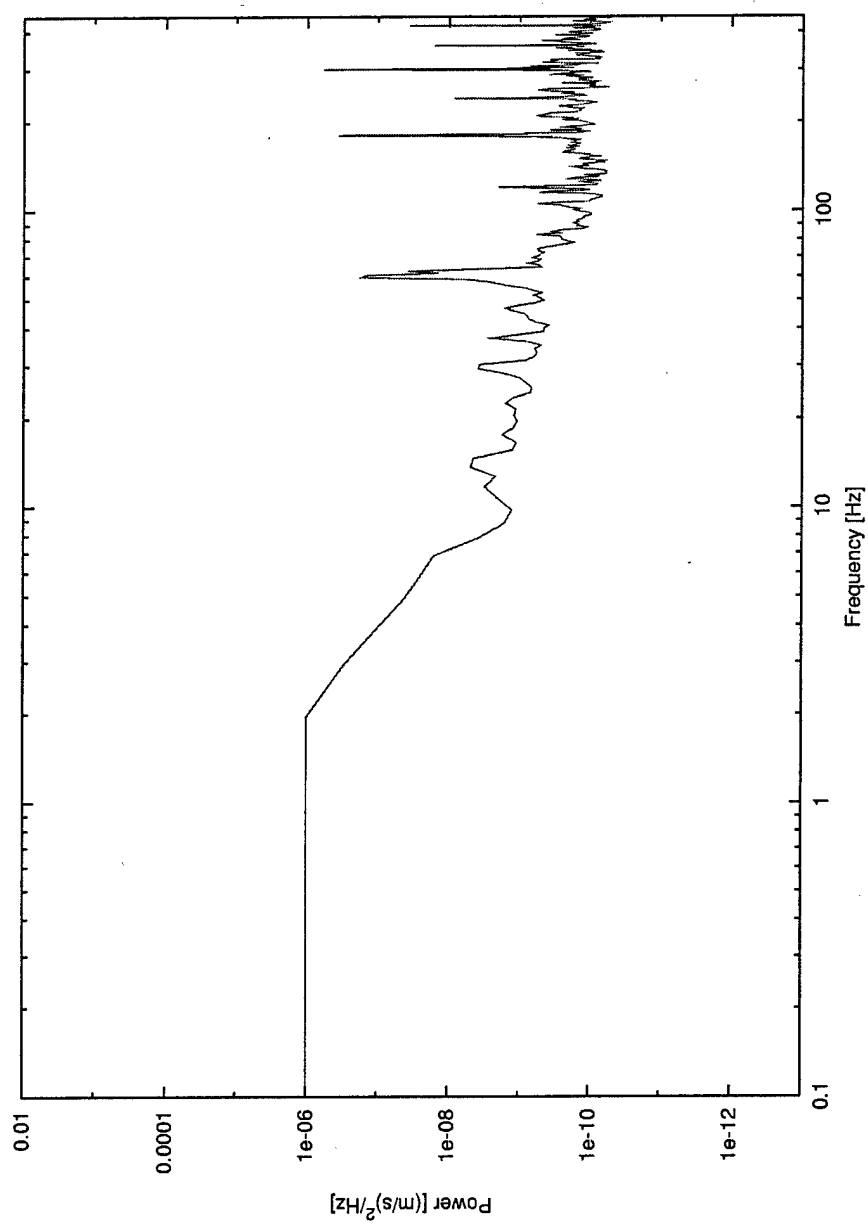
Figure 15. Freestream turbulence spectrum at $U_\infty = 8$ m/s, 1 - 450 Hz bandpass.
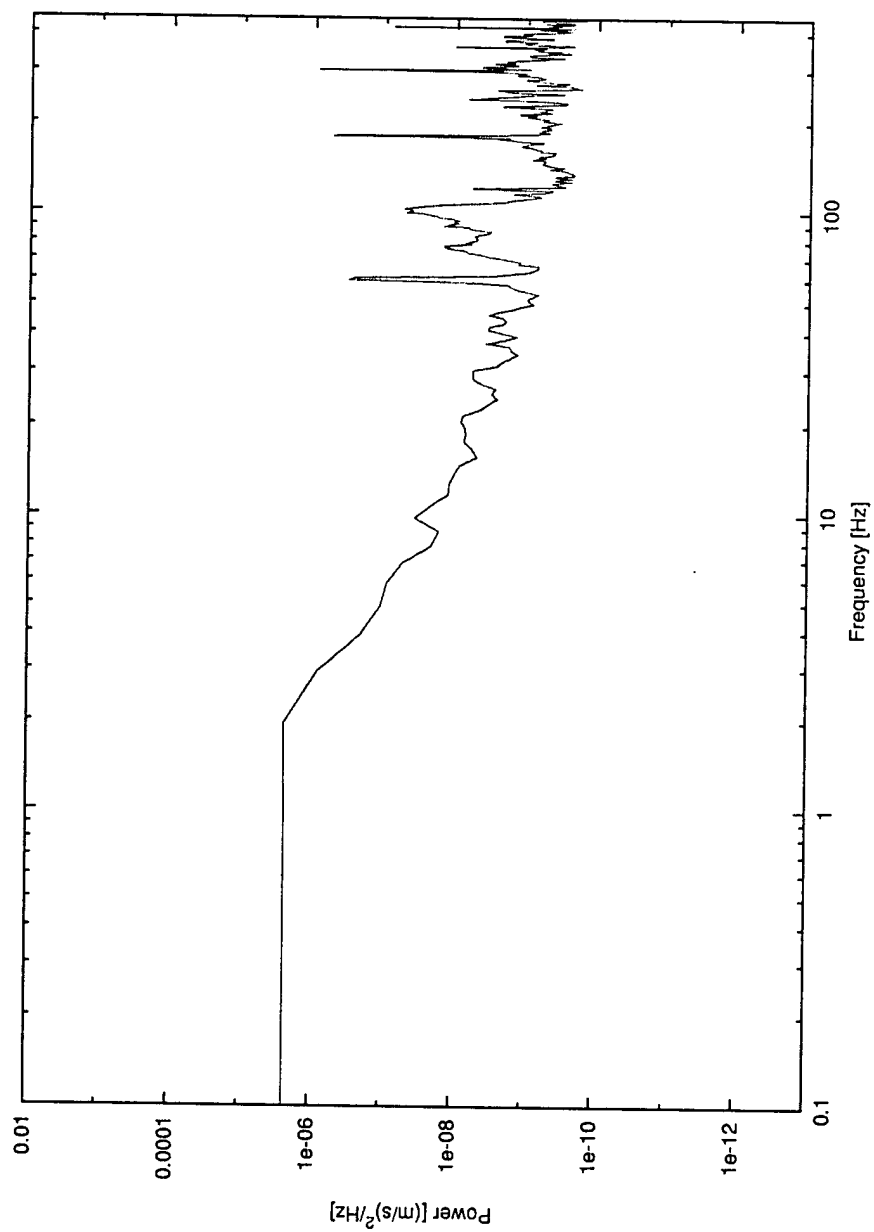
Figure 16. Freestream turbulence spectrum at $U_\infty = 12$ m/s, 1 - 450 Hz bandpass.
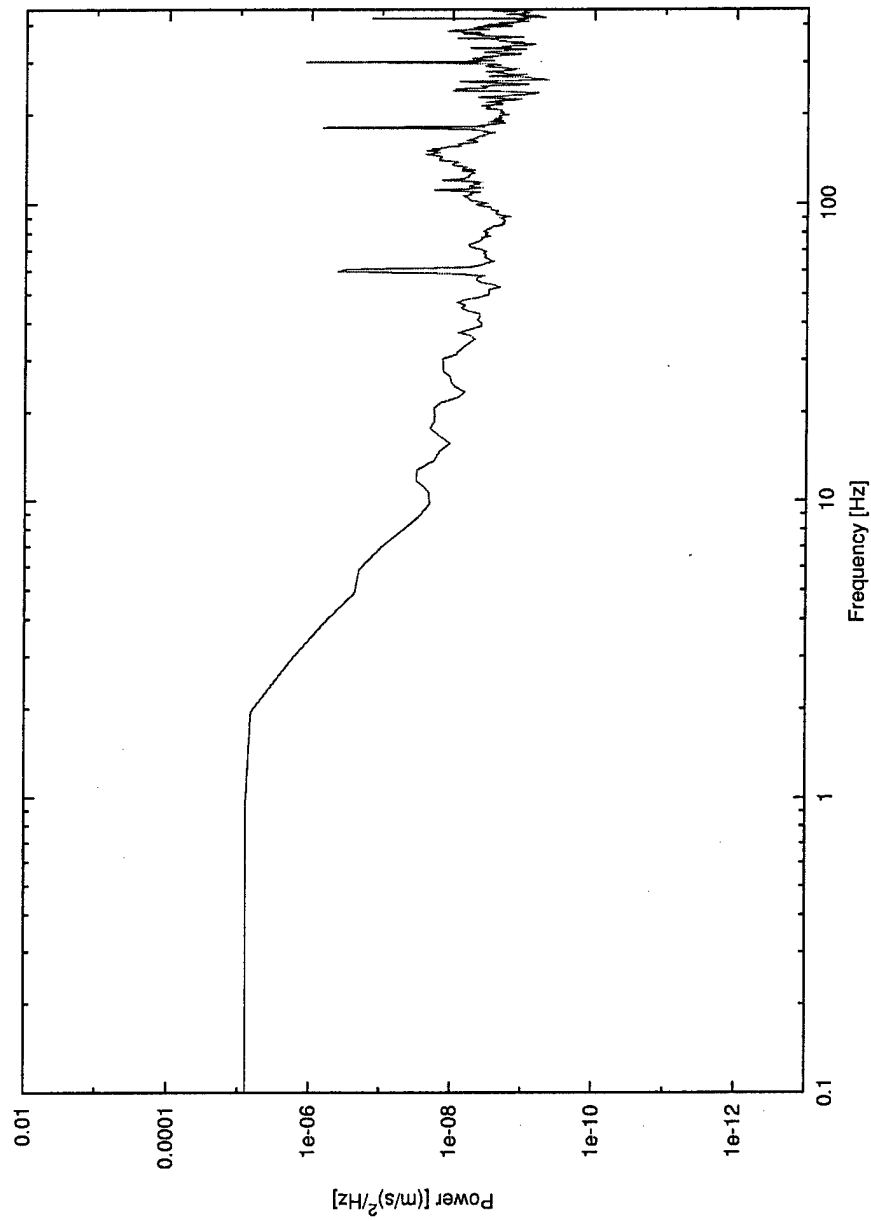
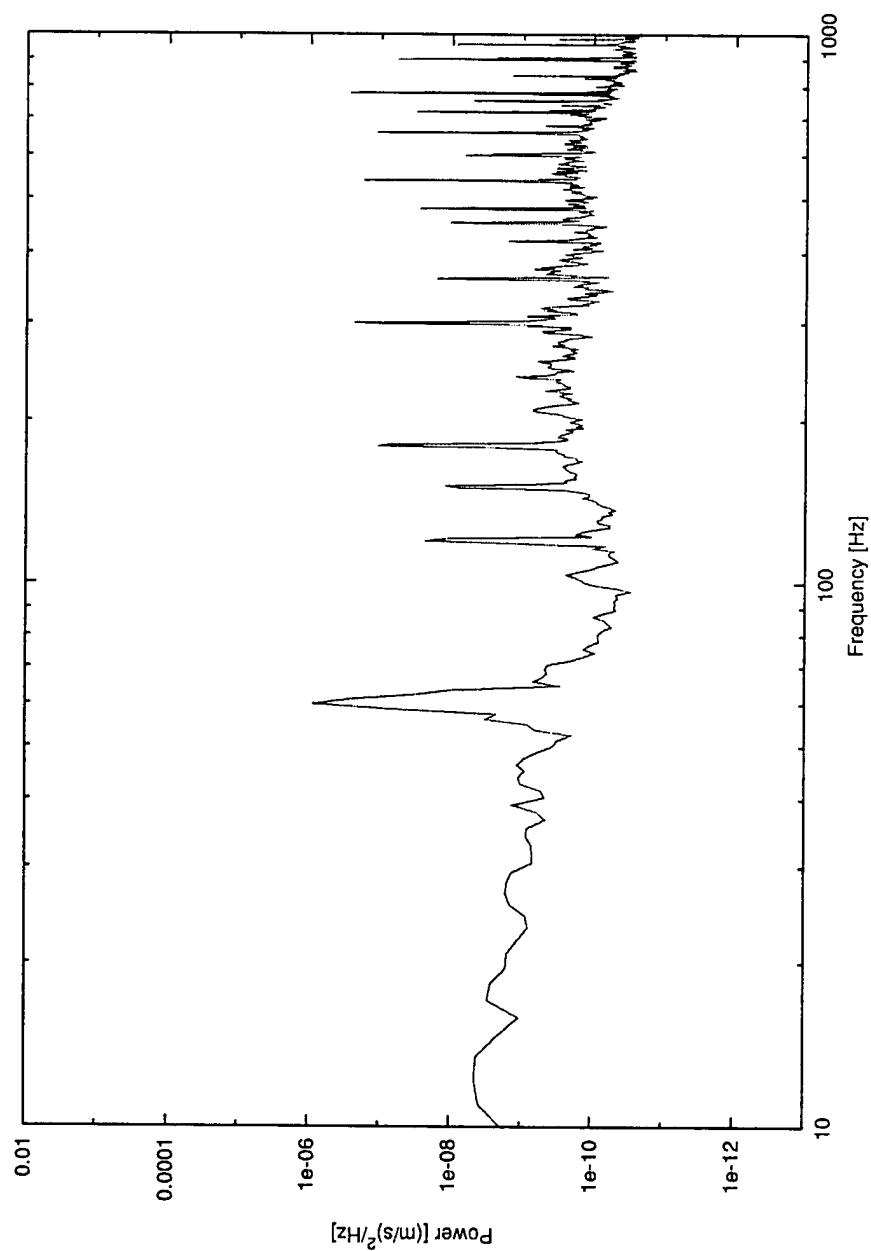Figure 17. Freestream turbulence spectrum at $U_\infty = 15$ m/s., 1 - 450 Hz bandpass.
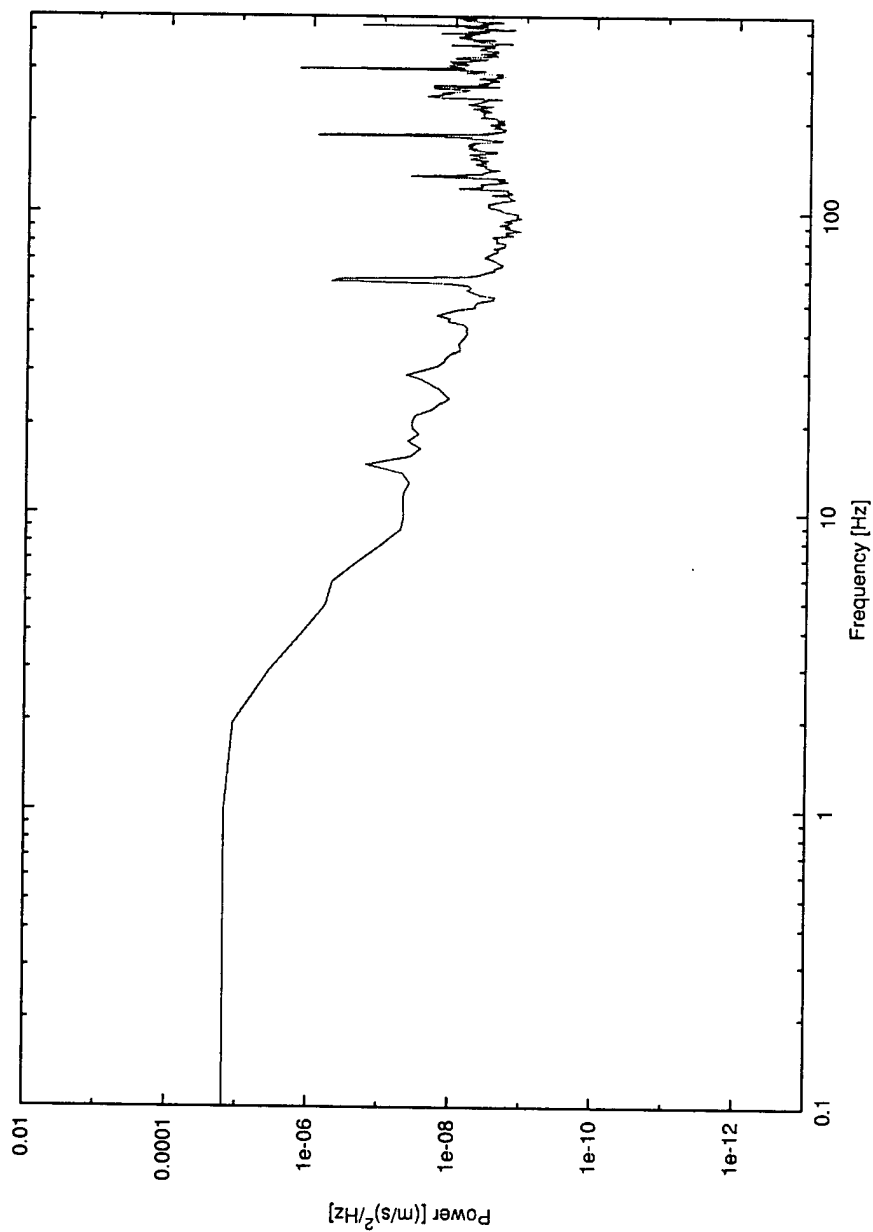
Figure 18. Freestream turbulence spectrum at $U_\infty = 18$ m/s, 1 - 450 Hz bandpass.
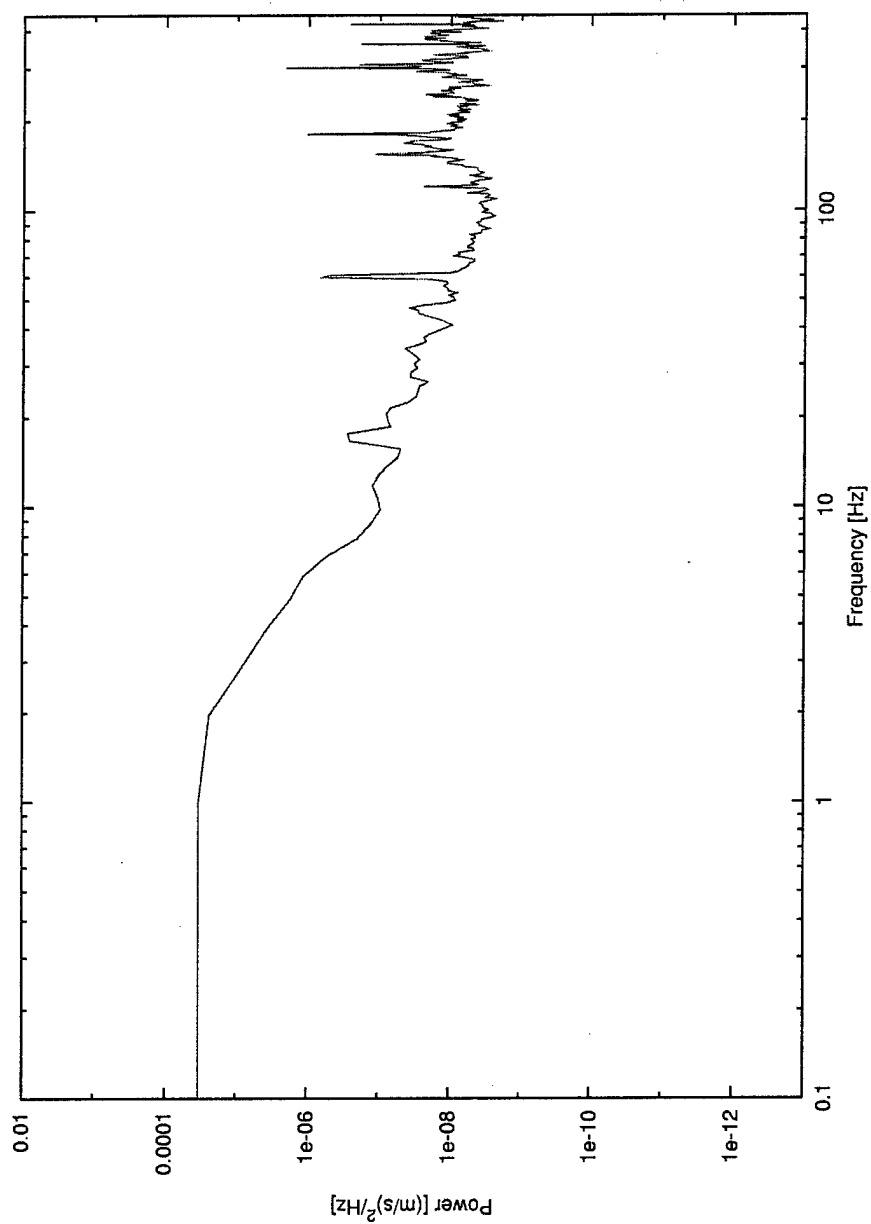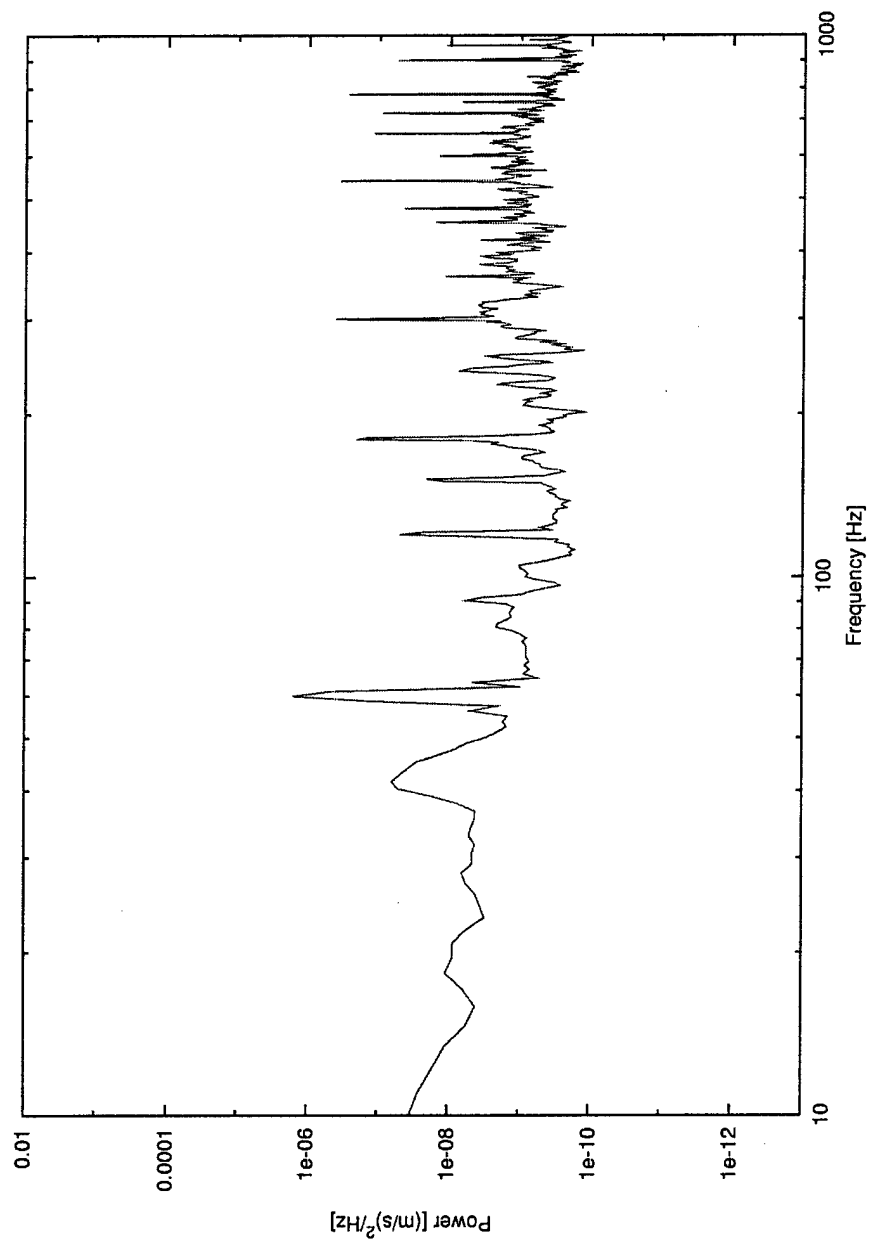
Figure 19. Freestream turbulence spectrum at $U_\infty = 21$ m/s, 1 - 450 Hz bandpass.
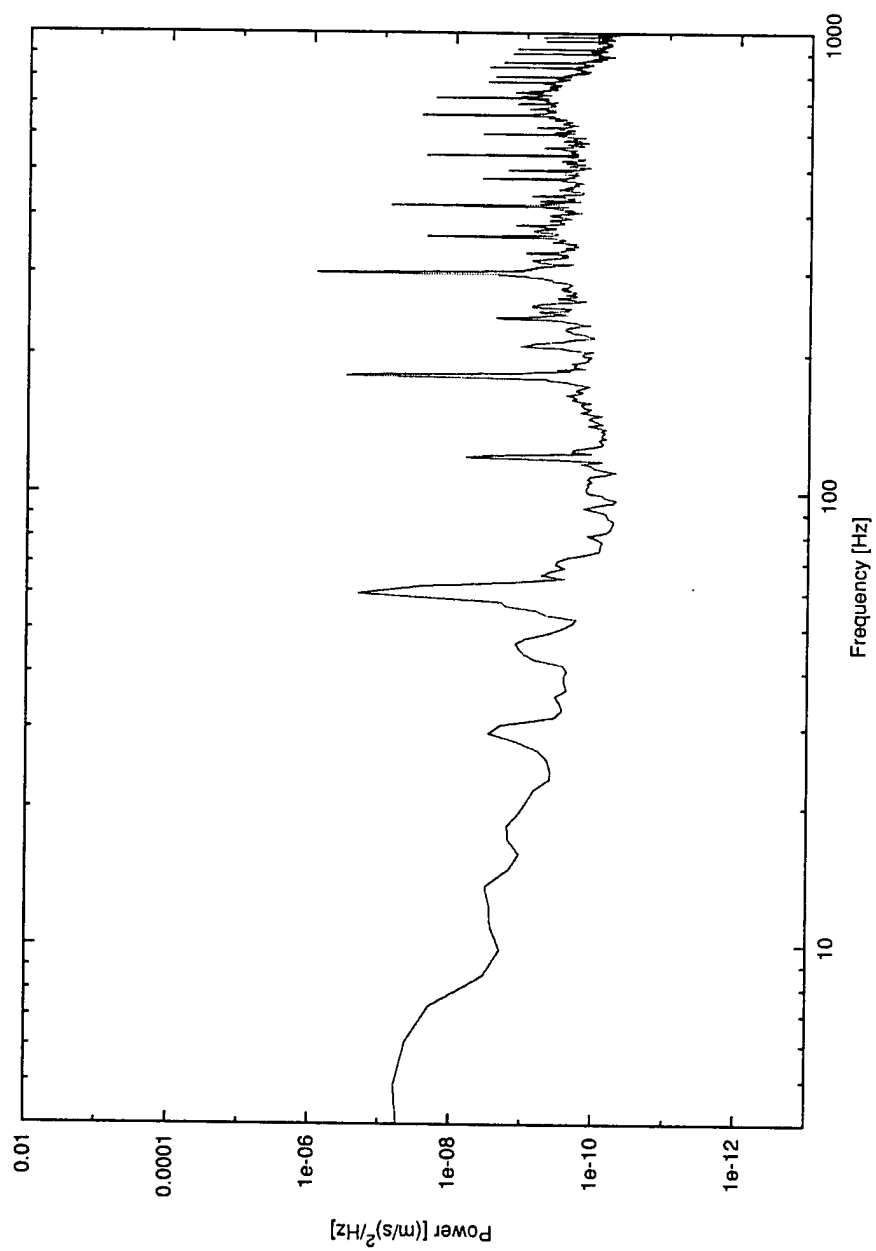
Figure 20. Freestream turbulence spectrum at $U_\infty = 8$ m/s, 4 - 1000 Hz bandpass.
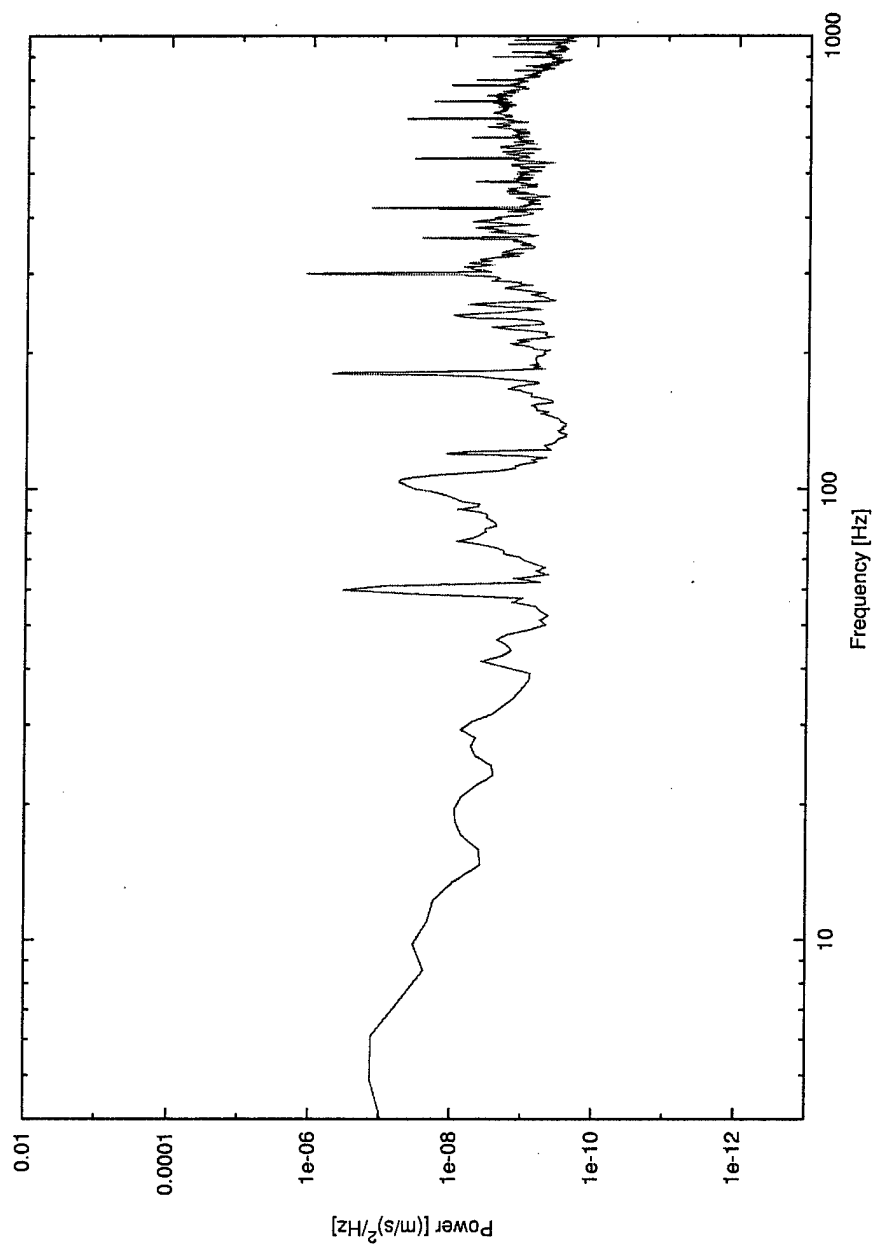
Figure 21. Freestream turbulence spectrum at $U_\infty = 12$ m/s, 4 - 1000 Hz bandpass.
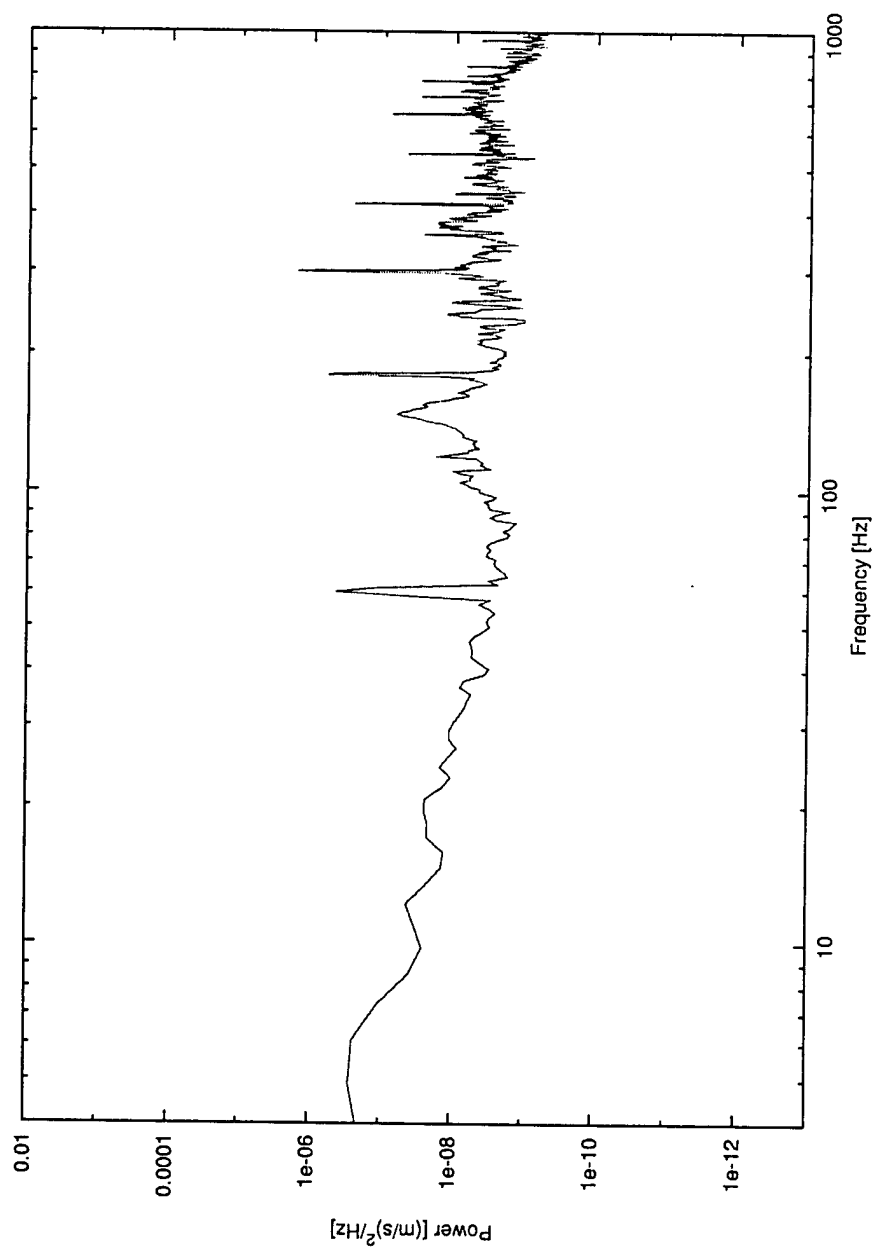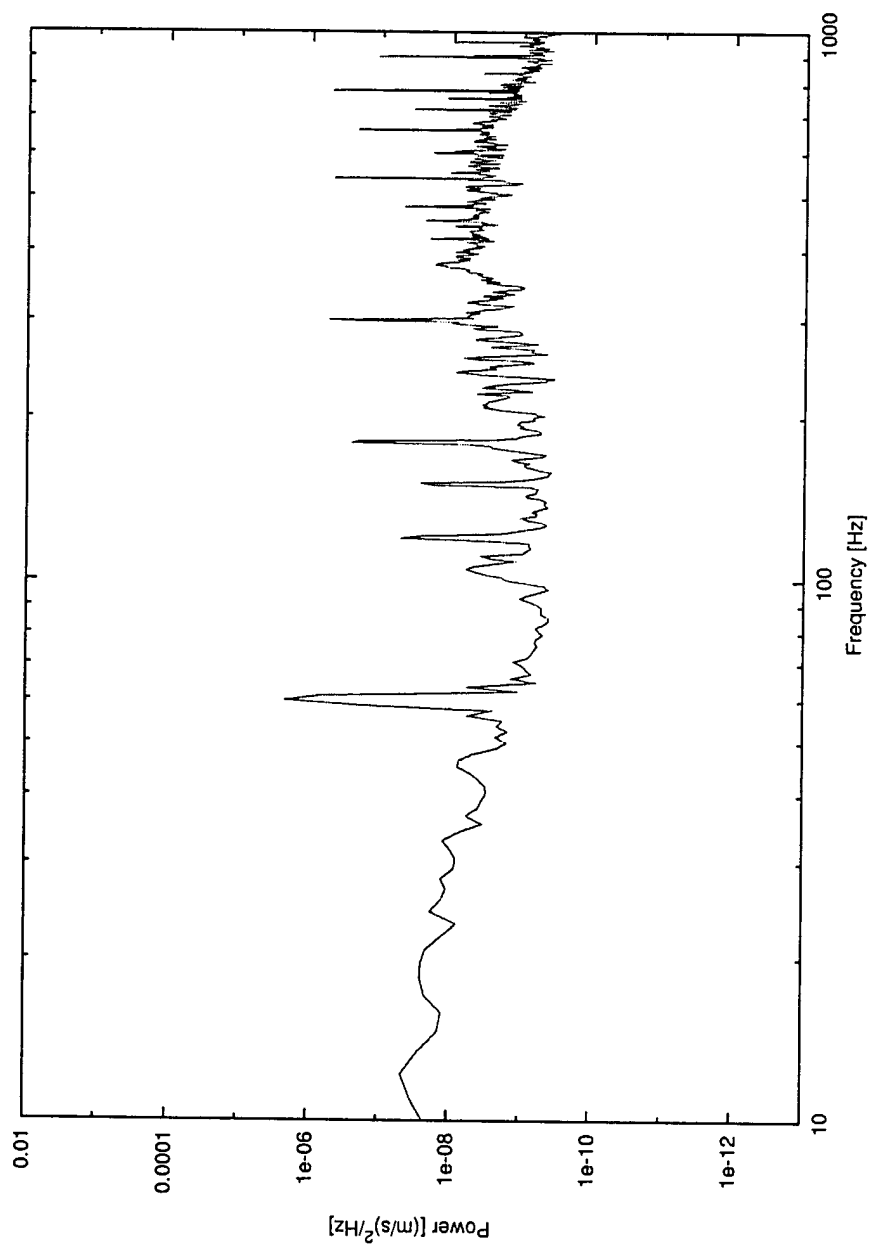
Figure 22. Freestream turbulence spectrum at $U_\infty = 15$ m/s, 4 - 1000 Hz bandpass.
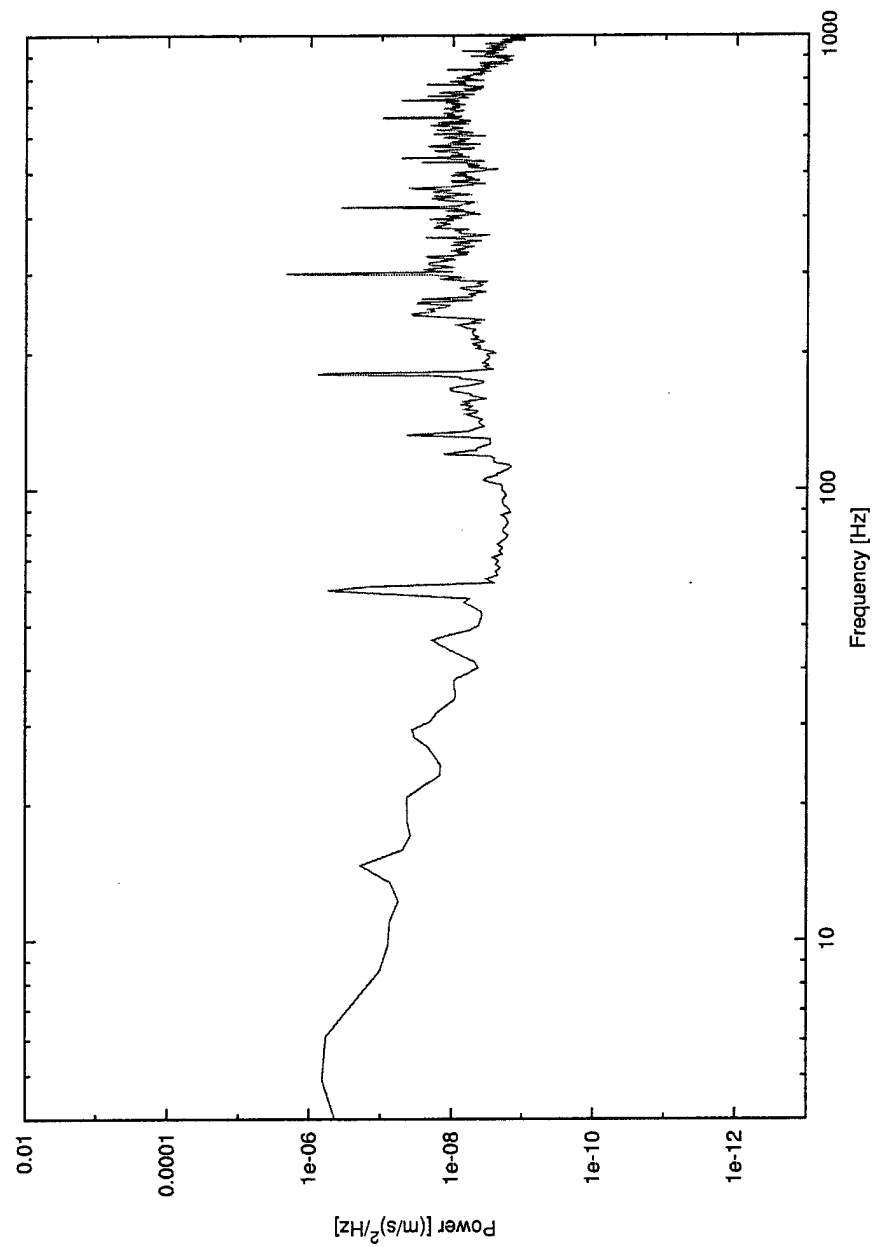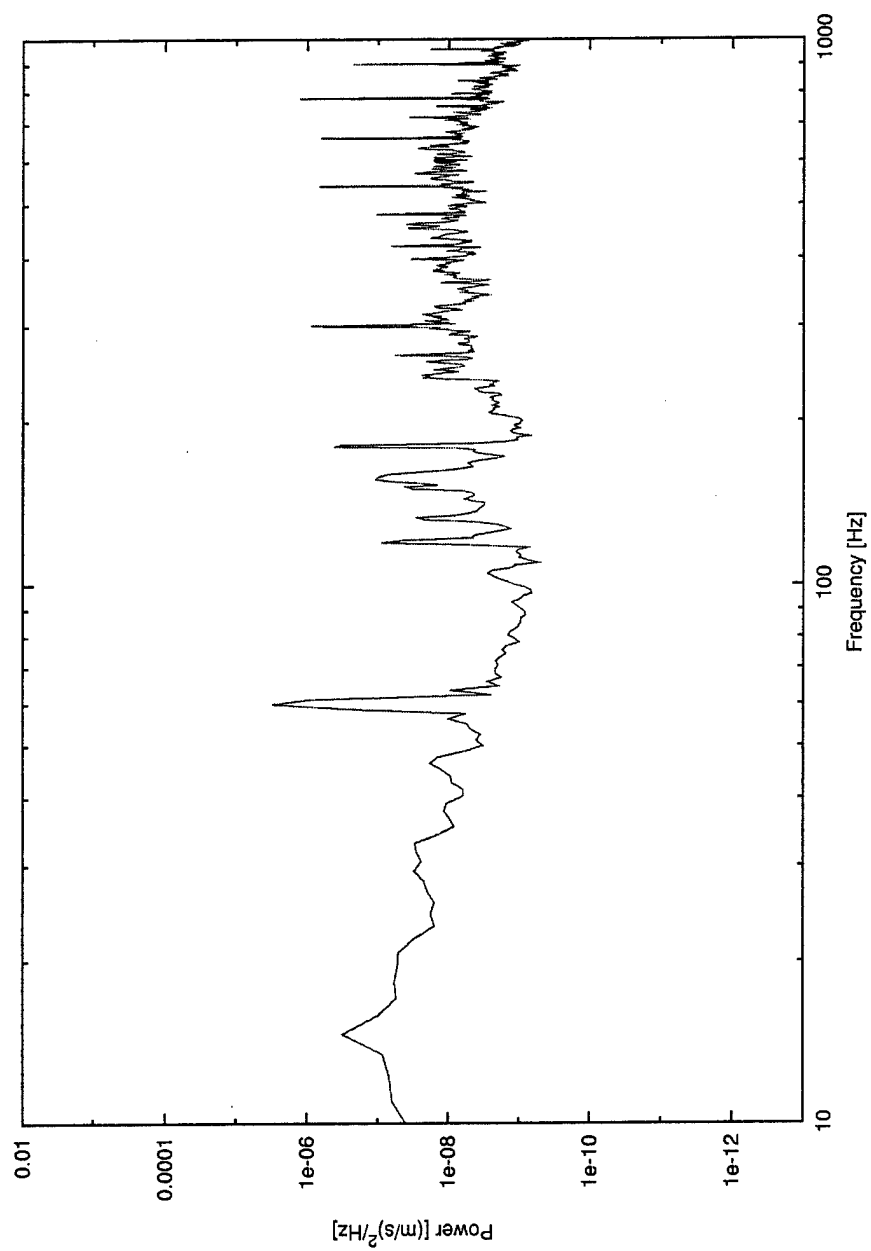
Figure 23. Freestream turbulence spectrum at $U_\infty = 18$ m/s, 4 - 1000 Hz bandpass.
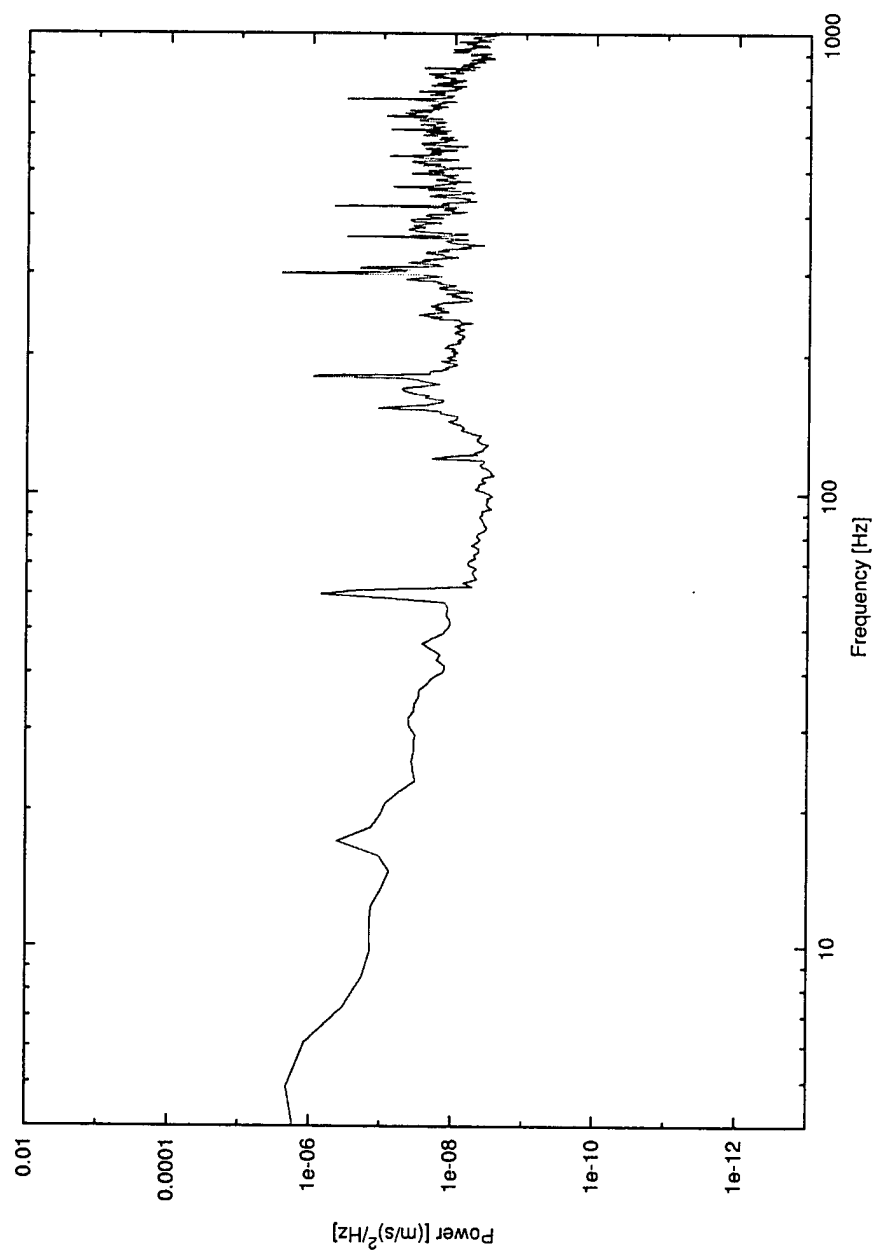
Figure 24. Freestream turbulence spectrum at U_∞ = 21 m/s,
4 - 1000 Hz bandpass.
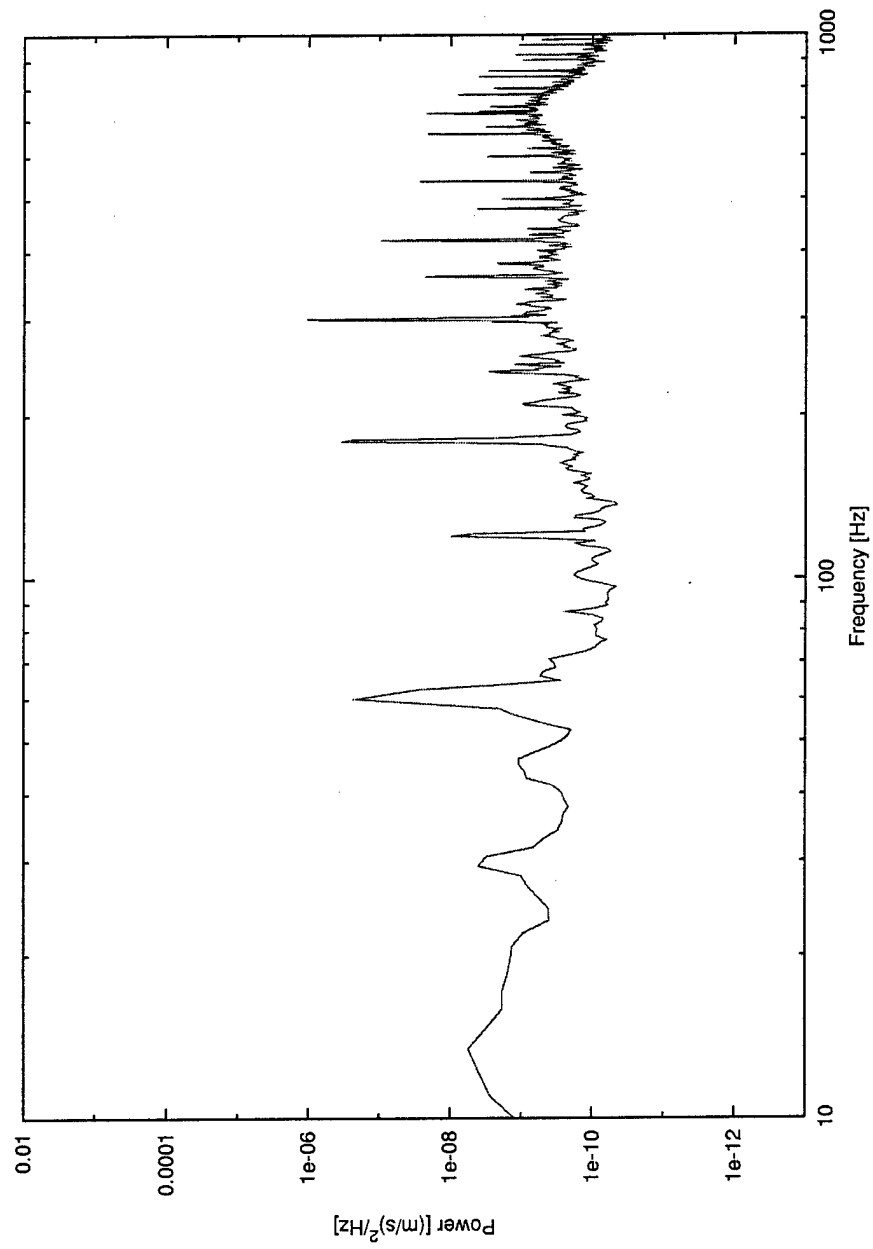
Figure 25. Freestream turbulence spectrum at $U_\infty = 8$ m/s.
10 - 1000 Hz bandpass.
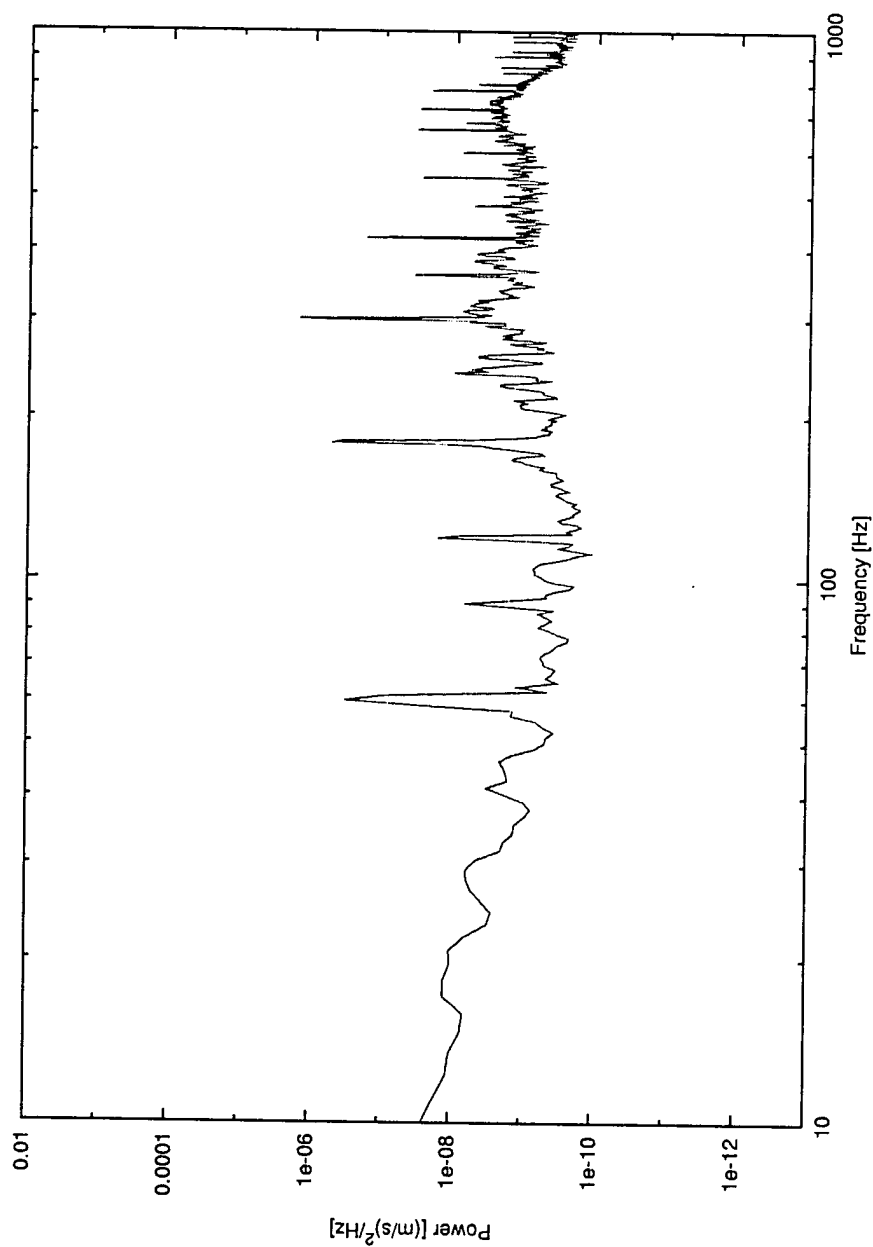
Figure 26. Freestream turbulence spectrum at $U_\infty = 12$ m/s, 10 - 1000 Hz bandpass.
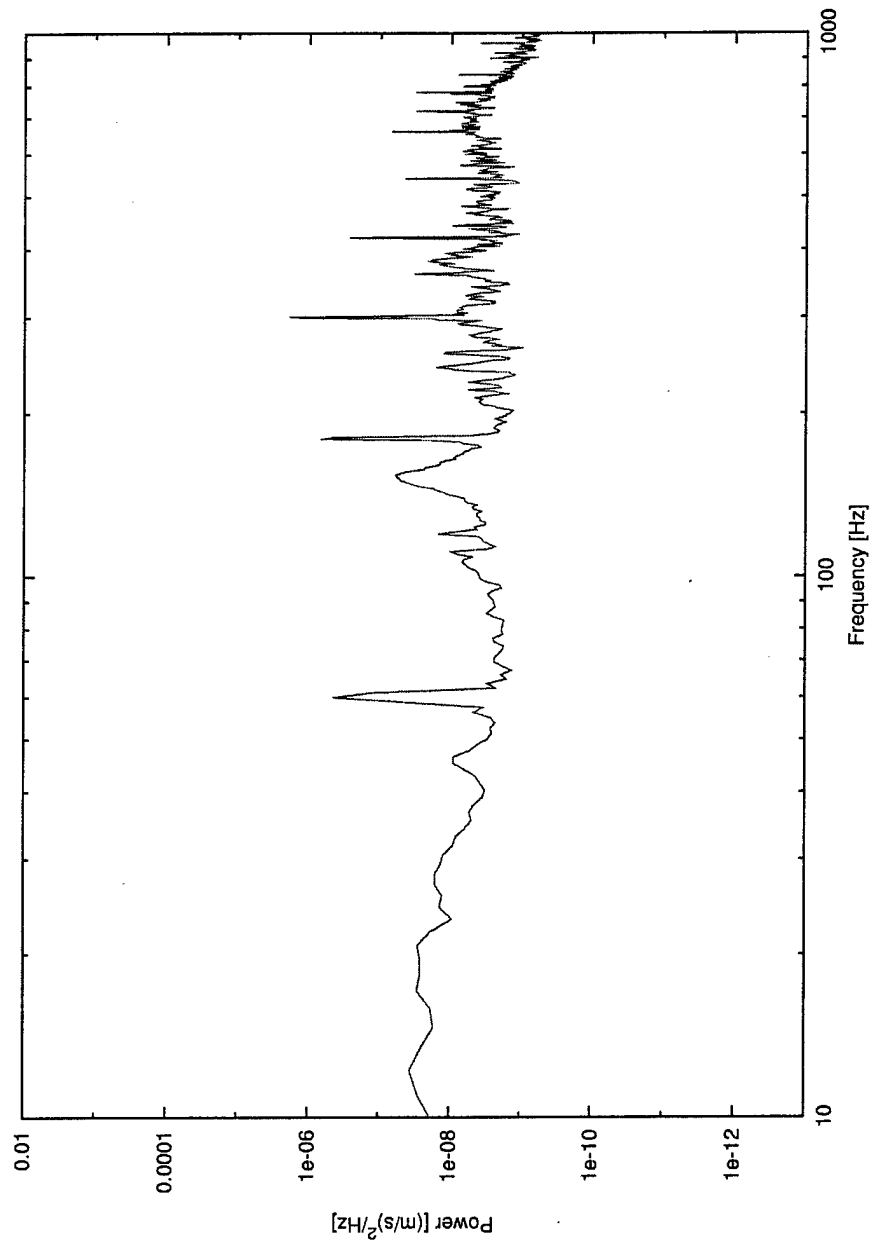
Figure 27. Freestream turbulence spectrum at $U_\infty = 15$ m/s., 10 - 1000 Hz bandpass.
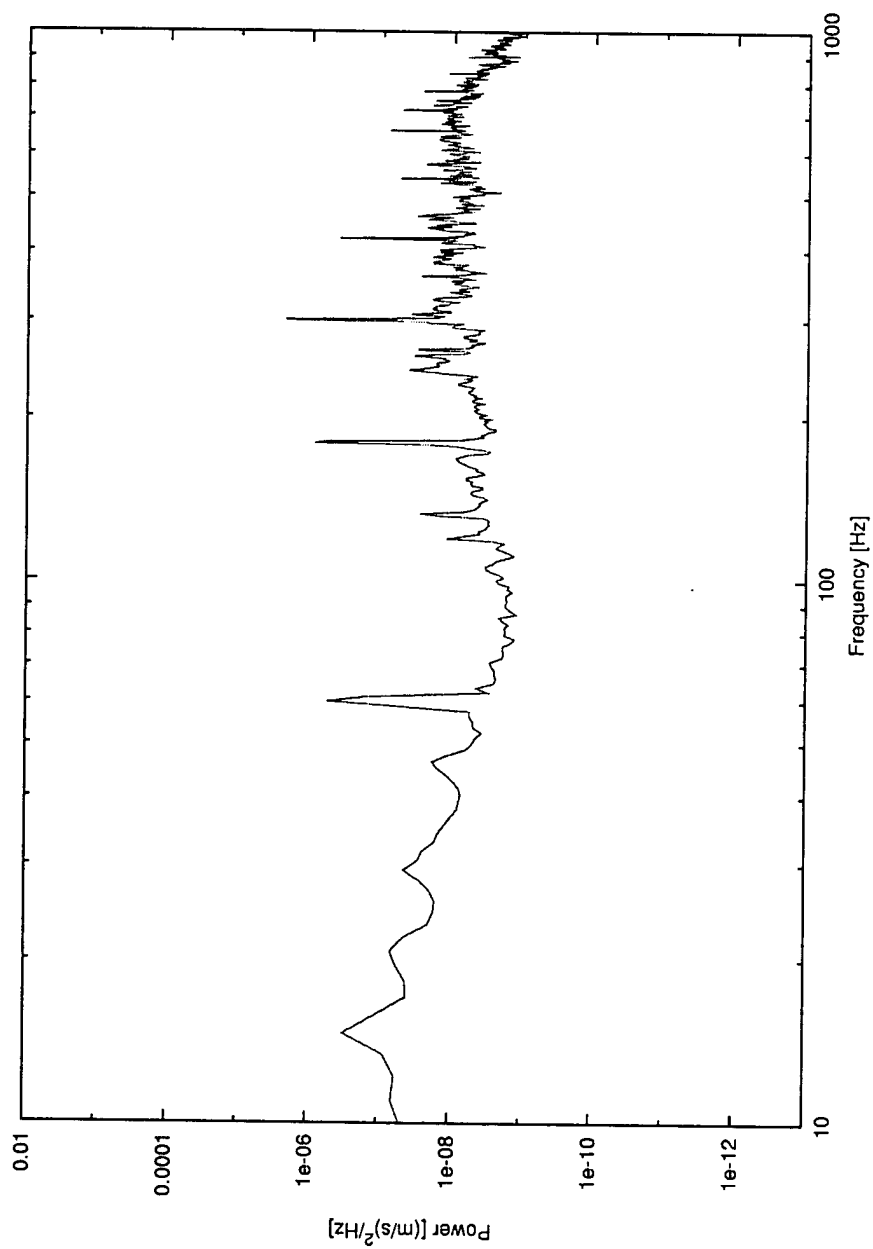
Figure 28. Freestream turbulence spectrum at $U_\infty = 18$ m/s, 10 - 1000 Hz bandpass.
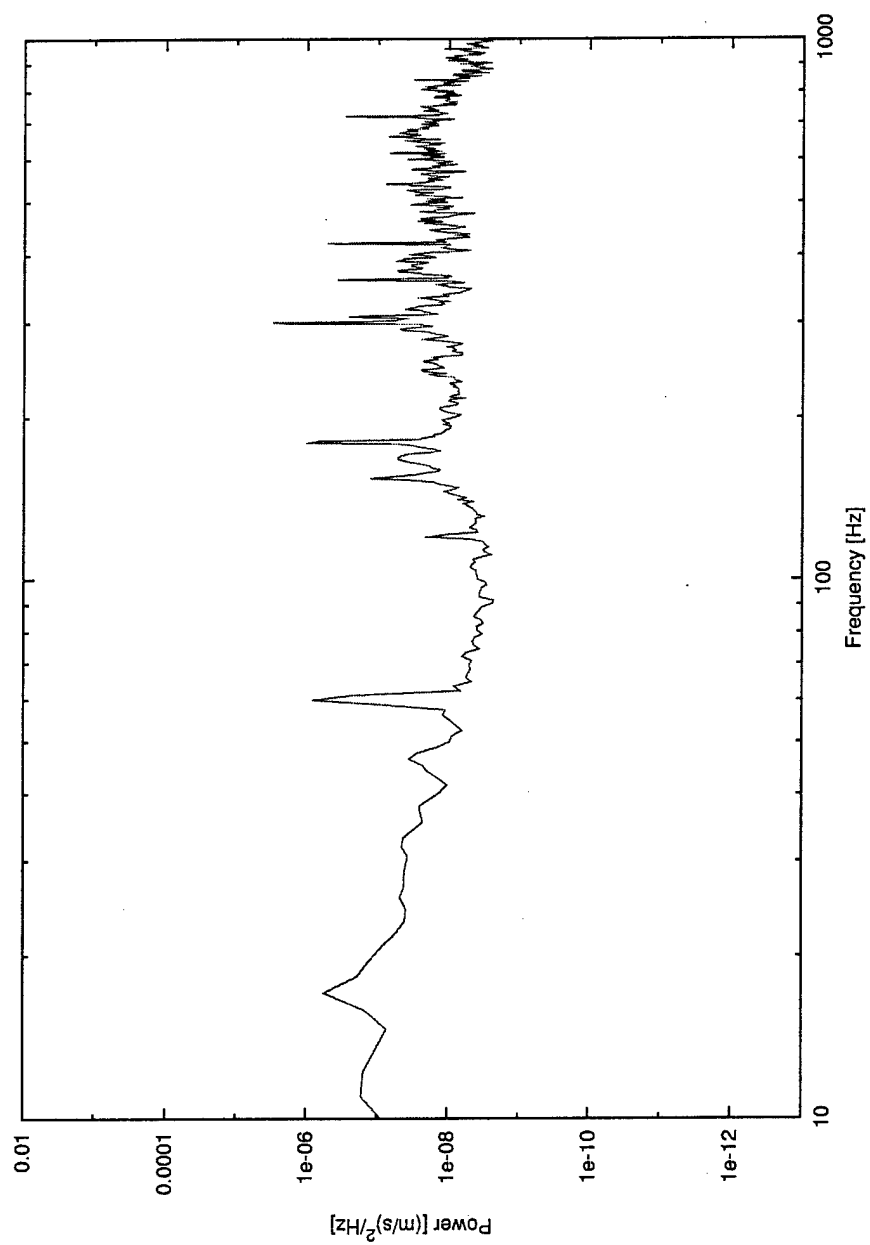
Figure 29. Freestream turbulence spectrum at $U_\infty = 21$ m/s, 10 - 1000 Hz bandpass.
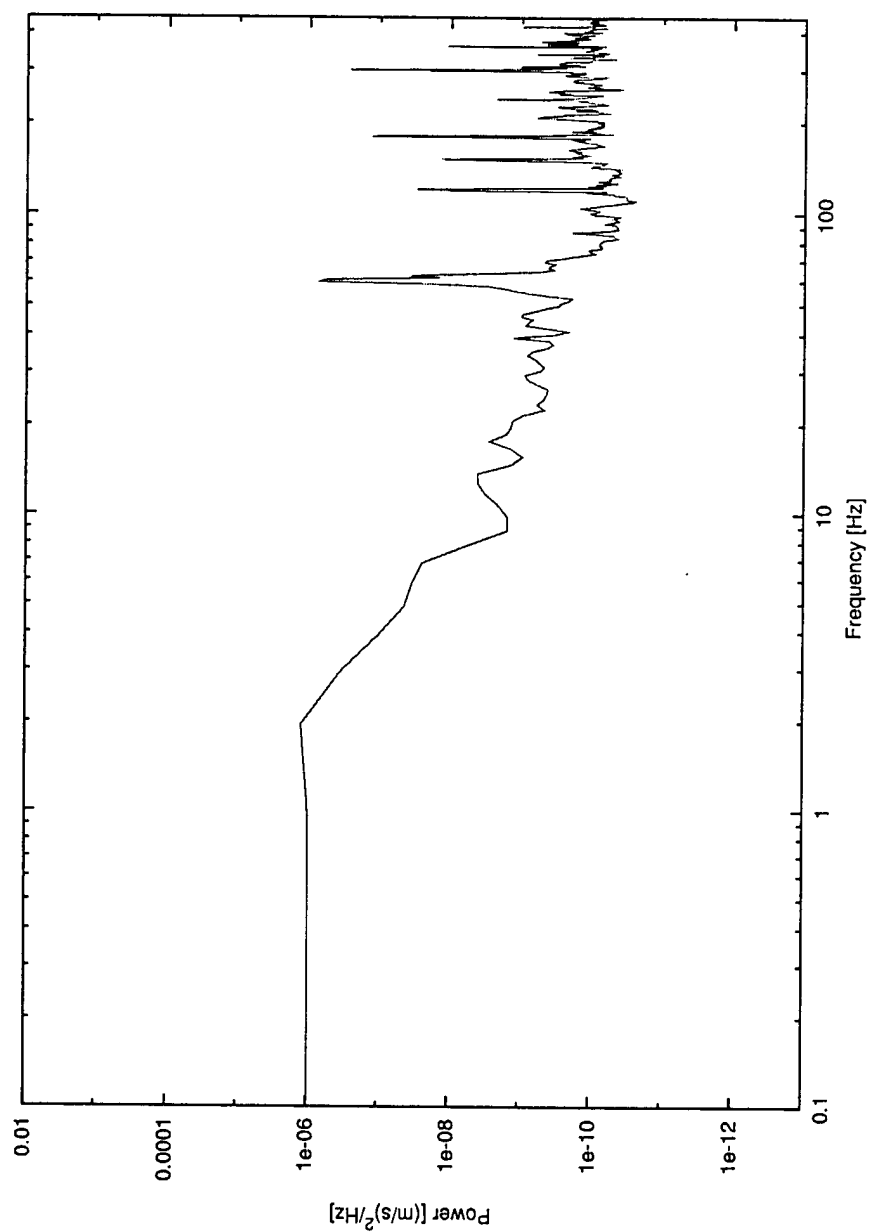
Figure 30. Freestream turbulence spectrum at $U_\infty = 8$ m/s, 1 - 450 Hz bandpass, using acoustic foam.
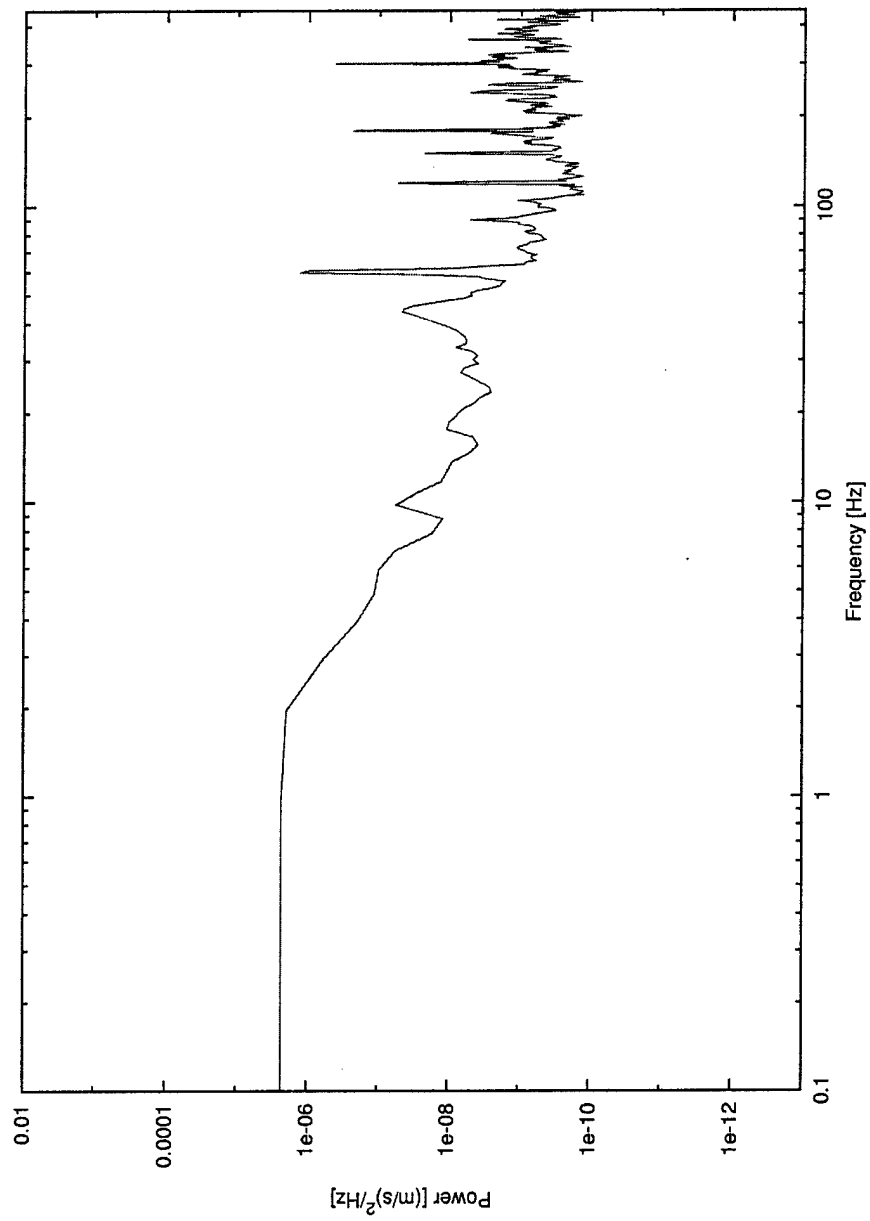
Figure 31. Freestream turbulence spectrum at $U_\infty = 12$ m/s, 1 - 450 Hz bandpass, using acoustic foam.
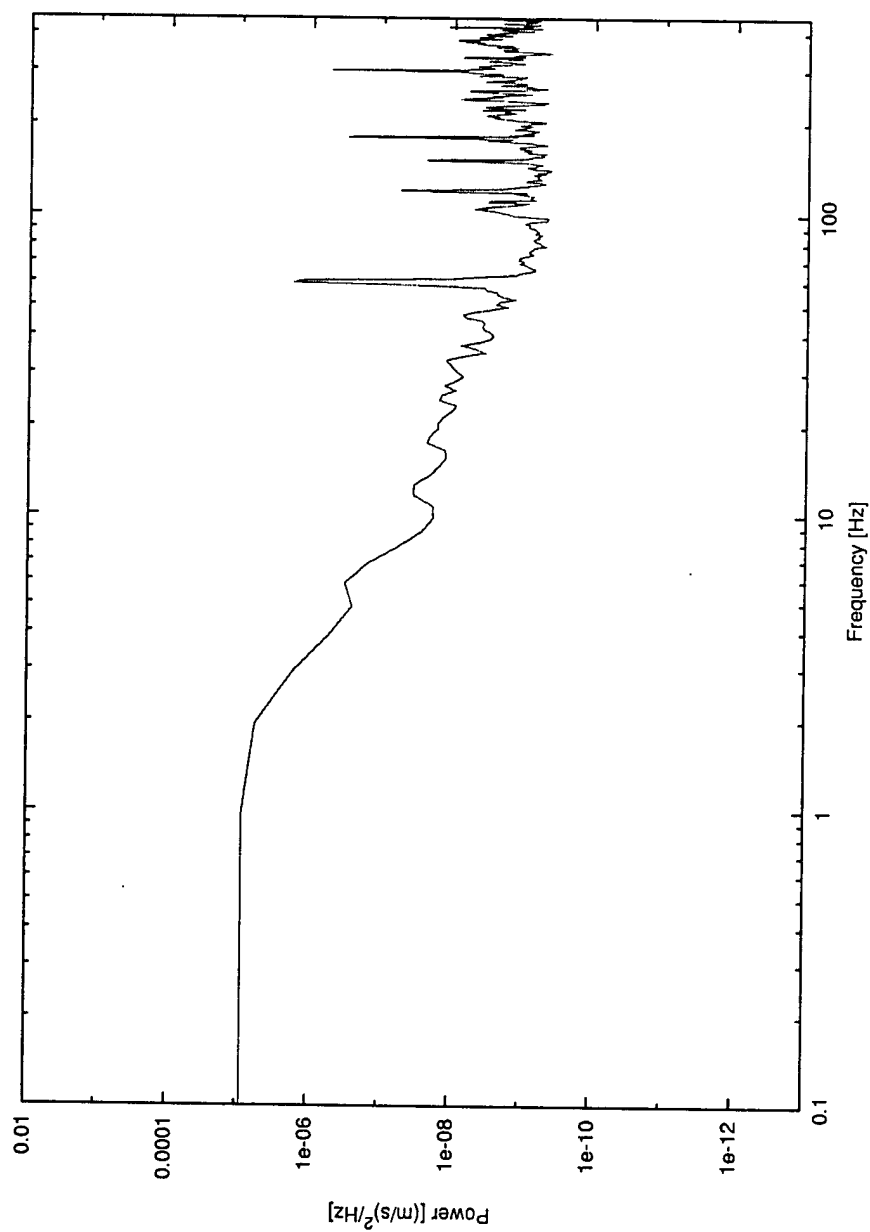
Figure 32. Freestream turbulence spectrum at $U_\infty = 15$ m/s, 1 - 450 Hz bandpass, using acoustic foam.
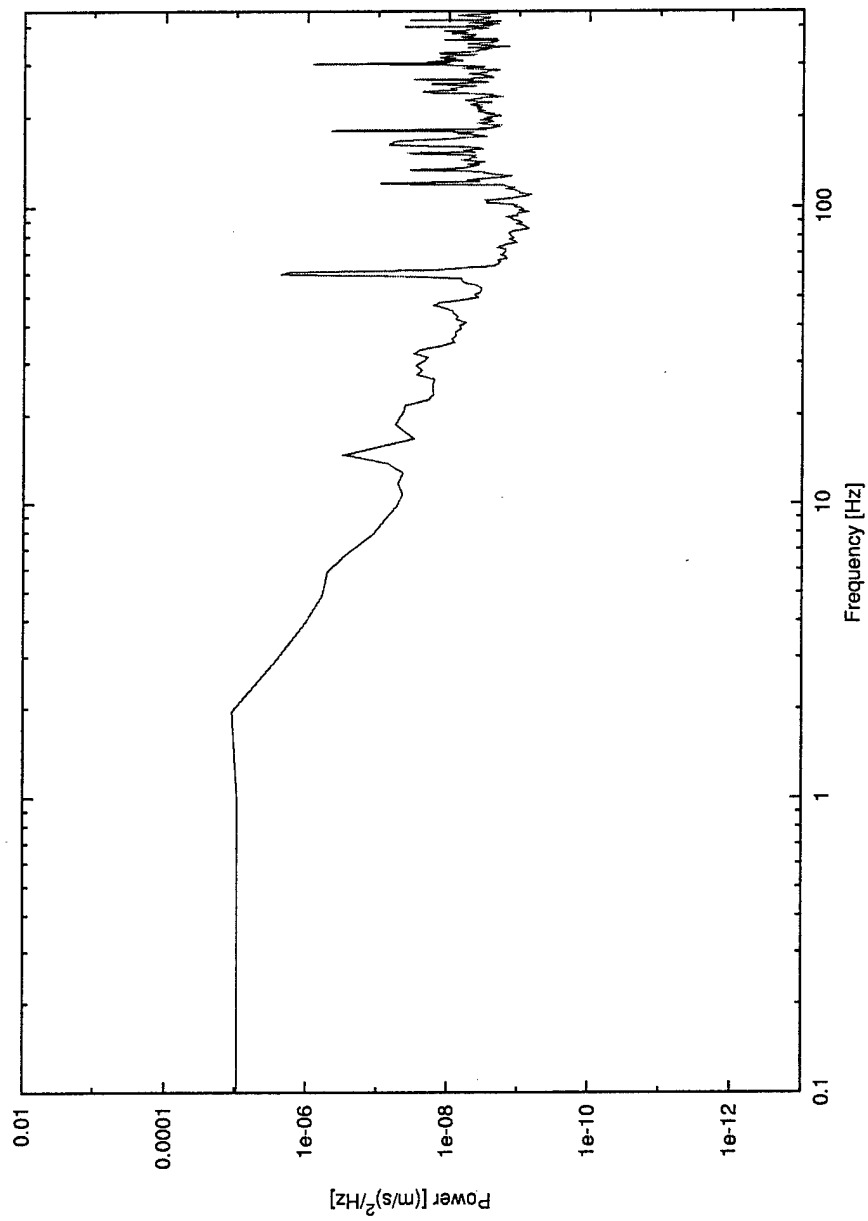
Figure 33. Freestream turbulence spectrum at U_∞ = 18 m/s, 1 - 450 Hz bandpass, using acoustic foam.
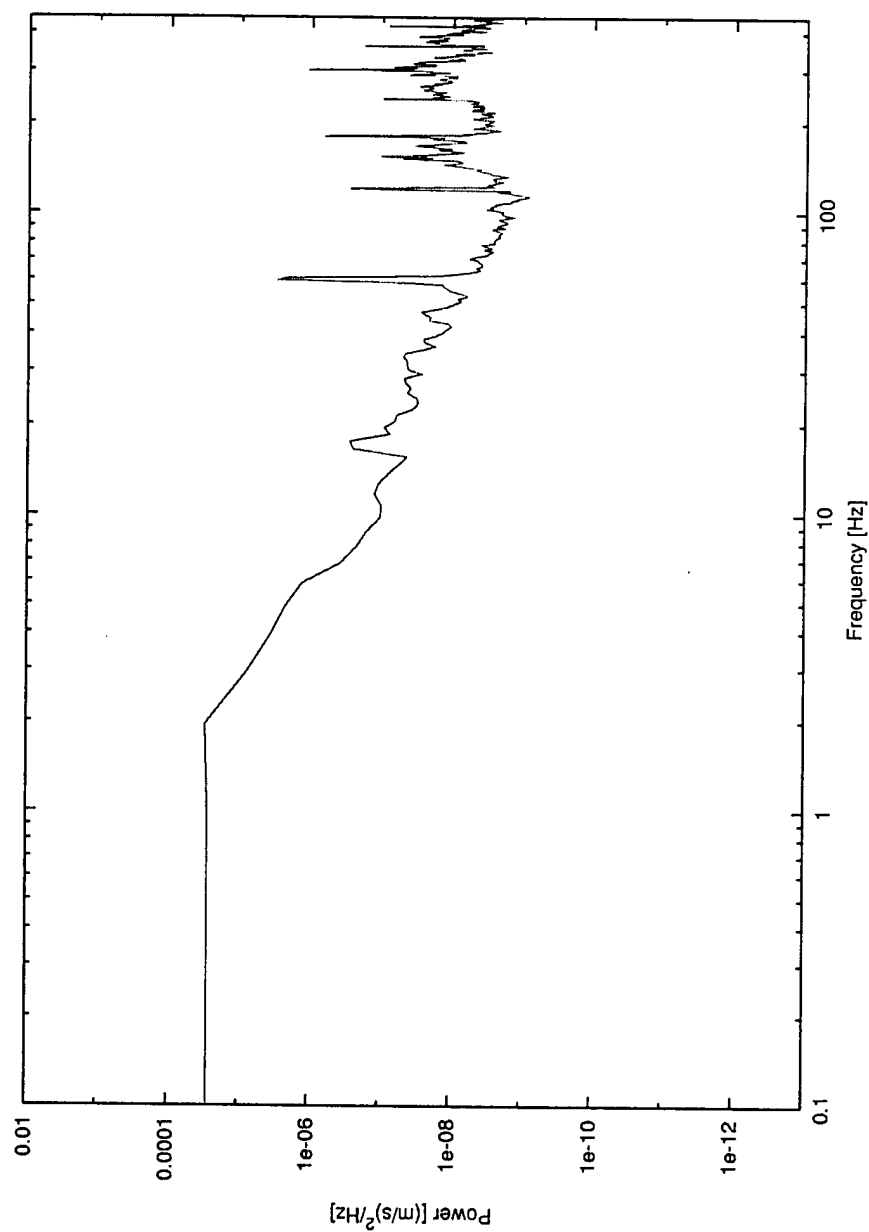
Figure 34. Freestream turbulence spectrum at $U_\infty = 21$ m/s, 1 - 450 Hz bandpass, using acoustic foam.
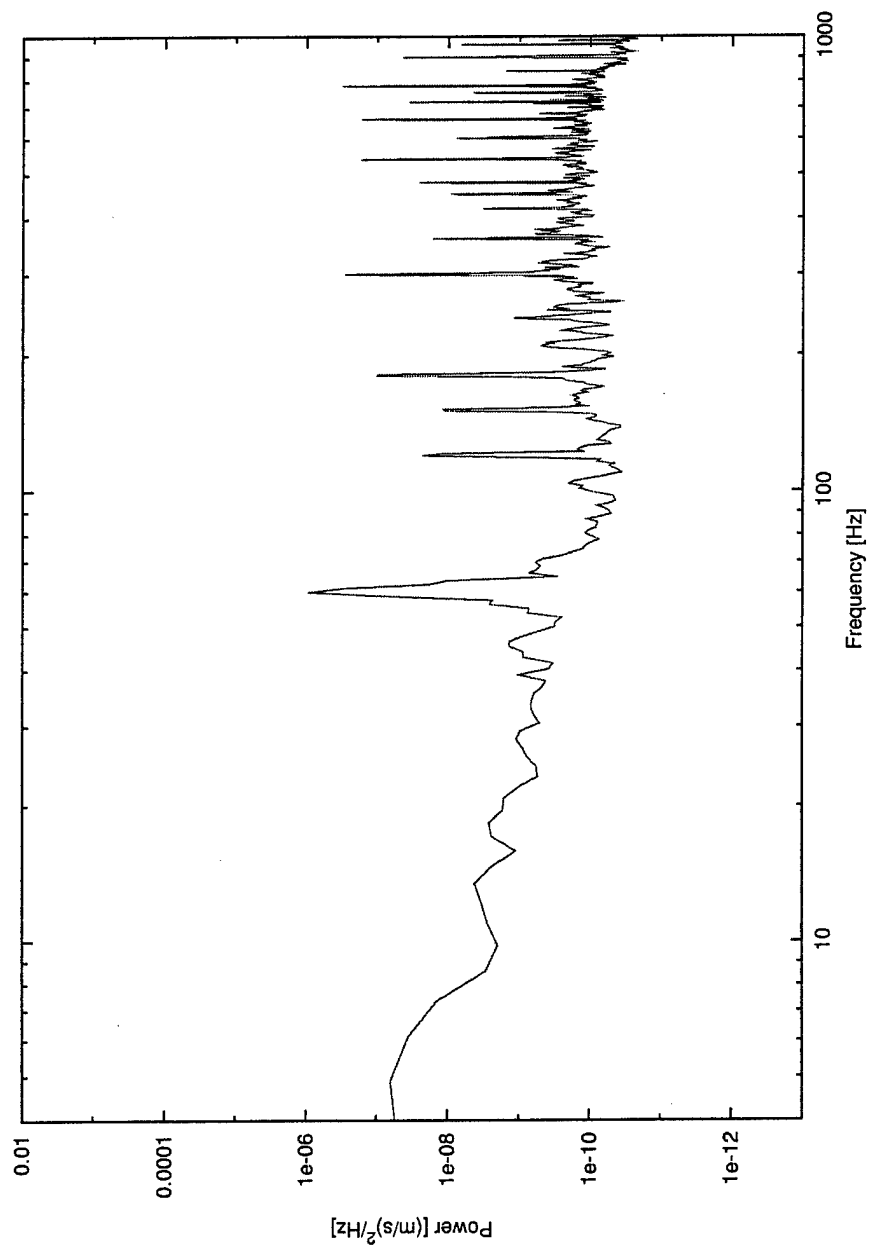
Figure 35. Freestream turbulence spectrum at $U_\infty = 8$ m/s, 4 - 1000 Hz bandpass, using acoustic foam.
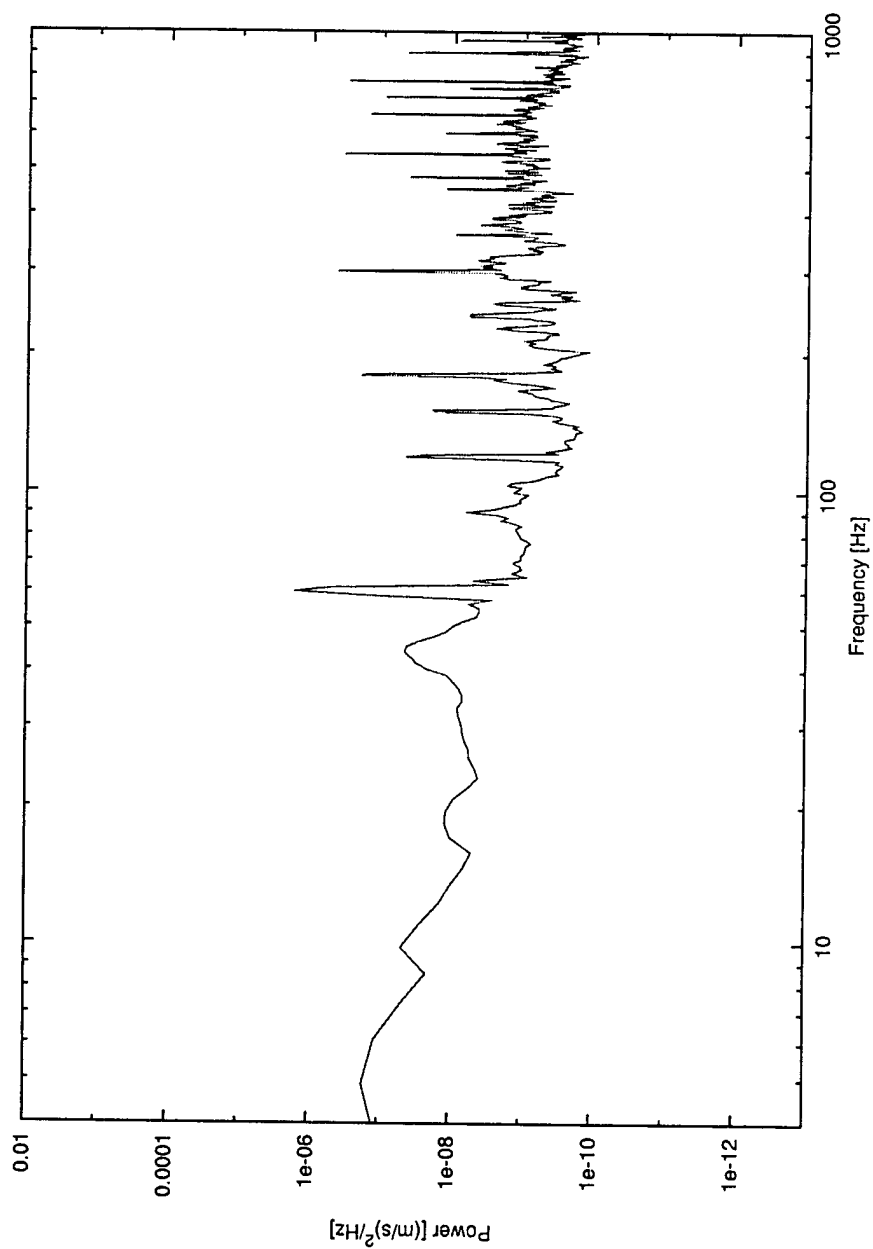
Figure 36. Freestream turbulence spectrum at $U_\infty = 12$ m/s, 4 - 1000 Hz bandpass, using acoustic foam.
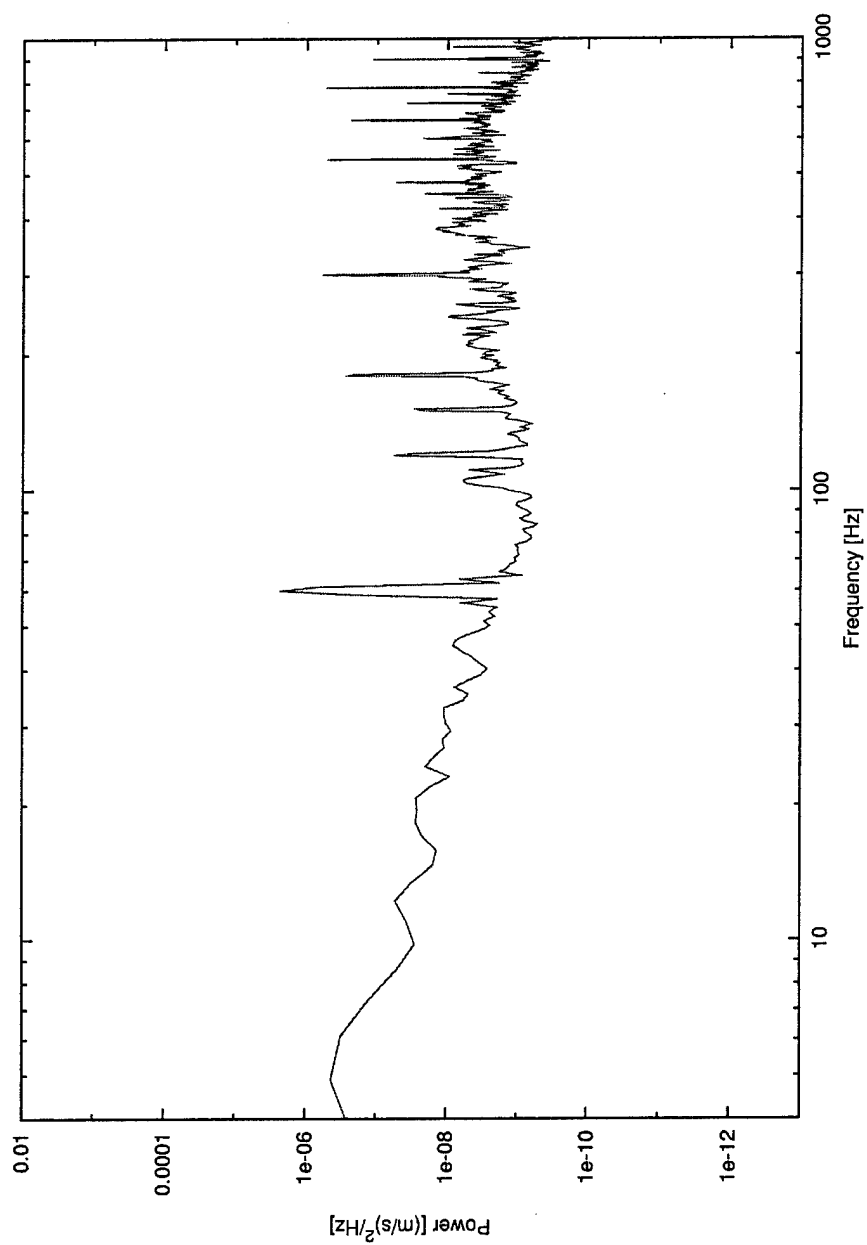
Figure 37. Freestream turbulence spectrum at $U_\infty = 15$ m/s, 4 - 1000 Hz bandpass, using acoustic foam.
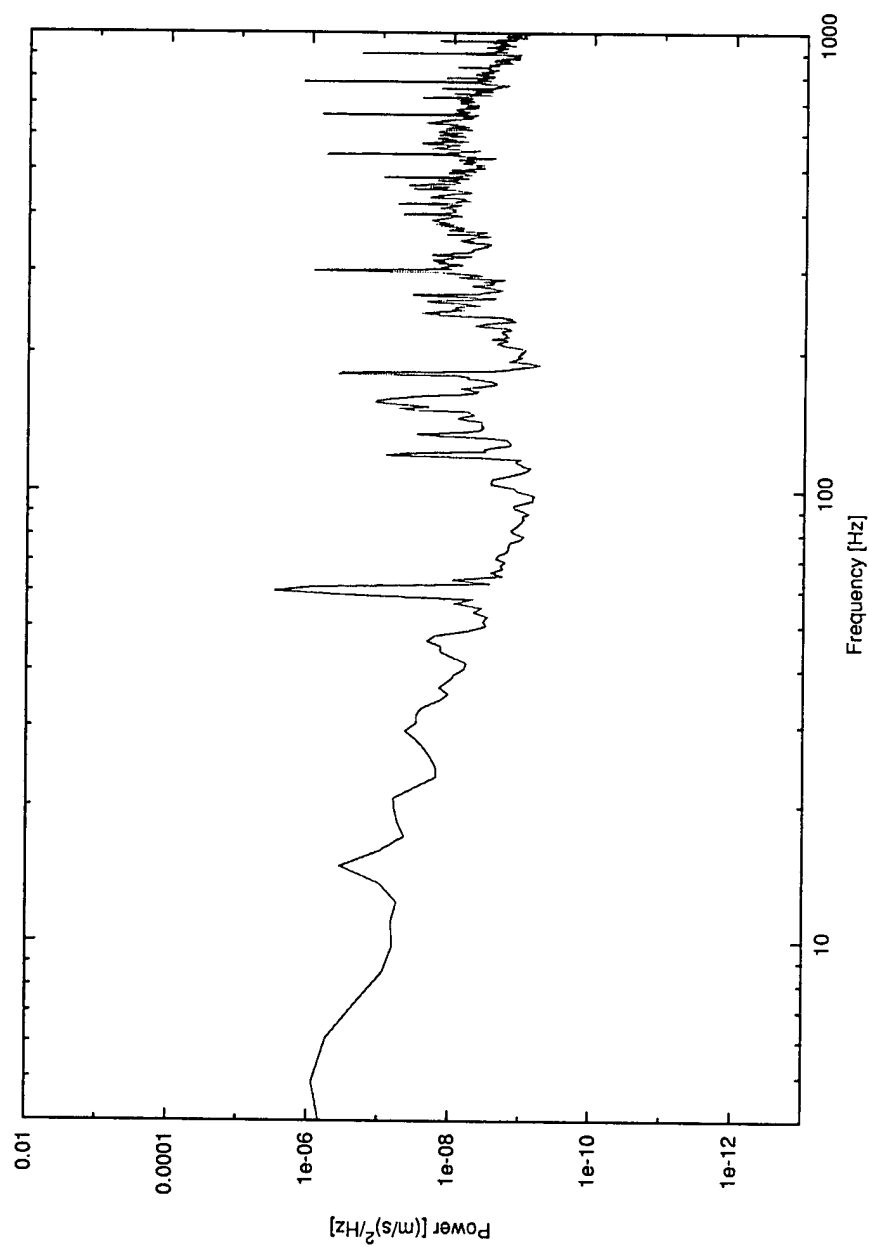
Figure 38. Freestream turbulence spectrum at $U_\infty = 18$ m/s, 4 - 1000 Hz bandpass, using acoustic foam.
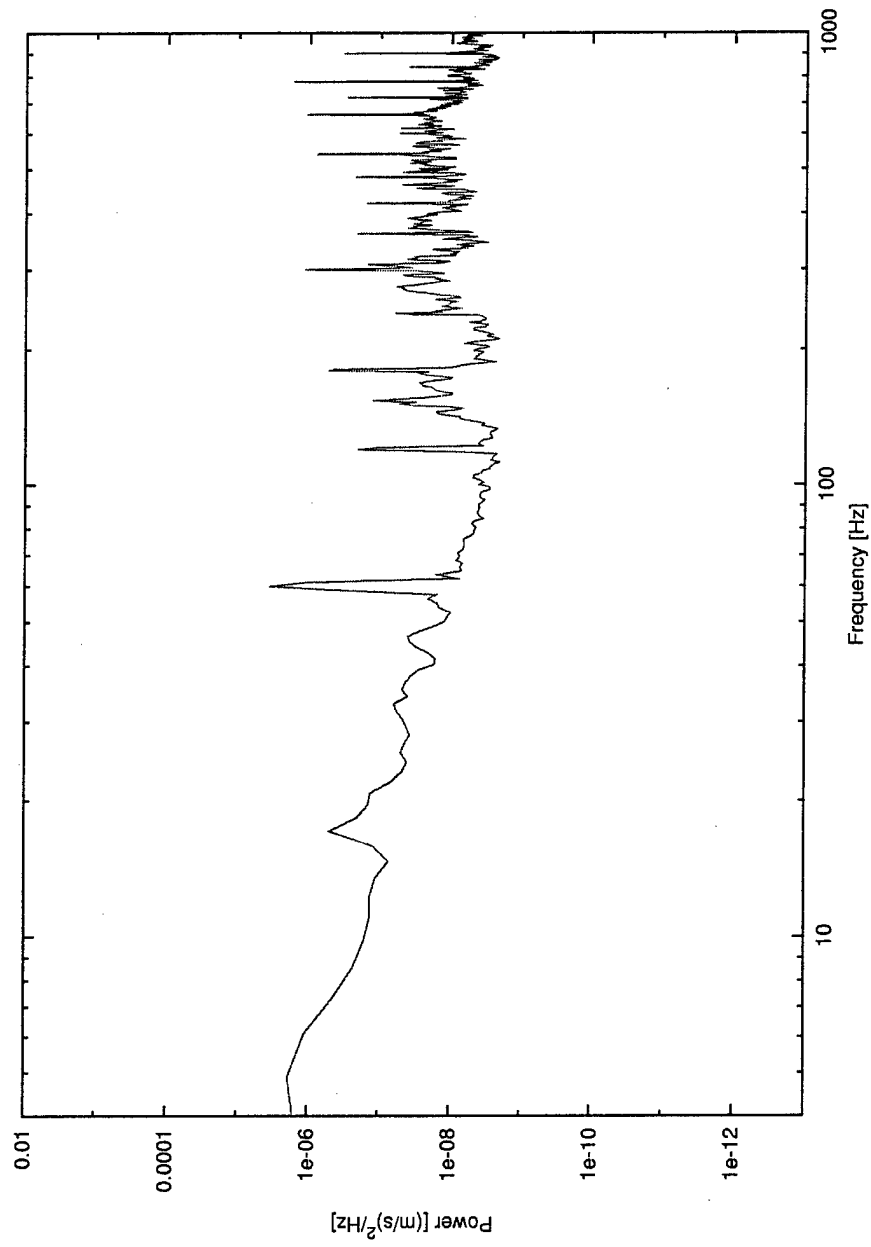
Figure 39. Freestream turbulence spectrum at $U_\infty = 21$ m/s, 4 - 1000 Hz bandpass, using acoustic foam.

Figure 40. Freestream turbulence spectrum at $U_\infty = 8$ m/s, 10 - 1000 Hz bandpass, using acoustic foam.

Figure 41. Freestream turbulence spectrum at $U_\infty = 12$ m/s, 10 - 1000 Hz bandpass, using acoustic foam.

Figure 42. Freestream turbulence spectrum at $U_\infty = 15$ m/s, 10 - 1000 Hz bandpass, using acoustic foam.

Figure 43. Freestream turbulence spectrum at $U_\infty = 18$ m/s, 10 - 1000 Hz bandpass, using acoustic foam.
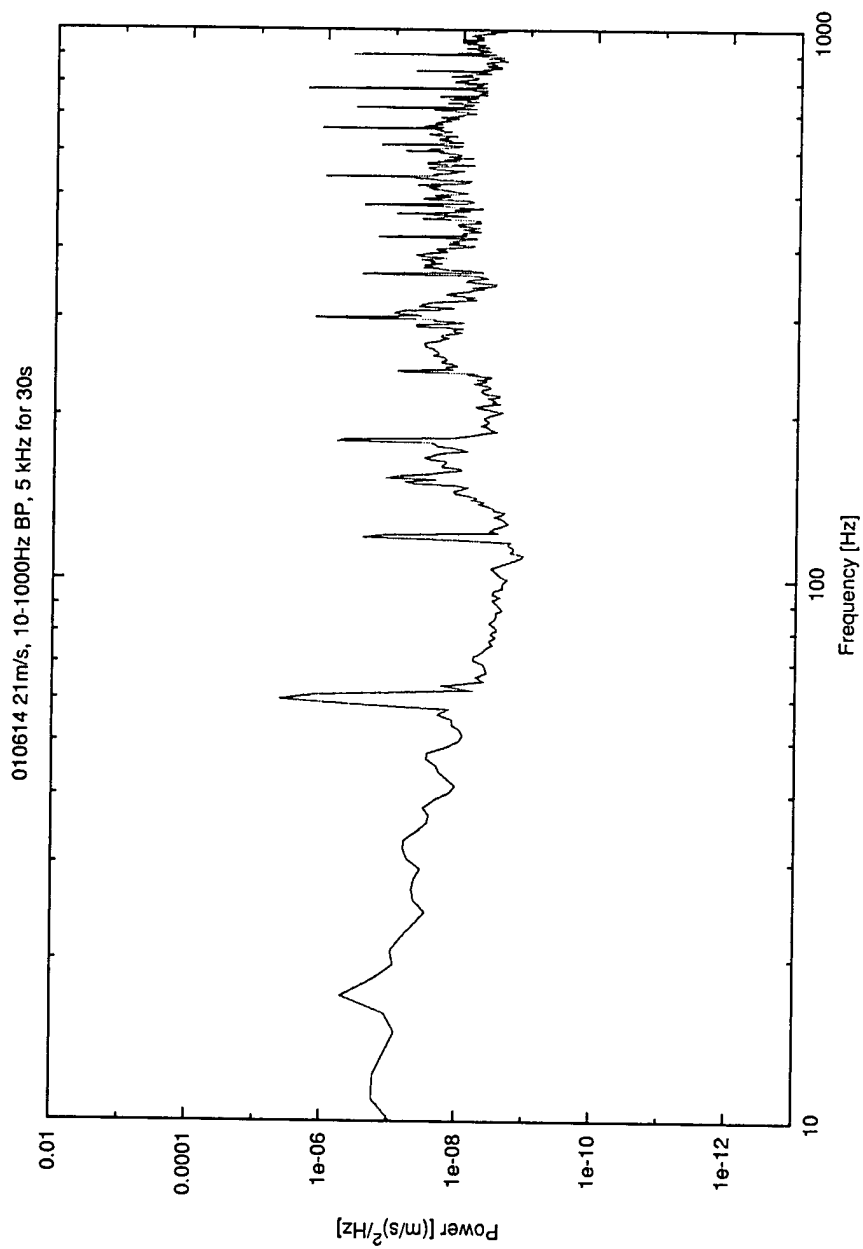
Figure 44. Freestream turbulence spectrum at $U_\infty = 21$ m/s, 10 - 1000 Hz bandpass, using acoustic foam.
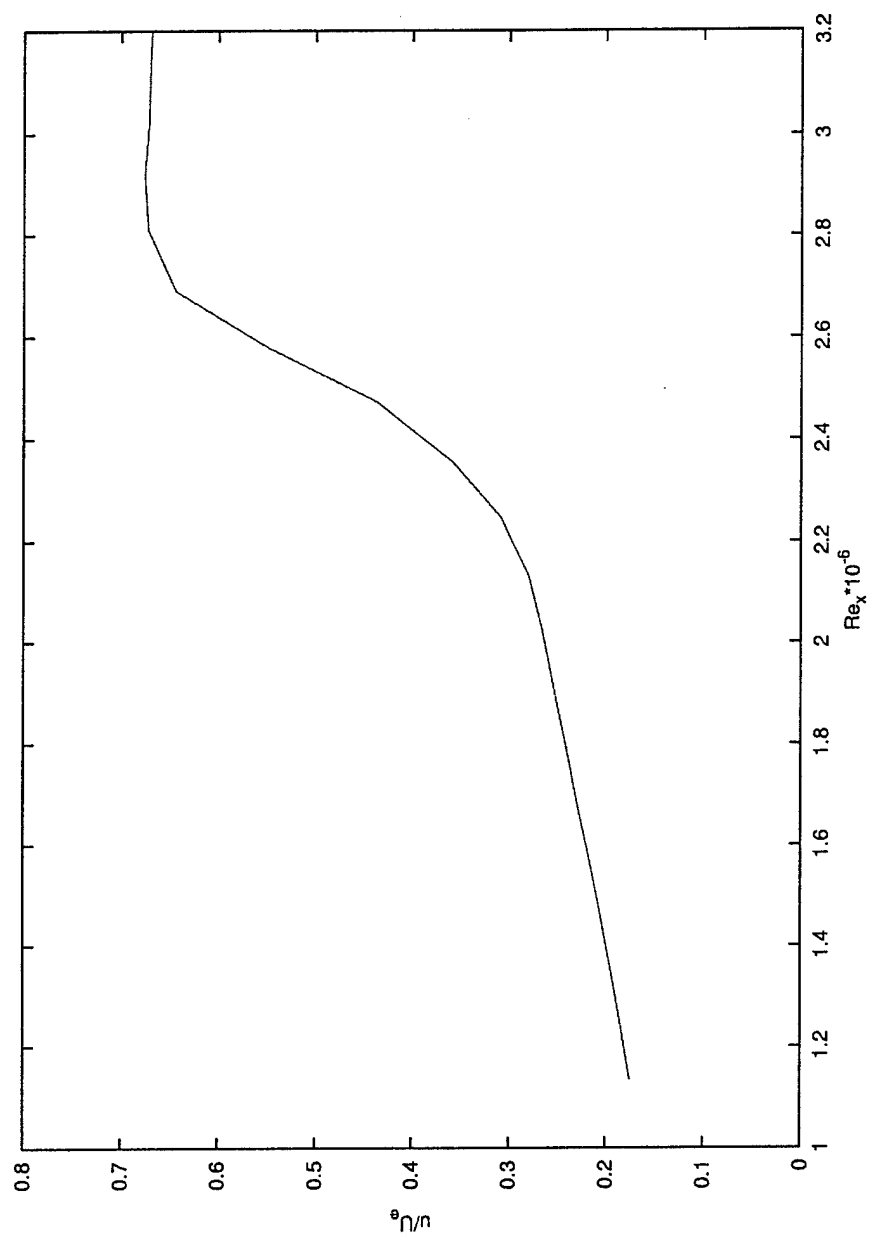
Figure 45. Transition Reynolds number. Fixed hotwire at x=1.8 m, y=1.0 mm
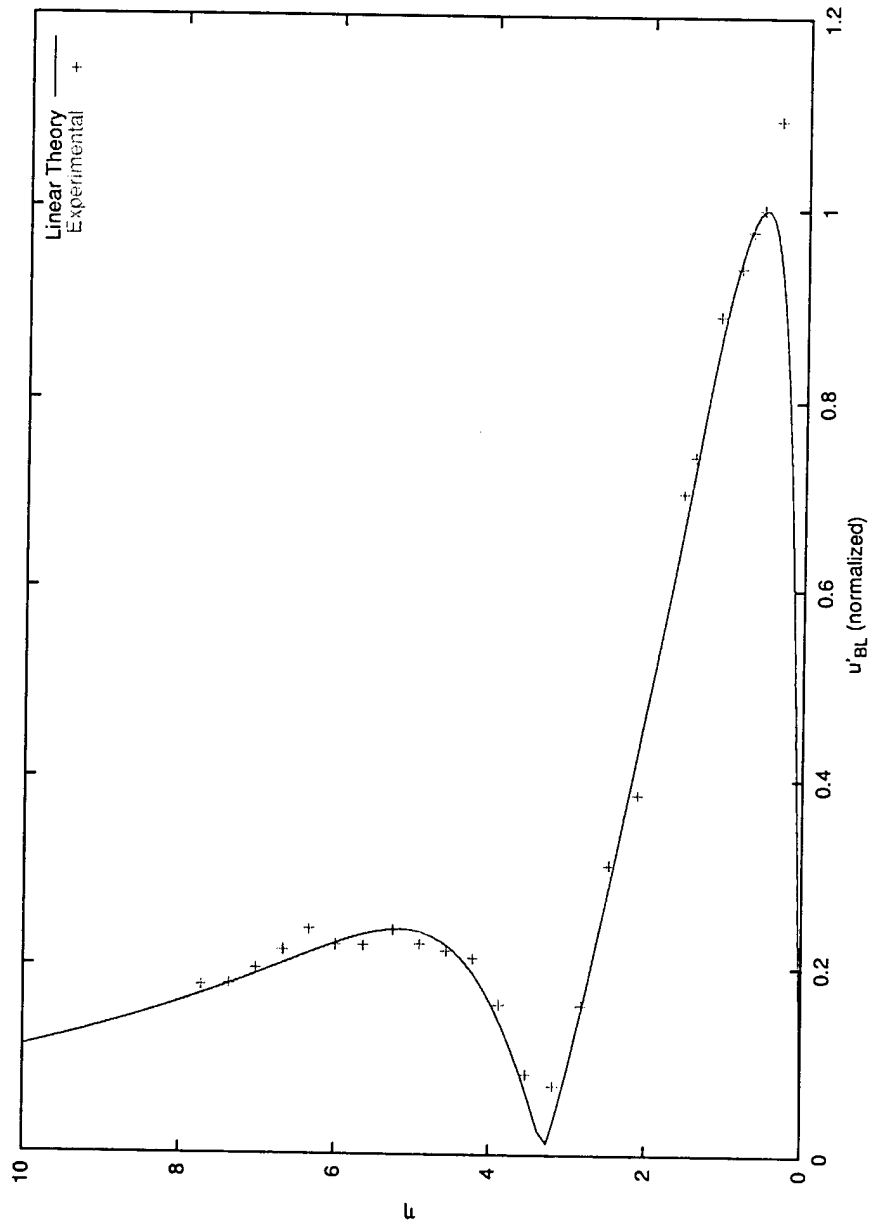
Figure 46. The T-S modeshape profile for $U_\infty = 12$ m/s and
$F = 59.8$.
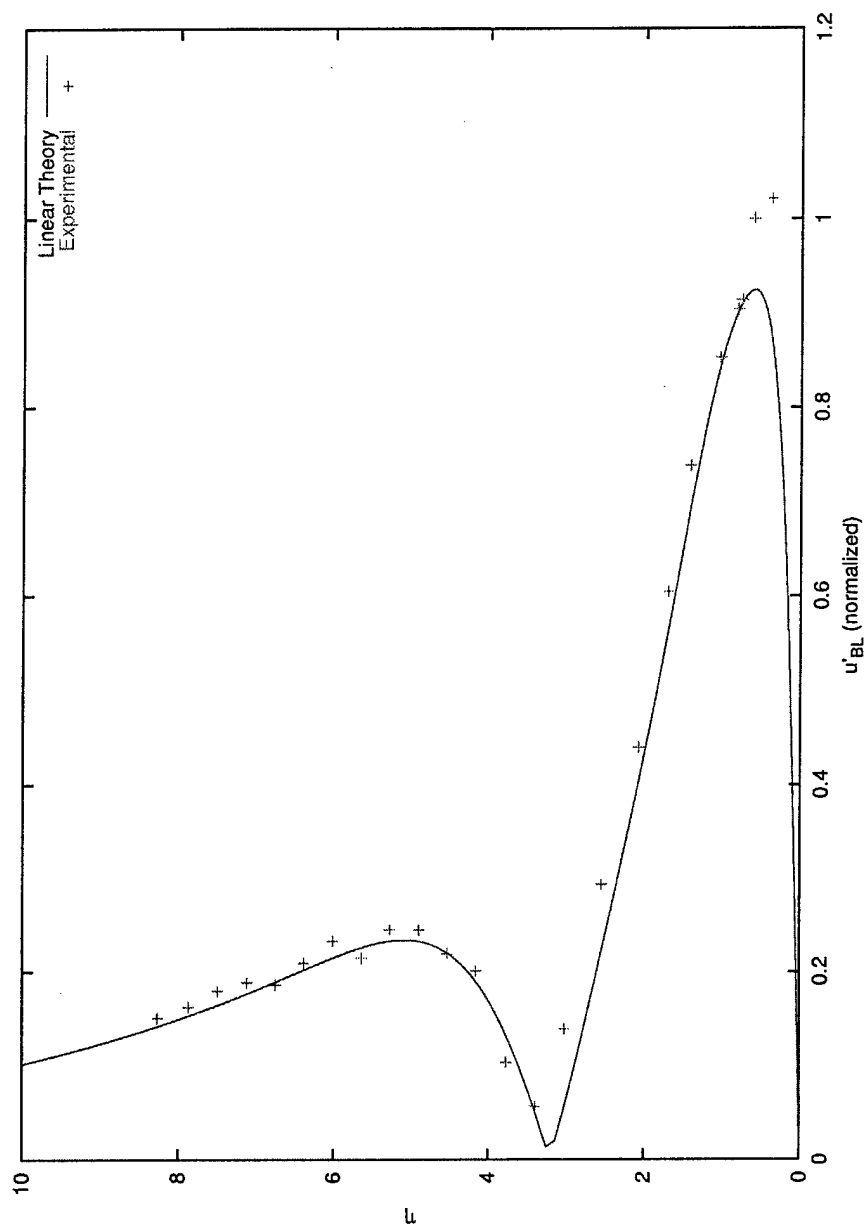
Figure 47. The T-S modeshape profile for $U_\infty = 15$ m/s and $F = 47.6$.
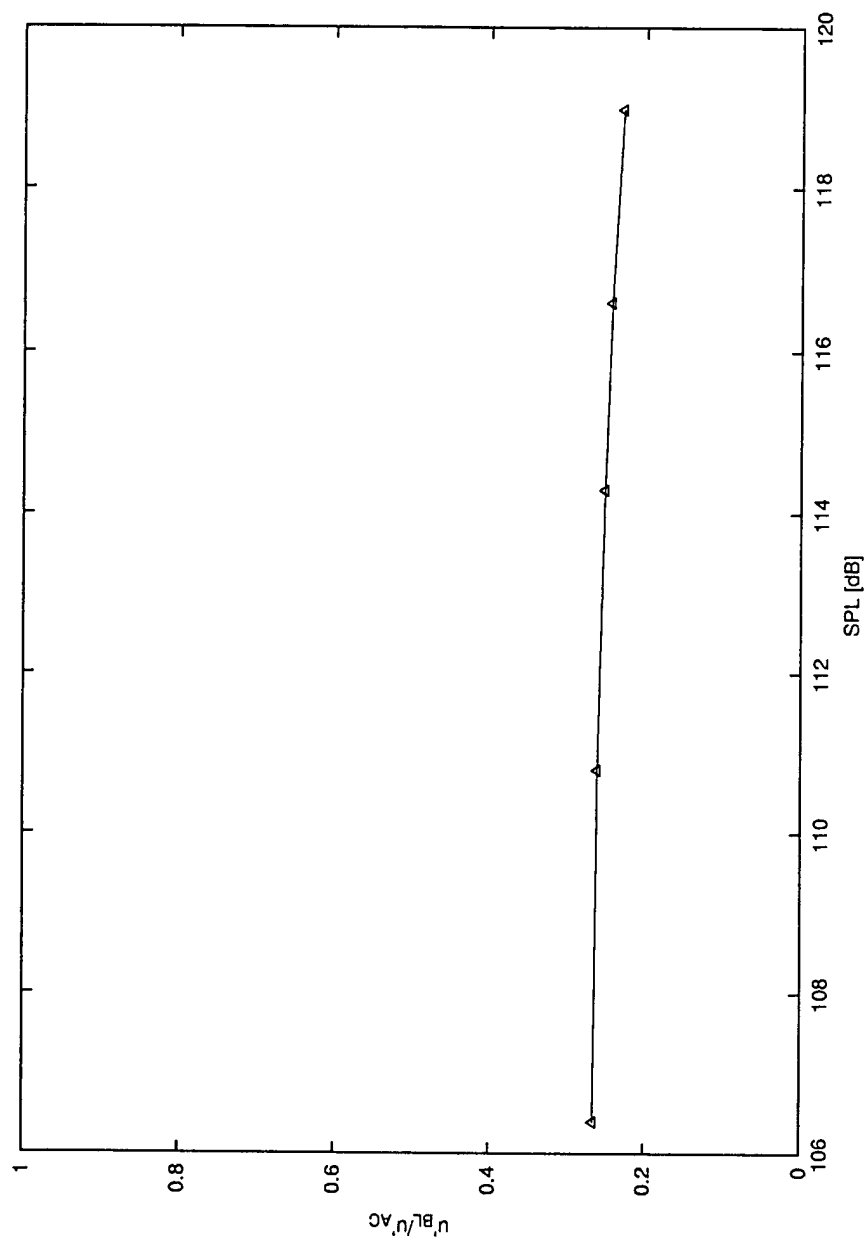
Figure 48. Disturbance amplitude versus freestream sound pressure level for $U_\infty = 8$ m/s.
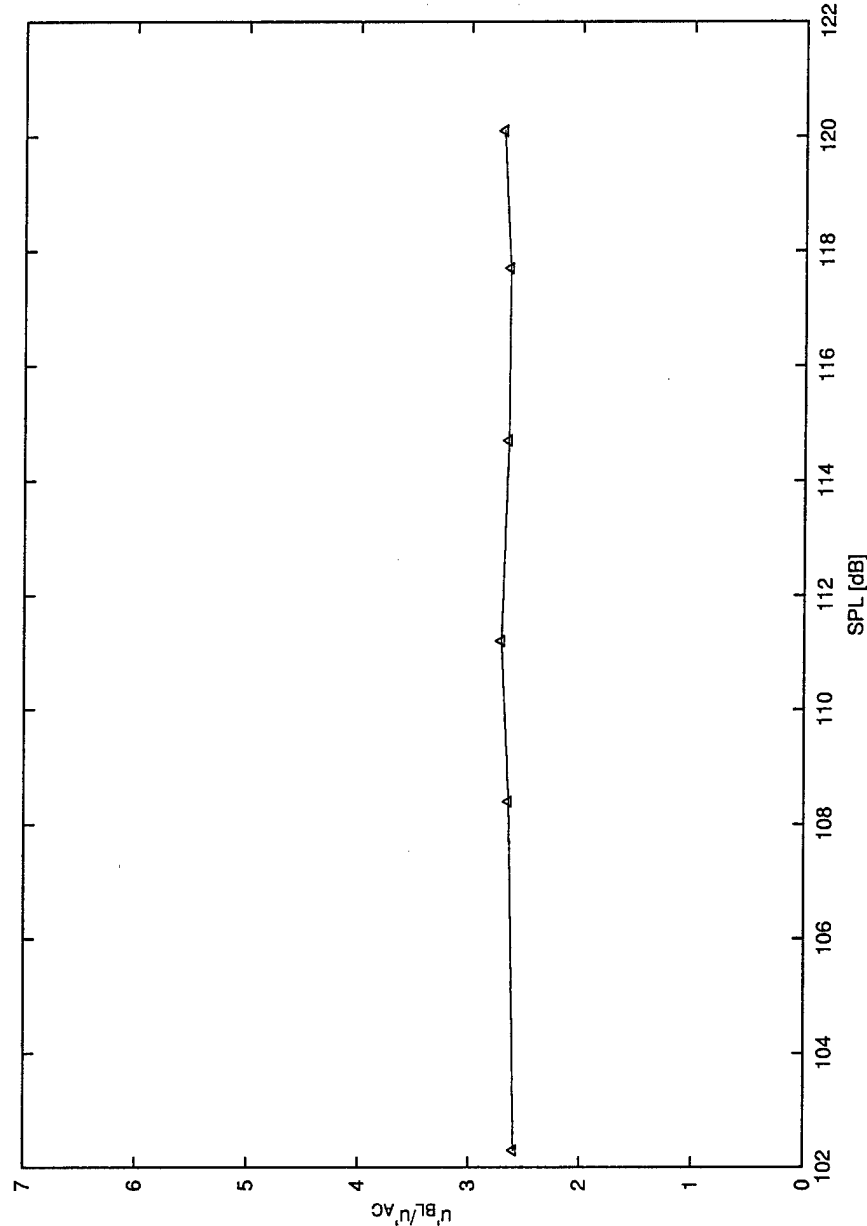
Figure 49. Disturbance amplitude versus freestream sound pressure level for $U_\infty = 12$ m/s.
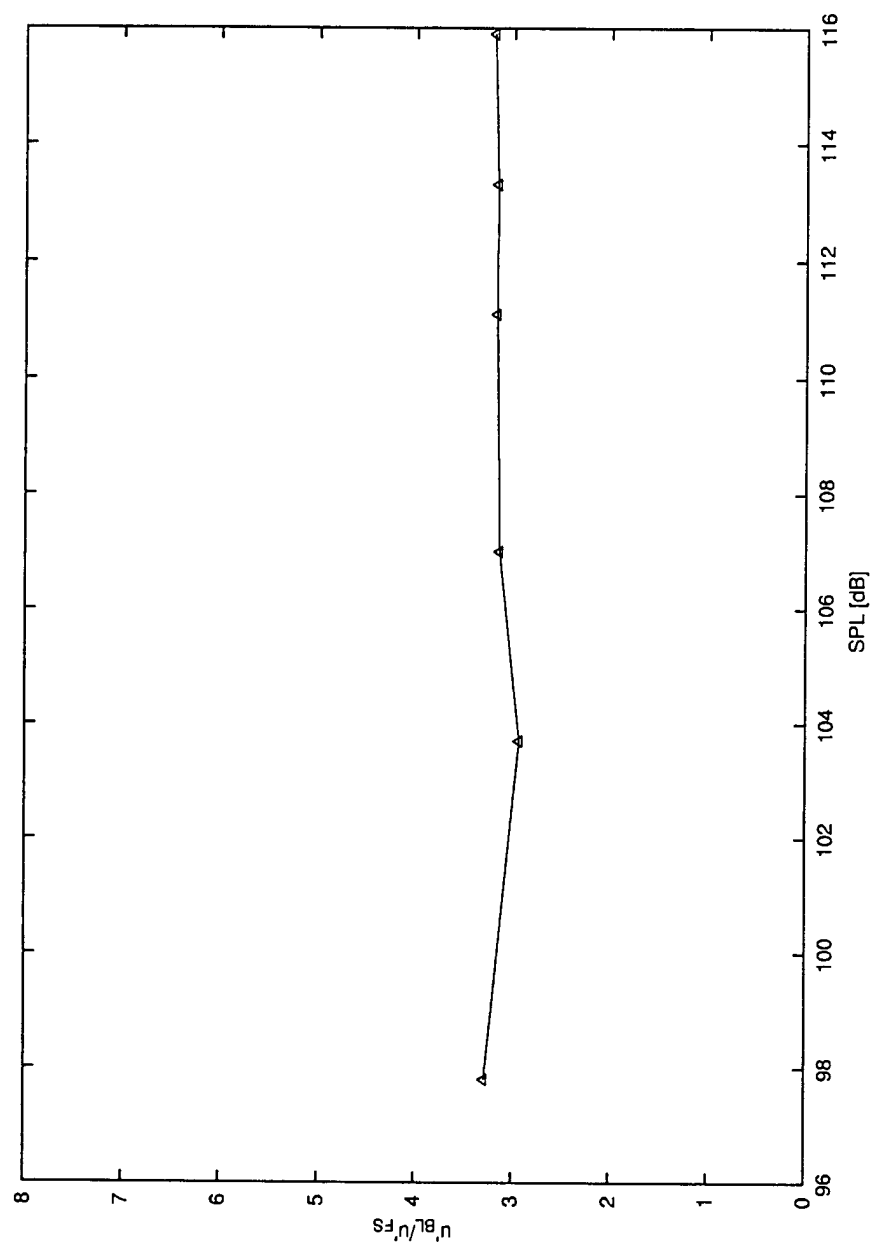
Figure 50. Disturbance amplitude versus freestream sound pressure level for $U_\infty = 15$ m/s.
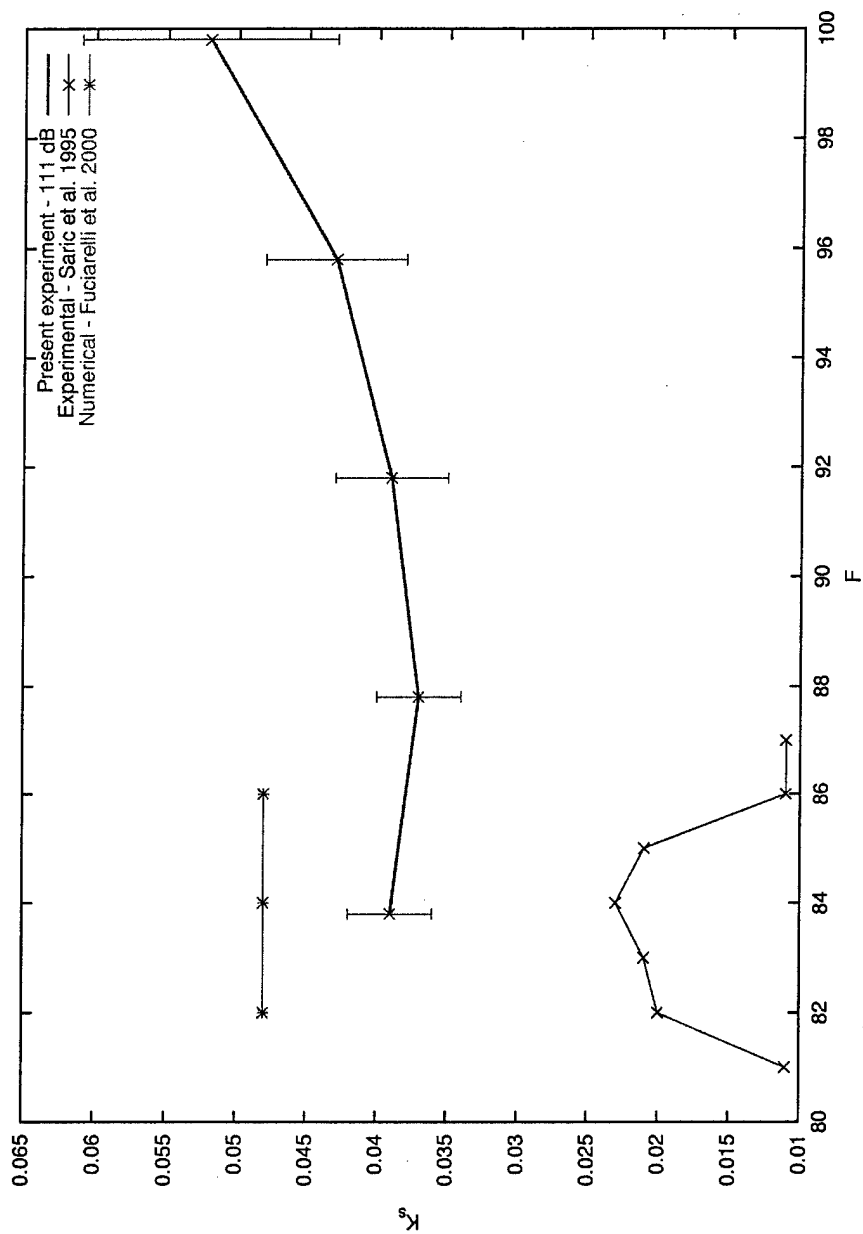
Figure 51. Receptivity coefficients for $U_\infty = 8$ m/s, and comparison to Saric et al. (1995), and Fuciarelli et al. (2000).
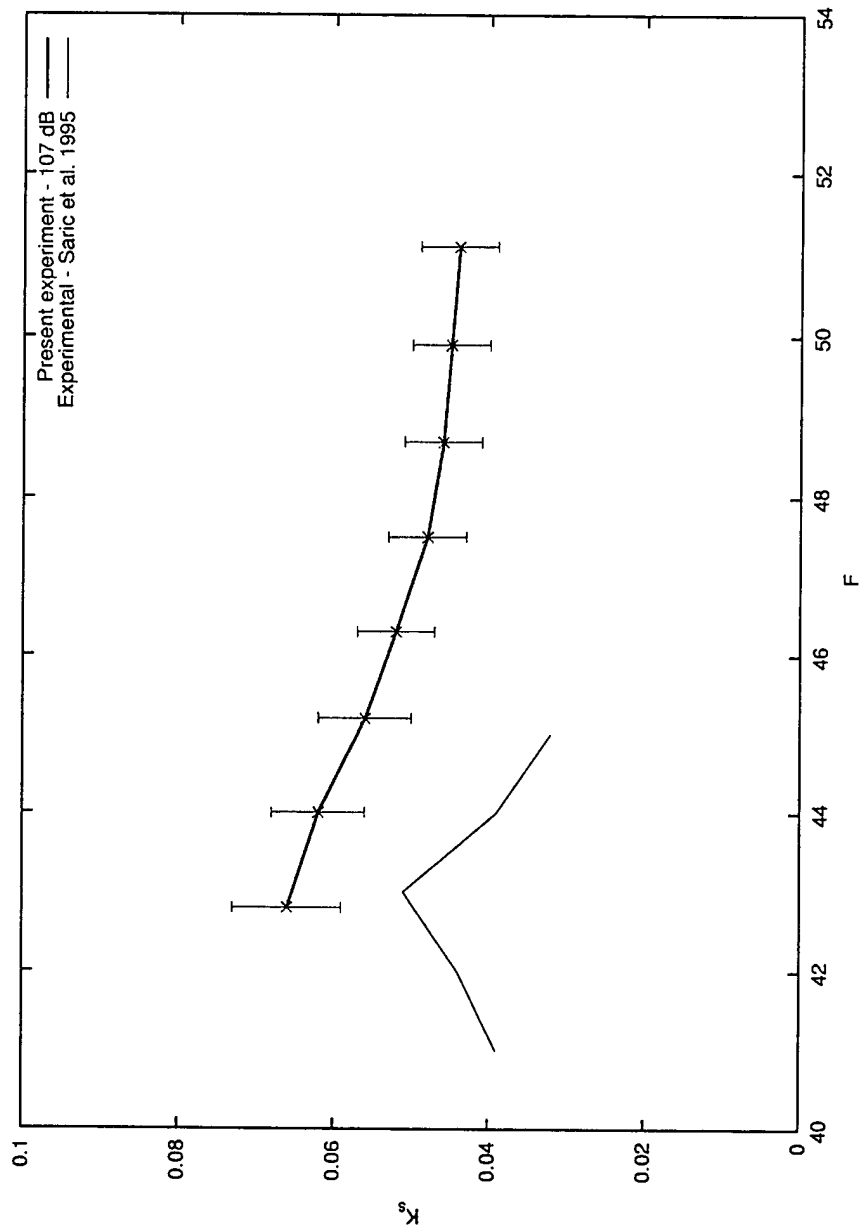
Figure 52. Receptivity coefficients for $U_\infty = 15$ m/s, and comparison to Saric et al. (1995).
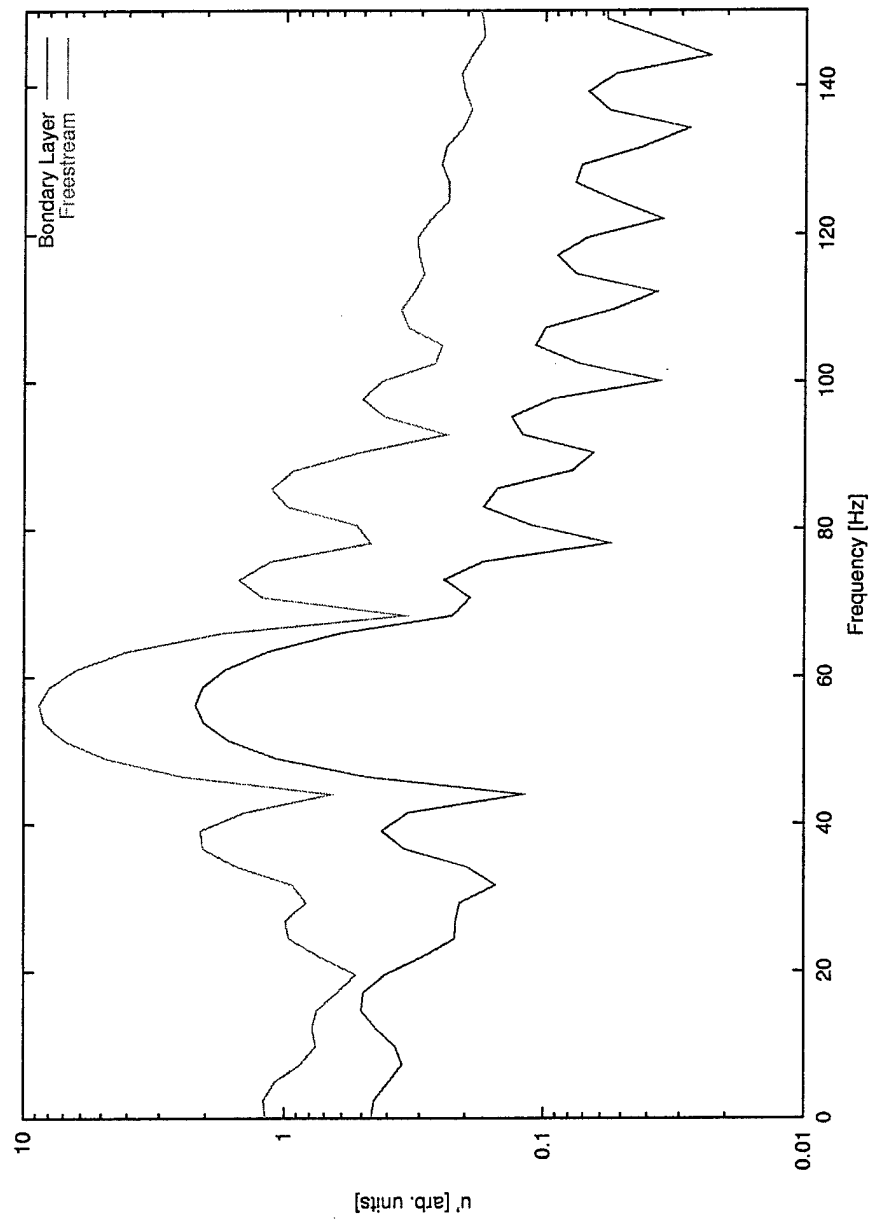
Figure 53. Acoustic and T-S spectra; $U_\infty = 8$ m/s, 5-cycle, 55.6 Hz pulse, SPL = 114 dB.
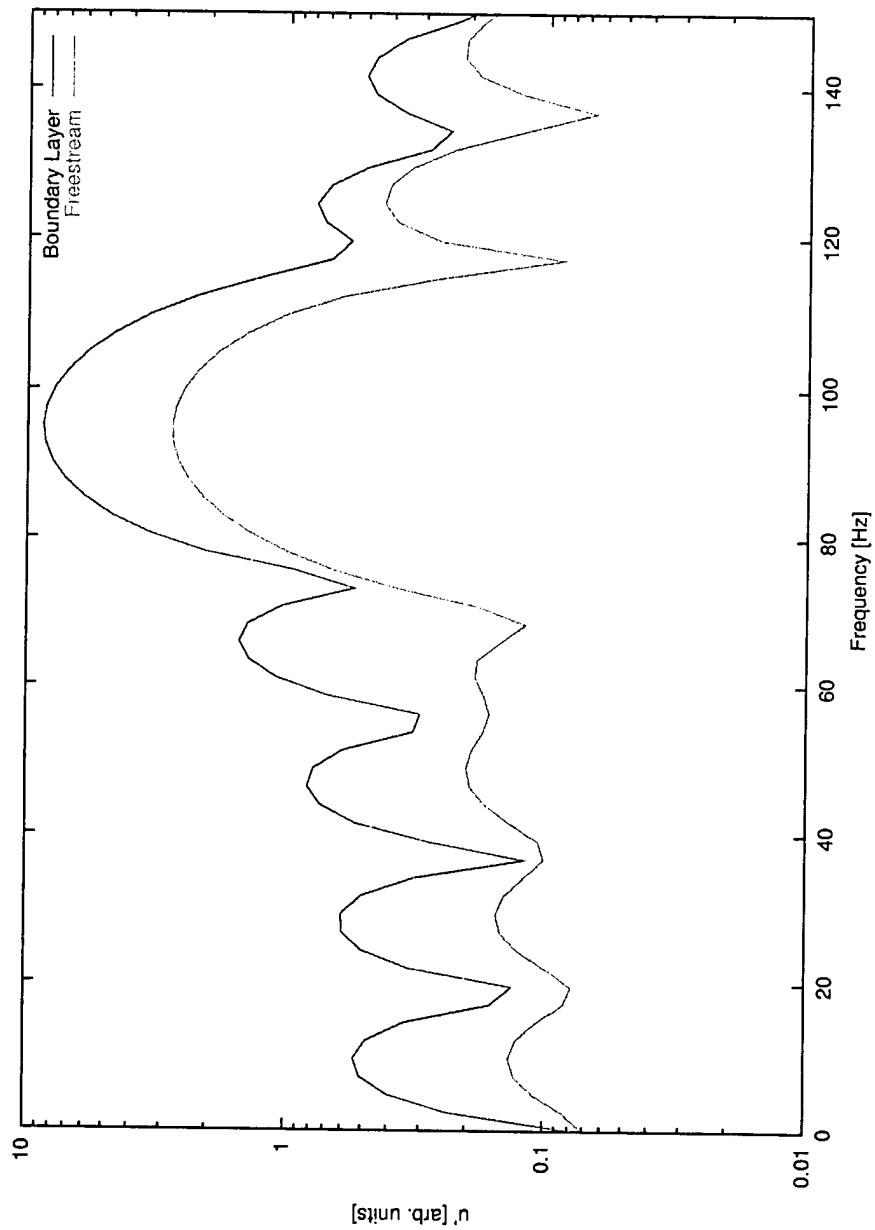
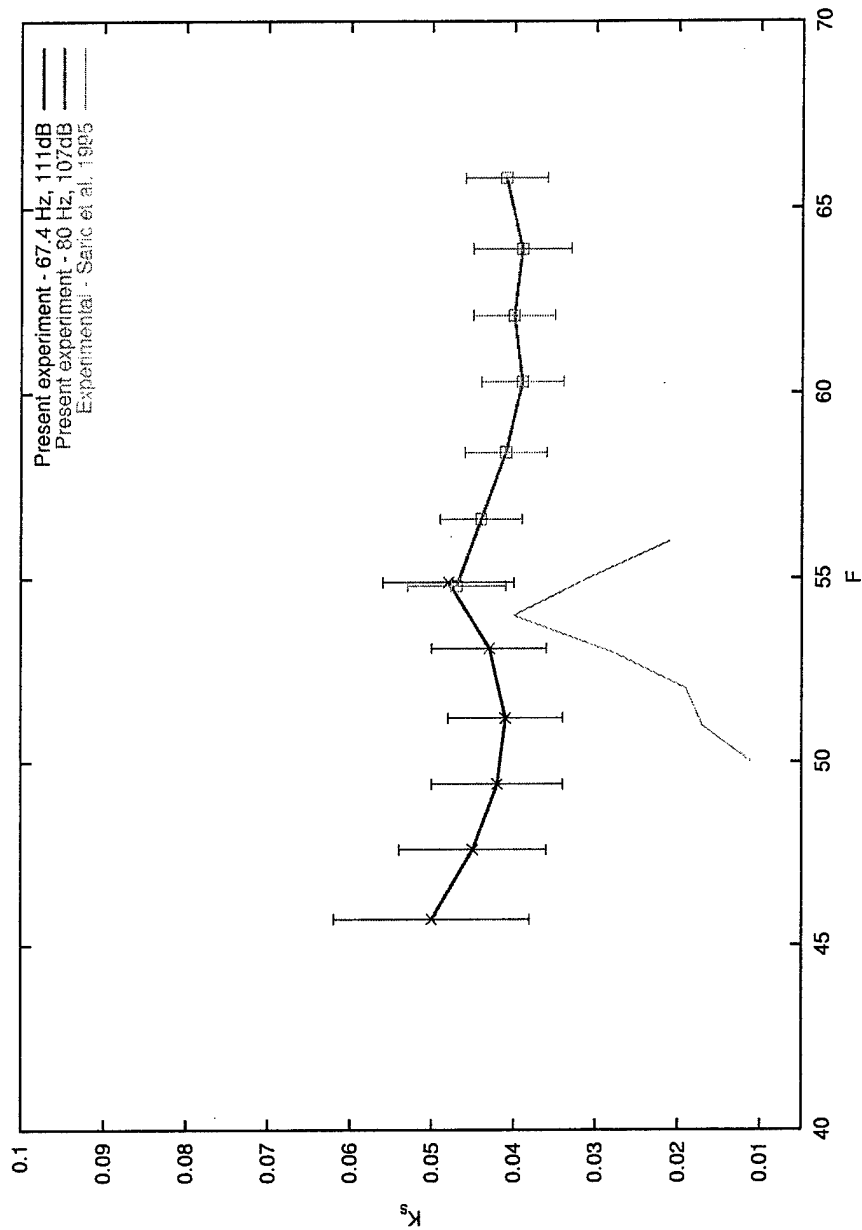Figure 54. Acoustic and T-S spectra; $U_\infty = 15$ m/s, 5-cycle, 97Hz pulse, SPL = 107 dB.

Figure 55. Receptivity coefficients for $U_\infty = 12$ m/s, and comparison to Saric et al. (1995).
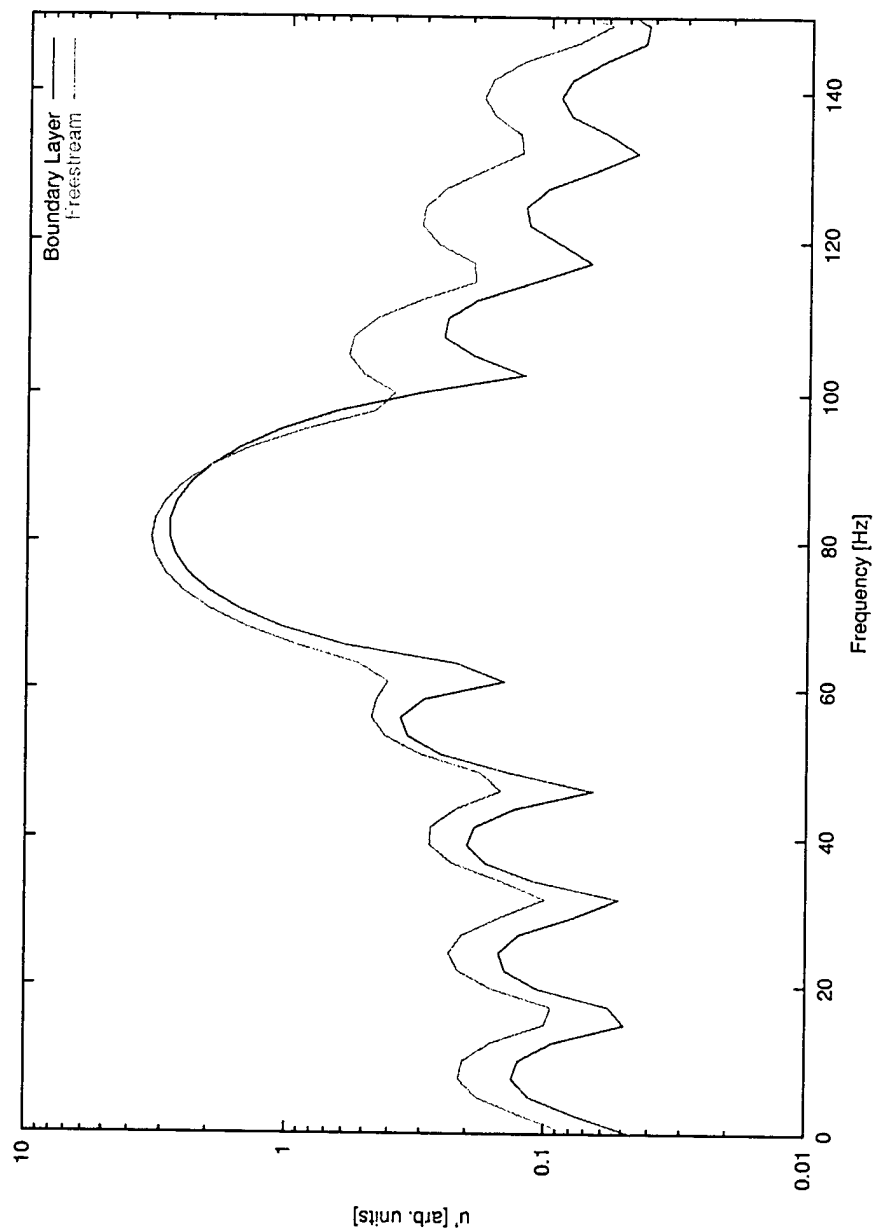
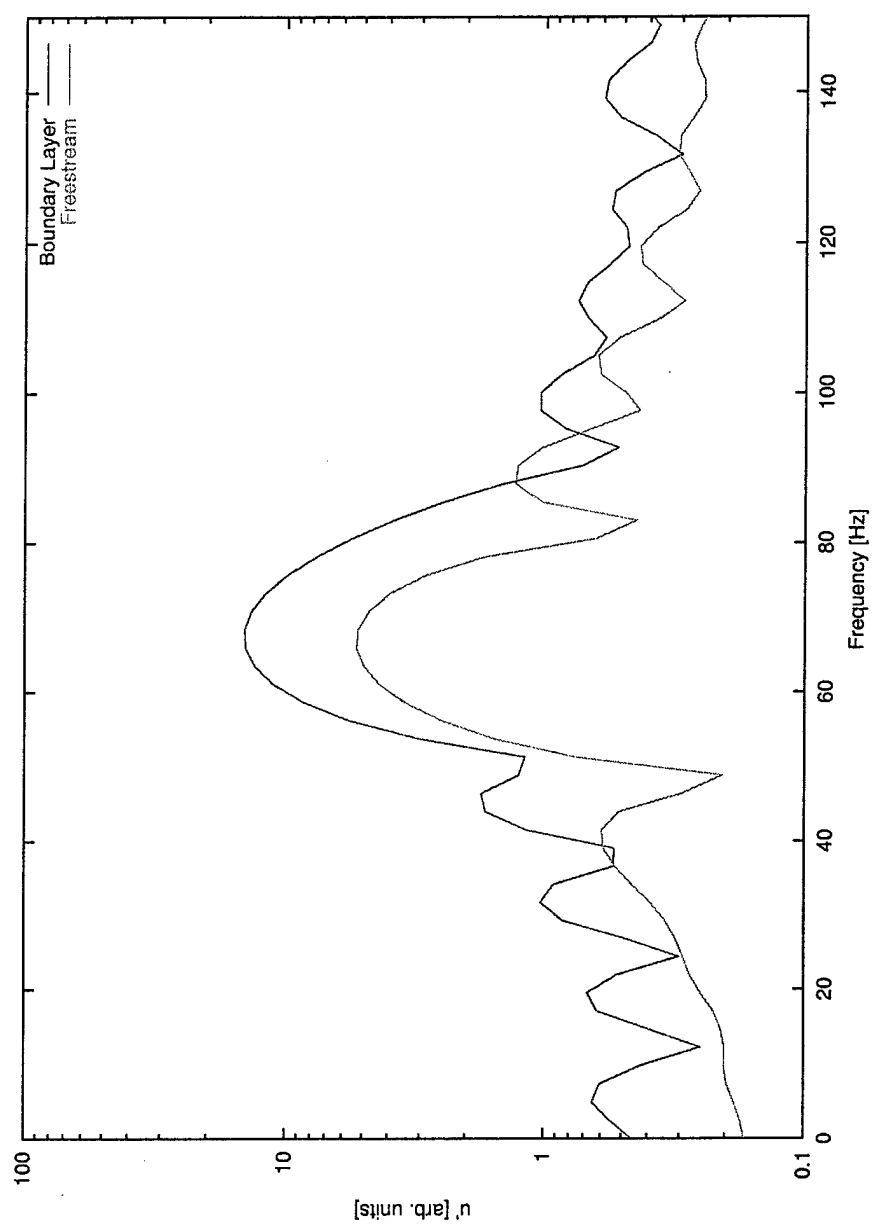Figure 56. Acoustic and T-S spectra; $U_\infty = 12$ m/s, 5-cycle, 80 Hz pulse, SPL = 107 dB.

Figure 57. Acoustic and T-S spectra; $U_\infty = 12$ m/s, 5-cycle, 67.4 Hz pulse, SPL = 111 dB.